

UC Berkeley

UC Berkeley Electronic Theses and Dissertations

Title

Emergent material properties and shape transformations of fluctuating membranes with adhered proteins

Permalink

<https://escholarship.org/uc/item/37x315dp>

Author

Ryan, Christopher J.

Publication Date

2013

Peer reviewed|Thesis/dissertation

**Emergent material properties and shape transformations of fluctuating
membranes with adhered proteins**

by

Christopher James Ryan

A dissertation submitted in partial satisfaction of the
requirements for the degree of
Doctor of Philosophy

in

Biophysics

and the Designated Emphasis

in

Computational Science and Engineering

in the

Graduate Division

of the

University of California, Berkeley

Committee in charge:

Professor Phillip Lewis Geissler, Chair
Professor Daniel Alden Fletcher
Professor David G. Drubin
Professor David Chandler

Fall 2013

**Emergent material properties and shape transformations of fluctuating
membranes with adhered proteins**

Copyright 2013
by
Christopher James Ryan

Abstract

Emergent material properties and shape transformations of fluctuating membranes with adhered proteins

by

Christopher James Ryan

Doctor of Philosophy in Biophysics

with the Designated Emphasis in

Computational Science and Engineering

University of California, Berkeley

Professor Phillip Lewis Geissler, Chair

Many processes that occur at biological membranes have been shown to be remarkable displays of molecular coordination and shape transformation. Despite the apparent complexity of these processes, investigations of simplified systems have successfully characterized many ways that these materials can self-organize. Such studies established that proteins may either bend membranes by binding to them along curved structural domains or by inserting into them asymmetrically. One recent study, however, showed that generic clusters of small membrane-adhered proteins that lack these features can nevertheless remodel membranes into highly curved shapes.

In this manuscript we use theoretical and computational methods of statistical mechanics to elucidate how a driving force for membrane curvature emerges from the steric effects among such adhered proteins. First, we develop a basic thermodynamic model of the experimental system referenced above, considering the energetic penalty of membrane bending for simple shapes while also introducing the 2-dimensional pressure of the adhered protein layer. We show that increasing the curvature of the underlying membrane effectively increases the area of the adhered protein layer, lowering the associated pressure and entropically stabilizing the composite system at nonzero curvatures. To generate quantitative predictions of curvature as a function of adhered protein concentration, we model the protein layer as a hard disk fluid and compare these results to experimental data. We also use overdamped Langevin dynamics simulations, again considering only volume excluding interactions among proteins, to observe shape transformations and fluctuations of such systems in more complex morphologies. We extend our thermodynamic model to show that cylindrical curvature becomes more stable than spherical curvature at protein densities higher than some critical value. This critical value becomes smaller as membrane area increases, which supports experimental observations and explains why tubules are unstable in simulated systems, which are much smaller.

The development of a molecular simulation model for this research was a significant effort, and we discuss this implementation in some detail. We build upon a coarse-grained model previously developed in our research group, however we modify its original functional forms to be smoothly varying and thus stable for dynamical integrators. We also develop consistent coarse-grained models for adhered proteins and for a second lipid type. We then discuss extensions developed for future studies, methods of analysis, and relaxation time scaling for cylindrical configurations.

Finally, we show how the adhered protein layer effectively renormalizes the original material properties of the underlying membrane. We begin by theoretically analyzing our composite membrane-protein system in the regime of small but nonzero curvature fluctuations. This analysis yields a form identical to the standard free energy of a bare membrane but with effective expressions for the bending rigidity, surface tension, and spontaneous curvature that are dependent on the density of adhered proteins. As protein density increases, the effective bending rigidity and spontaneous curvature reduces until the system can become unstable. We support these predictions with molecular simulation calculations of the type discussed earlier.

These results exemplify the ideas discussed at the start of this manuscript, demonstrating how the emergent characteristics of seemingly complex membranes can sometimes be remarkably folded back into the basic physics of these soft materials. Moreover, since a membrane attachment region alone is sufficient for protein clusters to produce the results presented throughout this work, these results could characterize a new and general way that proteins modify and sculpt membranes during various essential cellular processes.

Contents

Contents	i
List of Figures	iii
1 Adaptive and transformative responses of biological membranes: a review	1
1.1 Cellular processes require membranes to be stable, tunable, and transformable	1
1.2 Curvature sorting of biomolecules at membranes	2
1.3 Membrane curvature generation by biomolecules	5
1.4 Lateral domain formation by line tension renormalization and criticality	6
1.5 Nonlinear responses and dramatic transformations	7
1.6 Outlook	11
2 Steric interactions among adhered proteins drive membrane curvature	13
2.1 Background & Experiments	13
2.2 Thermodynamic modeling	14
2.3 Simulations of shape transformations by adhered proteins	18
2.4 Spherical vs. spherocylindrical curvature	19
3 Brownian dynamics simulations of fluctuating membranes at large length-scales	24
3.1 Motivation	24
3.2 The membrane patch model	25
3.3 Adapting the membrane patch potential for dynamical integrators	27
3.4 Deriving N -body force equations	29
3.4.1 Algorithmic implementation & computational efficiency	34
3.5 Incorporating different lipid types	36
3.5.1 The model	36
3.5.2 Domain boundary fluctuations and line tension measurements	38
3.6 The protein model	40
3.6.1 N -body potential	40
3.6.2 Mimicking hydrophobic insertion	43
3.6.3 Parameter choices: pathologies and practical considerations	44

3.7	Computational analysis of model properties	47
3.7.1	Bending rigidity computation	47
3.7.2	Relaxation time of cylindrical morphologies	52
3.8	Other features of the custom simulation program	54
3.8.1	Constant tension ensemble	54
3.9	Additional extensions	55
3.9.1	BAR proteins	55
3.9.2	Actin-membrane interactions	56
4	Adhered proteins renormalize the material properties of membranes	59
4.1	Introduction	59
4.2	Analytical results	60
4.3	Simulations of bending modulus and surface tension renormalization	61
4.4	Simulations of spontaneous curvature renormalization	62
4.5	Discussion	63
4.6	Appendix A: Deriving κ_{eff} , γ_{eff} , and $c_{0,\text{eff}}$	64
4.7	Appendix B: Simulation Details	67
4.8	Appendix C: Experimental measurement of κ_{eff} softening	67
5	Conclusions & Future Work	71
	References	73

List of Figures

1.1	Examples of molecular organization and curvature at biological membranes. (left) caveoli, (middle) endoplasmic reticulum, (right) mitochondrion. (All images from [1].)	2
1.2	(top) An experimental image in which a tubule is pulled from a GUV by an optical trap. The BAR family protein amphiphysin 1 (denoted amph1*) is enriched on the tubule due to its high curvature (scale bar: 5 μm). (bottom, left) Fluorescence intensity measurements that correspond to protein enrichment on the tubule may be related to theoretical expressions to calculate curvature sorting constants. (bottom, right) Tubule pulling force and surface tension can be monitored via the optical trap and micropipette suction, respectively, to measure the effect of amphiphysin 1 binding on membrane bending mechanics. (All figures from [9], plots show low density amph1* data).	4
1.3	(top) Microscopic images showing lipid domain coarsening as the temperature is lowered below the critical point (adapted from [35], each image is approximately 50 μm wide). (bottom) This schematic shows how a hybrid lipids containing 1 saturated fatty acid chain and 1 unsaturated fatty acid chain (h) can act as a line-active agents, stabilizing the domain boundary between saturated (s) and unsaturated (u) lipids (adapted from [36]).	6
1.4	(left) Upon exposure to high concentrations of cholera toxin B (CTB), GM ₁ -enriched domains phase separate from surrounding lipids on the surface of a GUV (from [44], scale bar 5 μm). (right) A schematic showing how cytoskeleton proteins (green, yellow, and blue) concentrate PIP ₂ (red) in the membrane and fosters phase separation (from [45]).	8
1.5	(left) thin actin protrusions emerge from dendritic actin networks outside of a GUV, scale bar 5 μm (middle) actin filaments protruding into the membrane are bundled to reduce membrane curvature energy (right) the membrane enclosing filament bundles provides additional structural stability since buckling requires membrane bending (adapted from [49]).	10

- 2.1 Experimental results of Stachowiak *et al.* In these experiments various proteins, such as epsin1, were tested for their ability to morphologically transform nearly-flat membrane domains. Each protein tested had a high affinity for attachment to this lipid domain and thus adhered to the GUV (giant unilamellar vesicle) in high concentration. Generally, this layer of proteins remodeled the domain into a long tubule if the domain was in the gel phase or into highly-curved shapes if the domain was fluid phase. Curved membranes are thermodynamically stabilized in this system because they provide more space in the adhered protein layer and are thus entropically favorable (schematics and first 2 images adapted from [76]; last image adapted from [75]; scale bars are $10 \mu\text{m}$ for the middle images and $2 \mu\text{m}$ for the bottom image). 15
- 2.2 How entropic forces within the protein layer can drive curvature. (left) In a simple depiction of this mechanism, consider a collection of proteins adhered to the surface of a membrane. The proteins sterically interact with each other along the dotted line through their centers, a distance l above the membrane. When the membrane is flat, this protein layer has the same area as the underlying membrane. When the membrane is curved, this area effectively increases, producing an entropic favorability that becomes more significant at higher densities of adhered proteins. (right) For a cylinder, the area of the protein layer as a function of tubule radius is $\bar{A} = 2\pi\bar{R}L = 2\pi(R+l)L = A(1 + \frac{l}{R})$ 16
- 2.3 Curvature generation mechanisms at play in Stachowiak *et al.* [75, 76]. The plot on the right separately considers the curvature predicted by the protein steric interactions (left, top) described by equation 2.3 and the curvature predicted by the hydrophobic insertion method (left, bottom) as attained from continuum mechanical strain calculations [26]. This shows that, while both likely play a role in the observed curvature generation, at high membrane coverage the effect discovered by Stachowiak *et al.* becomes most significant. The red dotted lines in the plot correspond to experimental measurements of adhered protein packing fractions for systems like those seen in Figure 2.2. These denote the packing fractions measured when 50% or 90% of vesicles, respectively, form tubules. 17
- 2.4 Physically realistic values of line tension can drive curvature in small systems. (left) This microstate from a membrane domain simulation with no proteins adhered exemplifies how appreciable curvature in the domain can become probable due to reductions in line tension free energy. (right) With high densities of proteins adhered, higher curvatures than those predicted by arguments discussed in section 2.2 can be achieved because the cinching seen here reduces the domain boundary. Above, $\eta = 0.32$ when the membrane is flat and changes with curvature throughout the trajectory. 19

- 2.5 At considerably high densities of adhered proteins (here, $\eta = 0.42$ when the membrane is flat and changes with curvature throughout the trajectory) vesicle formation can be readily observed by the mechanism discussed here. This is aided somewhat by the line tension driving force discussed in section 3.5.2. These screenshots also how display fluctuation modes of a characteristic length scale amplify due to substantial membrane tension during the vesicle formation trajectory. 20
- 2.6 Observed final morphologies depend on starting configurations during the simulation period. (left) A vesicle with adhered proteins, started in a spherical configuration. $\left(\frac{N_{\text{prot}}}{A_{\text{mem}}} = 0.93 \text{ prots}/\sigma^2\right)$. Assuming that this geometry is still approximately spherical, the radius is ~ 32.5 nm and the protein layer packing fraction is $\eta \approx 0.636$. (right) A vesicle with adhered proteins, started in a spherocylindrical configuration $\left(\frac{N_{\text{prot}}}{A_{\text{mem}}} = 0.80 \text{ prots}/\sigma^2\right)$. Though these systems feature similar numbers of proteins per membrane area, they do not reach similar configurations or curvatures during the simulation period. The spherical configuration in particular displays a curvature lower than predicted given the high density of proteins adhered. This may indicate that a sphere-to-spherocylinder transition requires a rearrangement of particles that is improbable on the timescale observed. 21
- 2.7 Simple modeling suggests that spherocylindrical vesicles become more stable than spheres as η and A_{mem} increase and as κ decreases. The top 4 plots were made by computing the total free energy for both spheres and tubules, then plotting the curvature radius of the shape with the lowest free energy. Inset images in 3 of these upper plots show simulations or experiments of system conditions corresponding to the plot parameters, however these do not necessarily exhibit accurate agreement. Upper two images are from Figure 2.6, center right image is from experiments in [75] (η unknown). In the bottom 2 plots, we use the methods above to predict morphological phase diagrams for $\kappa = 20k_{\text{B}}T$ and $200k_{\text{B}}T$ (typical fluid phase and gel phase rigidities) as a function of A_{mem} and η . 23
- 3.1 The membrane patch model of Pasqua *et al.* [66]. This meshless, solvent-free membrane model consists of a single layer of particles defined by their position and orientation. (left) Schematic showing a membrane particle 5 nm in diameter. Yellow shading corresponds to the equatorial neighbor region, blue shading corresponds to the polar neighbor region. (right) A vesicle configuration. 25
- 3.2 The G and H functions nested in the membrane patch potential. The original functions that comprise the model are piecewise and linear. Force equations derived from them are thus discontinuous and unsuitable for molecular/Brownian dynamics. The cubic equations that we replaced the original forms with are plotted here for comparison, along with a Fermi-function adaptation of the original functional forms (right plots). 28

3.3	(left) A simulation of a membrane domain of particle type 2 surrounded by membrane particles of type 1. The “mem1-mem2” interaction potential is described by equation 3.17. The domain area is $A \approx 0.032\mu\text{m}^2$ and is typical of a large-sized simulation studied here. (right) For comparison, an experimental image of a giant unilamellar vesicle used in the experiment by our collaborators [75]. The domain area here is $A \approx 100\mu\text{m}^2$	37
3.4	(top left) This schematic shows how domain boundary fluctuations are mapped to a single dimension for Fourier analysis. Adapted from [35]. (top right) A screenshot from a typical trajectory from which interfacial fluctuation data are gathered. The yellow line gives the interpolated domain boundary. (It should be noted that this calculation could be preformed slightly more straightforwardly for a linear, rather than circular, domain interface.) (bottom left) An example of interfacial fluctuation measurements that are used to calculate λ . Confer with Figure 3.12. (bottom right) The y -values of this plot give line tension in units of piconewtons. This corresponds well with experimentally measured line tensions for lipid domains, which tend to be on the order of 10^{-1} pN to 10^0 pN [34, 35].	39
3.5	The protein-membrane potential was designed for this study to diffuse fluidly on the membrane surface and features a neighbor counting scheme similar to the one embedded in the membrane-membrane potential of Pasqua <i>et al.</i> [66]. The protein-protein potential includes only volume excluding interactions. The diameter of each particle representing a membrane patch (and, thus, also the membrane thickness) is $d_{\text{mem}} \equiv \sigma$, the diameter of protein particles are $d_{\text{mem}} = 2\sigma$. The protein layer height $l = (d_{\text{mem}} + d_{\text{mem}})/2 = 1.5\sigma$ was used for the analytical curve in Figure 4.2 and was verified numerically.	40
3.6	Adapting the protein-membrane potential to mimic hydrophobic insertion.	43
3.7	These histograms show distributions of n values for the protein-membrane potential for a tubule configuration. (left) Though typical values of n are ~ 4.5 , the value for $\bar{n} = 5.5$. Thus, this tubule is driven to increase its radius to increase n for particles in the protein layer. (right) Though there is no qualitative difference in this histogram, it shows that n for protein particles is easily above \bar{n} . Thus, this does not lead to unphysical effects on system curvature.	45
3.8	Different choices of parameters for the protein-membrane potential lead to different behavior. In these simulations, a box-spanning membrane tubule of radius $R = 7.5\sigma$ is allowed to relax to lower curvatures. Clusters of similar looking trajectory data might indicate problems with parameter choices.	46

- 3.9 Unphysical crystallization occurs when lengthscale parameters of the protein-membrane potential are too small, driving protein particles to sit between membrane particles like eggs in an egg carton (as seen in the cross section image, left). Though pure systems of hard disks and hard spheres are widely known to crystallize beyond some critical packing fraction [86], the ordering in the protein layer seen above is an artifact which results using these parameters because the membrane is resolved as a discrete set of bilayer-spanning spheres. Though we anticipated that the protein layer would crystallize at high packing fractions using the “good” parameters discussed below, analogously to the pure hard disk system, this was not observed. 47
- 3.10 Parameter trace results for $\sigma_{\text{prot}} = 2\sigma_{\text{mem}}$. Good choices of parameters for the protein-membrane potential are $\{z_b = 1.5, r_b = 3.0, \bar{n} = 3\}$ or $\{z_b = 1.5, r_b = 3.5, \bar{n} = 4.5\}$ 48
- 3.11 A nearly membrane surface fluctuating above the xy -plane, characterized by the height function $h(x, y)$. This parameterization is sometimes known as the Monge gauge. (Adapted from Brown [87].) 49
- 3.12 Fourier transformed height fluctuation statistics on a log-log scale. These data can be fit to equation 3.21 to extract the bending modulus (κ) and the surface tension (γ). 50
- 3.13 (top) Snapshots of a membrane tubule simulation used to calculate κ . Here, $\langle R \rangle = 7.5\sigma$, $L_z = 25\sigma$, and $N_{\text{mem}} = 803$. (bottom left) This shows running averages of σ_{zz} computed using equation 3.23. Stress in the x and y direction converges to 0, however, z -direction stress converges to a nonzero value. Confer with Figure 3 from [88]. (bottom right) tensile force calculations, here for a bare membrane, accurately correspond to κ over a variations of tubules radius. These data at $R = 2.5 \sigma$ do not map to equation 3.22 because the tubule has ruptured. The tubule configuration cannot be sustained because the radius is approaching the natural coarse-graining length scale of the model. 51
- 3.14 Tubule relaxation trajectories. These tests were intended to measure R_0 for various protein densities by letting the tubule radii relax, however this happened very slowly for reasons described in this section. The key of this plot gives N_{prot} for each simulation, and the corresponding colored straight lines are the R_0 values each of these simulations were predicted to relax to given the equation $R_0 = \kappa/pl$ (see section 2.2). 52
- 3.15 Both the numerically integrated Langevin representation and the molecular simulation approximately scale as $R \propto (t + c_0)^{\frac{1}{4}}$, where $c_0 = (R_0)^4$, for long timescale tubule radius relaxation dynamics. Early timescale dynamics are qualitatively different, however this is expected since the molecular simulation relaxes via particle position fluctuations and the other is approximated as an exact cylinder. (left) Euler-integrated numerical solution to our Langevin representation of R_0 relaxation dynamics. (right) Molecular simulation of R_0 relaxation dynamics. 54

- 3.16 BAR family proteins and curvature generation (left) The protein structure of the the BAR domain of *Drosophila* amphiphysin [99]. The electrostatic equipotential surface in the lower image shows a high concentration of positive charge along the inner face, which is through to aid in binding and bending membranes rich in negative multivalent Phosphatidylinositol 4,5-bisphosphate (PIP₂) lipids. (right) This schematic shows how assembly features of FBAR proteins could allow these clusters to adapt to different curvatures and to possibly aid in vesicle neck constriction during endocytosis [100]. 56
- 3.17 Implementing BAR family proteins in simulation using the membrane patch model of Pasqua *et al.* [66]. (left) This schematic shows how a simple model of a BAR family protein was implemented in the simulation program. The SHAKE algorithm was used to maintain distance constraints between neighboring particles and non-neighboring particles, modeling bonds and bond angles respectively. Variations in “curviness” could model various members of the BAR protein family, and the orientational protein-membrane potential was implemented as in section 3.6.2. (right) A snapshot of coarse-grained BAR molecules above a membrane surface. 57
- 4.1 Renormalization of the bending modulus, κ_{eff} , and surface tension, γ_{eff} (data from simulations by Julian Weichsel). (top left) $\langle |h_q|^2 \rangle$ spectrum of the membrane height fluctuations around its flat state versus the corresponding mode q without adhered proteins (upper) and including adhered proteins (lower). The effective bending rigidity and surface tension are determined by fitting the small and long wavelength fluctuation regime respectively (solid line). The dashed line for comparison corresponds to a case without adhered proteins and vanishing surface tension. (top right) Renormalization of the bending rigidity and surface tension (inset) as functions of packing fraction of adhered proteins for $\kappa = 10 k_B T$ (triangles) and $20 k_B T$ (circles). Dashed and solid lines are the theoretical expectations. (bottom) Wavelength dependent instability regimes versus packing fraction of adhered proteins. 62
- 4.2 Renormalization of spontaneous curvature, $R_{0,\text{eff}}$. In the key, $\tilde{\kappa} = \kappa/k_B T$ is a reduced bending modulus, “sim” corresponds to molecular simulation data, and “CS eqn” plots equation 4.4 using the $2d$ Carnhan-Starling equation for pressure [79] and $l = (d_{\text{prot}} + d_{\text{mem}})/2 = 7.5\text{nm}$. (inset) raw data of tensile force computed as $f_z = \sigma_{zz} L_x L_y$ as a function of packing fraction of proteins. (main) Both the tensile force data and analytical curve are plotted via equation 4.6. 64

- 4.3 Coarse grained models. Here d are particle diameters and l is the height of the protein layer. (left) Triangulated mesh membrane model [89, 90], extended to include an adhered protein model. (right) The meshless membrane model we used was developed by Pasqua *et al.* [66] to study membrane height fluctuations and shape transformations at large lengthscales. This N -body potential allows fluid motion of particles within the surface, and the blue triangles represent each particle's orientation vector. The protein-membrane potential was designed for this study to diffuse fluidly on the membrane surface. The protein-protein potential includes only volume excluding interactions. The diameter of each particle representing a membrane patch (and, thus, also the membrane thickness) is $d_{\text{mem}} = 5$ nm, the diameter of protein particles are $d_{\text{prot}} = 10$ nm. The protein layer height $l = (d_{\text{mem}} + d_{\text{prot}})/2 = 7.5$ nm was used for the analytical curve in Figure 4.2 and was verified numerically. 68
- 4.4 Molecular simulation snapshots. (top) These 3 screenshots correspond to the 3 regimes in Figure 4.1 – when no mode is unstable, when large wavelength modes are unstable, and when all modes are unstable and a membrane bud forms. (bottom) The tensile force was computed in the z -direction (blue arrow) using $f_{zz} = \sigma_{zz}L_xL_y$ and then related to c_0 using equation 4.6. Here, $\langle R \rangle = 37.5$ nm, $L_z = 125$ nm, $N_{\text{mem}} = 803$, and $N_{\text{prot}} = 146$ 69
- 4.5 The results of Settles *et al.* [16] support our prediction that κ_{eff} softens as protein density increases. (left) This illustration shows the optical trap from which researchers extended membrane tethers and measured κ_{eff} from average values of tensile force. (middle) This plot shows that as protein density in solution (assumed to correlate with bound protein density) increases, κ_{eff} decreases until the system becomes unstable. (right) An image of the curvature instability seen when κ_{eff} would be predicted by the trend to become negative. 70

Acknowledgments

I'm very grateful to my adviser, Phill Geissler, as well as Lutz Maibaum, Andrea Pasqua, Anna Schneider, & Julian Weichsel for making influential contributions that shaped the research presented here. Thanks also to Jocelyn Rodgers, Ayelet Benjamini, & Yael Elmatad for many occasions of help and support. Special thanks as well to Jeanne Stachowiak, Eva Schmid, and other experimental collaborators for their thoughtful, friendly, and enthusiastic advice. And, of course, I am grateful to Lisa Littlejohn and Kate Chase for many years of friendship and guidance.

Chapter 1

Adaptive and transformative responses of biological membranes: a review

Many cellular processes demonstrate biological membranes to be stable and highly organized despite the presence of considerable environmental and intracellular noise. Membranes must nonetheless be poised for large-scale collective transformations in response to specific small changes in their environments, such as vesicle formation in response to ligand-receptor binding. Here, we review recent studies on reconstituted systems that have elucidated when and how membranes achieve such diverse responses. Experiments show that cell-like organization can require surprisingly small sets of molecular components. The often simple physical underpinnings of this remarkable adaptability are underscored by theoretical studies that recapitulate emergent responses from microscopic models with minimal molecular detail. Together, this body of work points to the possibility that even dramatic membrane rearrangements in cells can be viewed as exploiting rich intrinsic susceptibilities of this multifaceted material.

1.1 Cellular processes require membranes to be stable, tunable, and transformable

Cells engineer remarkable feats of organization in space and time in order to achieve the many processes of life. We have a particularly clear view of such phenomena at membranes due to their quasi 2-dimensional nature and microscopy technology for imaging surfaces. Such studies have revealed processes like the immune response, endocytosis, and cell motility to require membranes to be both robust to molecular noise and susceptible to large scale transformations regarding lateral organization or 3-dimensional morphology.

Through combinations of theory and experiment on such reconstituted systems, a new perspective on membrane organization is emerging: The unperturbed state of a simple lipid

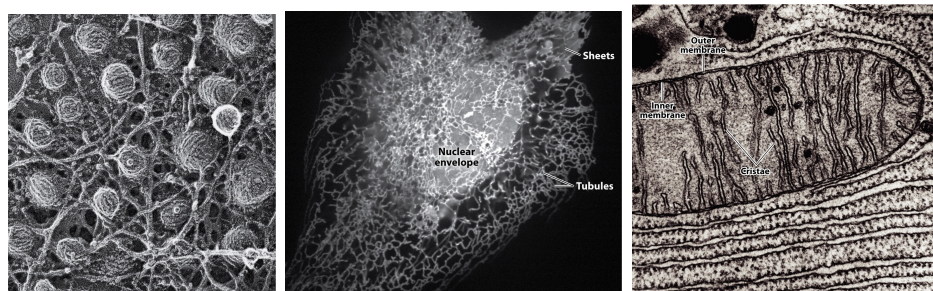


Figure 1.1: Examples of molecular organization and curvature at biological membranes. (left) caveoli, (middle) endoplasmic reticulum, (right) mitochondrion. (All images from [1].)

bilayer does not manifest the exotic features described above, either on average or in the course of typical equilibrium fluctuations. It is membranes' intrinsically strong nonlinear susceptibilities that permit access to extensive rearrangement through small changes in protein-lipid interactions.

We outline here a view of membranes as remarkable materials in which small changes may either subtly modify or dramatically transform their characteristics. Such changes typically include local modifications in the concentrations of specific biomolecules associated with various processes. Though many membrane-associated molecules have been identified and characterized, a mechanistic and physical understanding of how their interactions lead to organization is only beginning to be understood. We suggest that experiments using reconstituted membranes and minimal sets of proteins may provide the most promising way to identify the requirements for cell-like organization. Such results are often also amenable to theoretical treatment that applies and extends the principles of soft matter physics.

1.2 Curvature sorting of biomolecules at membranes

Membranes are complex mixtures whose spatial heterogeneity has functional consequences for cells. This heterogeneity is important at several scales, from the localization of specific molecules in small domains to large-scale segregation. Though many proteins have been implicated in this organization, including those that expend ATP or GTP, many membrane components have been shown to be thermodynamically driven to regions of nonzero curvature. Such regions may be imposed by the environment or the internal structure of the cell. Recently, experiments using reconstituted systems have demonstrated that the curvature sorting capacity of biomolecules can be measured and defined in terms of a membrane's linear susceptibilities.

Several molecular characteristics of proteins, lipids, and other biomolecules can cause them to be localized to curved membranes [2, 3]. BAR family proteins provide prominent examples of this. These proteins feature crescent-shaped domains and generally bind to the

membrane along their inner curve. Proteins may also have a preferred membrane curvature because they insert into the bilayer asymmetrically. This insertion leads to unequal, unfavorable lipid packing effects between leaflets when the membrane is flat. Interestingly, recent results showed that existence of membrane anchoring domains, regardless of attachment chemistry, is sufficient for targeting proteins to regions of curvature [4, 5]. Furthermore, the kinetics of membrane attachment was shown to rely primarily on membrane rather than protein characteristics. This reliance is because non-flat membrane configurations increase molecular fluctuations that open binding sites for protein attachment.

Optical microscopy can be used to examine concentration differences in heterogeneously curved membranes. Such experiments typically feature some apparatus, such as an optical trap, for mechanically pulling a narrow tubular tether from the surface of a giant unilamellar vesicle (GUV) [6, 3] (see Figure 1.2, top). Curvature sensitive molecules with fluorescent probes will sort between regions on the negligibly-curved GUV surface and the highly-curved tether. Since photon intensity measurements directly correspond to fluorophore concentration, the enrichment of labeled biomolecules on the tether can be measured.

Tian & Baumgart [7] used such experiments to test the curvature sorting capacities of both lipids and proteins. Interestingly, theoretical analysis of these data showed that entropic effects may be appreciable enough to prevent lipid sorting even when lipids feature a preferred curvature. The authors note that previous experiments imply that cooperativity among lipids can produce sorting in such cases [8]. The protein cholera toxin B, in contrast, was shown to sense curvature significantly due to its shape and to also to affect the rigidity properties of the membrane.

Sorting analyses by Tian & Baumgart and several others are based upon the standard description of membrane bending mechanics [10, 11]. At lengthscales on the order of ~ 10 nm or greater, the membrane may be modeled as a continuum elastic sheet of negligible thickness. Geometric arguments derived by Canham and Helfrich lead to the following curvature (free) energy for a membrane of fixed topology [12, 13]:

$$F_{\text{bend}} = \int d\mathbf{A} \frac{\kappa}{2} [2H - c_0]^2 \quad (1.1)$$

The bending modulus, κ , describes the stiffness of the membrane and is composition dependent. H is the mean curvature at a point on the membrane (geometrically defined as $\frac{1}{2}[C_1 + C_2]$, where $C_i = 1/R_i$ are the 2 principal curvatures). The spontaneous curvature of the membrane, c_0 , defines the curvature at which this expression is minimized. It can be non-zero when the two layers are compositionally asymmetric (i.e., they contain different numbers of molecules or contain different mole fractions of molecules with nonzero curvature preferences).

The relationship between curvature and other material properties, such as composition, can often be understood in the context of equation 1.1. For example, the dependence of the bending modulus, κ , on lipid tail saturation [14], cholesterol concentration [15], and adhered protein density [16] has been characterized in experiment. Theoretical treatment of

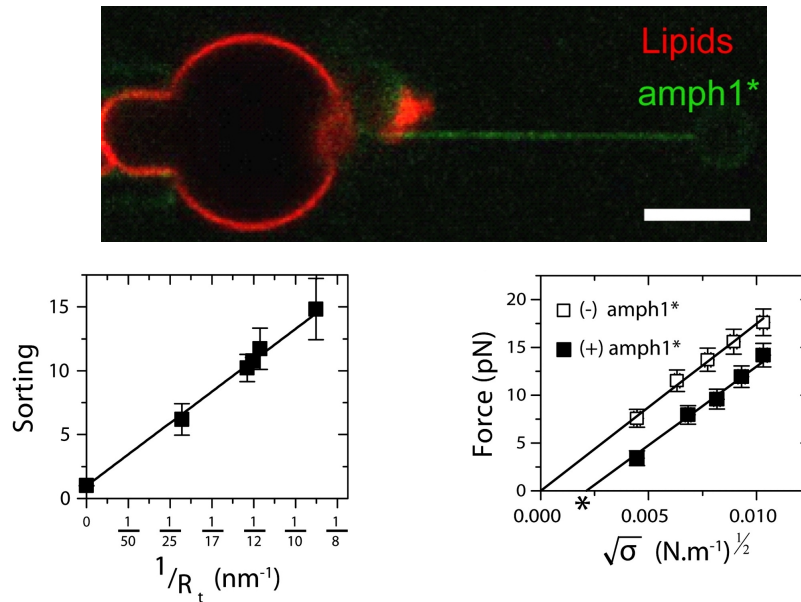


Figure 1.2: (top) An experimental image in which a tubule is pulled from a GUV by an optical trap. The BAR family protein amphiphysin 1 (denoted amph1*) is enriched on the tubule due to its high curvature (scale bar: 5 μm). (bottom, left) Fluorescence intensity measurements that correspond to protein enrichment on the tubule may be related to theoretical expressions to calculate curvature sorting constants. (bottom, right) Tubule pulling force and surface tension can be monitored via the optical trap and micropipette suction, respectively, to measure the effect of amphiphysin 1 binding on membrane bending mechanics. (All figures from [9], plots show low density amph1* data).

additional material properties, such as molecular inclusions [17], has sometimes been shown to reduce to a form equivalent to equation 1.1 with analytical expressions for an effective κ [18, 19].

Coupling between curvature and composition can also be incorporated analytically by expressing c_0 as a linear combination of the spontaneous curvatures of a membrane's constituent molecules. For a membrane composed of lipids A and B, this corresponds to defining $c_0 = c_A\phi_A + c_B\phi_B$, where ϕ_i is a mole fraction and c_i is the spontaneous curvature of molecule i . The mixing free energy can be described by modeling the membrane as a lattice gas [10] and molecular interactions can also be added. With a complete description of the free energy of the system, chemical potentials ($\mu = (1/N)\frac{dF}{d\phi}$) can be derived and used to fit sorting data between two adjoining regions at equilibrium [20]. Similar treatments were also used to explain pearling [21] and coiling [22] morphological transformations of a particular reconstituted membrane system featuring a high concentration of adsorbed polymers.

1.3 Membrane curvature generation by biomolecules

Many molecules that are targeted to curved membranes can also generate curvature when bound in high density. Several ways that proteins generate membrane curvature have been well-established [23]. Some employ “active” mechanisms that consume chemical energy in the form of adenosine triphosphate (ATP) or guanosine triphosphate (GTP). Dynamin, which coils around the necks of budding vesicles and hydrolyzes GTP to pinch them off the parent membrane, is one well-studied example. Other proteins aid in curvature generation without expending chemical energy [3]. Some achieve this by binding the membrane along an intrinsically curved structural region. The crescent-shaped protein amphiphysin and several other BAR family proteins have been attributed to bending in this manner [24]. Protein structures may also induce nonzero curvature via asymmetric insertion of the protein within the lipid bilayer. This insertion leads to more crowding in one leaflet than the other, which can be relieved by adopting some nonzero curvature. For membrane spanning proteins this effect can be achieved by, e.g., having a cone-shaped native conformation. Similarly, membrane-associated proteins like epsin1 [25] that adsorb from the cytosol have been attributed with curvature generation by inserting part of their structure into the hydrophobic region of the adjacent membrane leaflet. However, curvature generation by this “hydrophobic insertion” effect alone requires typical hydrophobic insertions to cover 10-25% of the membrane [26]. For some proteins previously shown to bend membranes, appreciable bending would require nearly complete coverage of the underlying surface.

Similar to curvature sorting studies described above, reconstitution experiments using mechanically manipulated GUVs interpreted using linear response theories can be used to measure the curvature induction capacity of proteins. Recent work by Sorre *et al.* used this approach to identify the crossover between curvature-sensing and curvature-inducing concentrations of amphiphysin [9] (see Figure 1.2). Their results showed that, at low densities, the BAR family protein amphiphysin was both highly enriched on membrane tubules and also mechanically stabilized curvature. These data showed that the tether pulling force was proportional to the square root of the membrane’s surface tension. This relationship corresponded to a free energy model similar to the one we described above in which c_0 in equation 1.1 is modeled as a function of the mole fraction of curvature-inducing molecules. At higher densities of adsorbed amphiphysin, however, the tether pulling force was linearly proportional to the membrane’s surface tension. These data were well supported by a revised model that additionally considered protein-protein and protein-membrane interactions and predicted stronger mechanical effects. Experimental observations also showed that amphiphysin molecules oligomerized into tubule-spanning scaffolds in this regime.

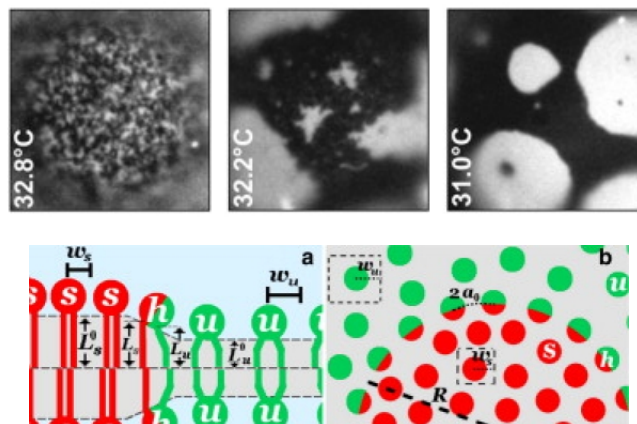


Figure 1.3: (top) Microscopic images showing lipid domain coarsening as the temperature is lowered below the critical point (adapted from [35], each image is approximately $50 \mu\text{m}$ wide). (bottom) This schematic shows how a hybrid lipids containing 1 saturated fatty acid chain and 1 unsaturated fatty acid chain (h) can act as a line-active agents, stabilizing the domain boundary between saturated (s) and unsaturated (u) lipids (adapted from [36]).

1.4 Lateral domain formation by line tension renormalization and criticality

Molecular organization in biological membranes also occurs in regions that are not appreciably curved. For example, antigen binding by T cell receptors leads to the aggregation of characteristic lipids and signaling proteins that ultimately initiate lymphocyte activity [27, 28]. To explain how cells achieve such clustering, the concept of lipid rafts was introduced [29, 30]. This hypothesis suggests that basic mixing thermodynamics is sufficient to cause biomolecules associated with particular signaling pathways to be compartmentalized into domains. Because lifetimes and size distributions of membrane domains are difficult to conclusively measure *in vivo* [31, 32], this idea remains somewhat controversial. Nevertheless, numerous observations of signaling complexes containing biomolecules that favor demixing, as well as successful *in vitro* reconstitution of lipid rafts [33], support this hypothesis as a common structural motif.

The formation of membrane domains from an initially de-mixed state is generally associated with an interfacial free energy penalty. This driving force has been suggested to originate from van der Waals attractions between tails, which are typically maximized when lipids of the same species are clustered into domains and thus produce an enthalpic driving force for molecular aggregation (i.e., “phase separation”) [34]. This penalty is parameterized by the line tension λ , which is defined as the free energy cost per length unit of interface. When this penalty is significant, strong phase separation of components is favored over collections of domains despite the entropic driving forces toward mixing.

One way domain boundaries may be stabilized is by specialized proteins or lipids that

selectively adsorb to this interface. Their effects can often be understood to reduce, or “renormalize,” the line tension [37, 38]. This renormalization stabilizes distributions of small clusters analogously to how surfactants stabilize oil and water mixtures in microemulsions. The intramolecular characteristics of these line-active agents, or “linactants,” thus favor both membrane environments separated by the boundary. Proposed boundary-active agents include lipids with with one fully saturated hydrocarbon chain and one partially unsaturated chain [39] (see Figure 1.3), such as POPC, or proteins with similar boundary-favoring characteristics [40].

Prominent research using reconstituted systems recently characterized how critical phenomena can reduce this interfacial penalty. Results from this theory show that line tension for such systems is a function of temperature according to $\lambda(T) = \lambda_0 |(T - T_c)/T_c|^\mu$. Here, T is temperature, T_c is the critical temperature below which domains form, $\lambda_0 = \lambda(T = 0)$, and μ is a critical exponent. This relationship shows that as $T \rightarrow T_c$, line tension vanishes and domains may form at a negligible free energy cost. Remarkably, experimental measurement of these critical exponents showed a striking quantitative correspondence between bi-component membranes and the 2-dimensional Ising model [41, 35]. This theoretical model was originally developed to describe the statistical mechanics of ferromagnets and has since become a cornerstone in the general study of phase transitions.

Such results also are notable because values of T_c that have been identified are typically near physiological temperatures. This property has been observed in membranes with few components as well as extracts from various cells [30], suggesting that biological systems might indeed exploit this inherent physics to organize molecules. At fixed temperature, proximity to a critical point suggests that domain size distributions could also be sensitive to changes in the mole fractions of molecular components. Mole fractions could therefore be tuned by cellular processes to organize and disorganize signaling molecules. Physical considerations similar to these may also prove useful for explaining molecular co-localization and aggregation away from the membrane. Notable examples of such aggregation phenomena include organelles comprised of liquid-like clusters of proteins and other biomolecules, like the nucleolus and Cajal bodies, that dynamically organize and disperse without requiring a membrane enclosure [42]. Criticality as a possible general motif of biological organization and long-range correlation has been proposed, but is currently a matter of debate [43].

1.5 Nonlinear responses and dramatic transformations

Though the above examples show membranes to be stable and adaptable to small changes, similarly modest changes may also elicit dramatic large-scale transformations between distinct material states. These nonlinear responses may endow membranes with a switch-like behavior that helps to form mesoscale structures and organelles. To identify minimal requirements for such transformations, reconstituted systems of lipid bilayers and associated

proteins have been particularly helpful.

Phase separation is one example of a large scale change in the material character of membranes. As discussed above, this can be induced in laboratories by changing the temperature of a system below its miscibility critical temperature T_c . In cells, however, this must be induced at fixed temperature for phase separation to be an organizing principle. Results by Hammond *et al.* used simplified model systems to show that the cross linking of membrane components can induce such a fixed-temperature phase separation [44]. The model membrane used contained sphingomyelin, cholesterol, phosphatidylcholine, and the ganglioside GM₁. Upon addition of cholera toxin B (CTB), which cross-links GM₁ molecules, phase separation between ordered and disordered domains occurred. Addition of this component corresponded to a shifting of the T_c from 42 to 47°C. Later experiments showed that CTB-induced cross linking of GM₁ in lipid extracts from plasma membranes can induce raft-like domain formation at physiological temperatures [46]. In a similar manner, a minimal system containing components of the actin cytoskeleton has also been shown to induce phase separation at fixed temperatures [45]. These domains were enriched in phosphatidylinositol 4,5 biphosphate (PIP₂), a lipid involved in numerous signaling pathways, suggesting that actin could be an important inducer of signaling-related organization in cells.

Large scale transformations of membranes also occur morphologically. Though we have discussed above several established ways proteins may induce curvature, a new and general mechanism for membrane remodeling by steric interactions among proteins is emerging. Research by Stachowiak *et al.* used GUVs with high densities of adhered proteins to show that, because curved membranes effectively increase the area of the adhered protein layer, non-flat configurations are entropically stabilized (see Figure 2.1; further discussed in Chapter 2). Each protein studied had different capacities for membrane bending, however none had intrinsically curved structures nor hydrophobic insertion regions large enough to generate the high curvature observed. Three of the proteins studied were involved in membrane

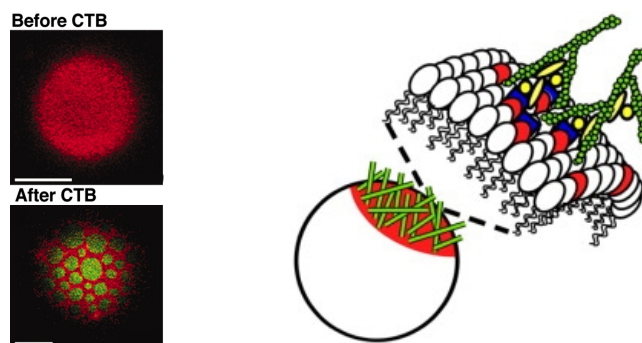


Figure 1.4: (left) Upon exposure to high concentrations of cholera toxin B (CTB), GM₁-enriched domains phase separate from surrounding lipids on the surface of a GUV (from [44], scale bar 5 μm). (right) A schematic showing how cytoskeleton proteins (green, yellow, and blue) concentrate PIP₂ (red) in the membrane and fosters phase separation (from [45]).

remodeling processes like endocytosis or vesicle trafficking, suggesting that this mechanism could be of general importance in cells. Ways that cytoskeletal interactions or clathrin scaffolds might modulate this effect remain unexplored, however these structures could serve to concentrate membrane bending proteins at specified in regions and enhance bending by this effect. (Post-translational modifications of membrane-adhered proteins could serve to dynamically enhance or diminish this effect in biological processes.) (Later work showed that this pressure can destabilize lipid domains [47].) These results thus parallel work discussed in Section 1.2 regarding the minimal requirements for curvature sorting, together suggesting that membrane attachment regions alone are generically sufficient for both membrane curvature generation and targeting. Further physical analysis inspired by ideas from these results constitutes much of the rest of this thesis.

Research in cell motility provides many of the most remarkable examples of dynamical organization between membranes and the cytoskeleton. One of the most well studied and universal proteins that comprise this cytoskeleton is actin [48]. Actin monomers (G-actin) freely diffuse and are typically bound to ATP. Hydrolysis of ATP releases energy and causes conformational changes that allow monomers to polymerize into actin filaments. Actin filaments (F-actin), along with associated proteins and lipids, assemble into various dynamical composite structures that allow cells to generate forces, transport material within the cytoplasm, and transform into functional shapes. Examples of such structures include filopodia, which are membrane-wrapped bundles of actin filaments used for cell motility. Actin and many associated biomolecules have been biochemically characterized, however relatively few composite actin-based structures are understood mechanically and kinetically.

Results by Liu *et al.* [49] showed that filopodia-like structures can emerge as a result of the combined material properties of membranes and actin. The investigated system contained giant unilamellar vesicles (GUVs) immersed in a solution containing G-actin monomers and proteins required for actin polymerization. Measurements showed these structures to contain ~ 10 filaments per filopodium and to be stable against restoring forces on the order of piconewtons.

Theoretical examination showed how membrane and actin mechanics together cause these structures emerge. The bending mechanics of actin filaments is well described by the standard “wormlike chain” model of semiflexible polymers. The form of this energy is

$$E_{\text{fil}} = k_{\text{B}}T \frac{l_{\text{p}}}{2} \int_0^L \left| \frac{d^2 \mathbf{r}(s)}{ds^2} \right|^2 ds \quad (1.2)$$

where L is the contour length of the polymer and s is the arc length along the filament $\mathbf{r}(s)$. The persistence length, l_{p} , parameterizes the rigidity of the polymer and is approximately $15 \mu\text{m}$ for F-actin. First, the authors used numerical calculations of equations 1.1 and 1.2 above to show that the organization of actin filaments into bundles can stabilize this total composite system. This is because bundled configurations appreciably lower the membrane curvature energy, offsetting the energetic cost of filament bending (figure 1.5). Similarly, the

membrane stabilizes filopodia against higher restoring forces than previously estimated [50] because buckling requires the additional energetic cost of bending the membrane.

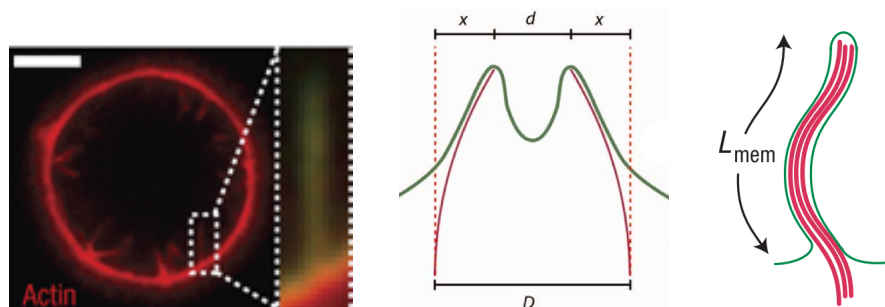


Figure 1.5: (left) thin actin protrusions emerge from dendritic actin networks outside of a GUV, scale bar $5 \mu\text{m}$ (middle) actin filaments protruding into the membrane are bundled to reduce membrane curvature energy (right) the membrane enclosing filament bundles provides additional structural stability since buckling requires membrane bending (adapted from [49]).

Other recent studies have provided additional examples of the ability of actin to self-organize with associated biomolecules. Lee *et al.* used a larger set of components to reconstitute filopodium-like structures and dynamically monitor their assembly via TIRF microscopy [51]. These results suggested that early stages of filopodium formation might begin via clustering of activator proteins related to Arp2/3-based actin branching. Other remarkable self-assembly properties observed in actin-based systems show no apparent analogue in cells. For example, reconstitution using components of the actomyosin system, which is related to muscle contraction, produced coherent flocking motions among filaments in clusters 20 to $500 \mu\text{m}$ in diameter [52, 53]. Similar experiments using microtubules produced lattices of vortex-like structures approximately $400 \mu\text{m}$ in diameter [54]. Closer examination of results such as these might reveal biologically important assembly features as well as inspire the design of novel nanomaterials.

Clathrin-mediated endocytosis is another eminent example of coordinated molecular organization and curvature control at biological membranes [55]. This process provides a means for uptake of molecules like low-density lipoprotein (i.e., “good cholesterol”), iron, various hormones, and other signaling molecules. Receptor molecules sit within an inward-curved pit on the cell membrane $\sim 100\text{-}200 \text{ nm}$ in diameter that is stabilized by various proteins within the cell. Among these coat proteins is clathrin, a protein with 3 “heavy” chains and 3 “light” chains that oligomerizes to form a lattice pattern along pit reminiscent of a soccer ball. Upon binding of the receptor’s corresponding ligand, a sequence of steps occurs that transforms this pit into a vesicle coated with proteins which dissociate upon full vesicle formation. The vesicle is then transferred elsewhere in the cell for further activity. The entire process takes about 1 minute.

Despite myriad proteins taking part in this process [56], pioneering experiments showed that stable clathrin-coated pits with a well defined size distribution require only the proteins

epsin & clathrin along with a lipid monolayer of brain lipids containing 10% phosphatidylinositol-4,5-bisphosphate (PIP₂) [25]. This report also showed that epsin alone is sufficient for transforming low curvature vesicles composed of mammalian brain lipids into tubules ~20 nm in diameter. More recent work showed that complete budding, scission, and vesicle formation can occur with the additional inclusion of dynamin and chemical energy in the form of GTP [57]. Though this identifies minimal requirements for an endocytosis-like process, other proteins shown to regulate endocytosis in cells are still likely to play important roles. Recent characterization of the timecourse of clathrin-mediated endocytosis in live cells could help guide further reconstitution experiments to elucidate the contributions of the actin cytoskeleton and BAR proteins [58].

1.6 Outlook

The examples above illustrate a particularly fruitful “bottom up” approach for understanding diverse ways membranes adapt and transform in response to small changes. Along the way, advances have been made in both experimental techniques and theoretical descriptions based upon soft matter physics. Though we anticipate this approach will continue to reveal minimal requirements for increasingly cell-like organizational features, several advances will likely need to occur before such complexity can be reached.

Developing new reconstitution technologies to study phenomena at membranes will continue to be a fruitful but challenging task. One new technique that is particularly promising creates highly customized giant unilamellar vesicles using microfluidic jetting [59]. This apparatus provides a way of independently controlling lipid composition in each leaflet as well the vesicle’s internal contents. Such techniques could be used for studying such compositional effects as well as the effect of vesicle confinement, however, several control variables in this method remain limited. Reconstituted systems can also be a powerful way for emulating interactions between cells and their environment, as shown by recent work regarding the effect of glycan network patterns on lipid domain formation [60].

Molecular simulation has proved to be an indispensable research tool for studying membranes as well as myriad subfields of soft matter [61]. These techniques are typically used when analytical descriptions are unattainable or too complex to be insightful. However, accurate simulations of biological systems can come at considerable computational expense. To this end, many “coarse-grained” models have been developed across that abstract chemical detail to a substantial degree while retaining correct large scale thermodynamic properties [62, 63, 64, 65, 66]. These models have enabled studies of large scale membrane remodeling by curved proteins [67], vesicle formation and fusion [68], the effect of cholesterol on phase behavior [69], and much more. Though each model is tuned to accurately reproduce various thermodynamic properties, dynamical properties may not be accurately modeled. Accurate coarse-grained methods for dynamical simulation of membranes are available for relatively few cases [70] and atomistic simulations are often necessary [71]. Future advances that make simulations more accurate and larger in scale will make them an increasingly valuable tool.

Surface tension is another material property of membranes that is emerging as an important modulator of organization. Though there have been many demonstrations of this importance in live cells [72], relatively few studies have used minimal reconstituted systems and so we have not highlighted this here. In one recent *in vitro* study, however, Staykova *et al.* used a controllable elastic surface that allowed an adhered membrane to be stretched and compressed [73]. The researchers observed that the membrane could passively fuse or generate adjacent vesicles in order to add or remove material from the membrane, without the aid of proteins. This tension response is analogous to that seen in caveoli in cells [74].

Chapter 2

Steric interactions among adhered proteins drive membrane curvature

Here, we discuss the experimental results that inspired much of this work as well as our analysis of these results using physical modeling and simulations. Throughout this chapter and elsewhere in this manuscript, discussions of “adhered proteins” refer to proteins that are bound to the surface of the membrane and interact with each other only through volume excluding interactions. Unlike previously established curvature generating proteins discussed in section 1.3, they do not contain any appreciable insertion into the bilayer or any intrinsic structural curvature (unless otherwise noted). Our analysis therefore isolates the newly discovered curvature driving force that emerges from steric interactions in the adhered protein layer.

2.1 Background & Experiments

The majority of the research presented in this thesis was inspired by the experimental discoveries of Stachowiak and coworkers regarding a new driving force for membrane curvature generation by proteins [75, 76] (see Figure 2.1). In both of these studies, researchers prepared giant unilamellar vesicles (GUVs) that phase separate into 2 distinct regions at the experimental temperature. One region was much smaller, consisting of $\sim 10\%$ of the surface area. These GUVs were then exposed to high concentrations of small proteins that were selected to bind tightly to the smaller domain. The proteins studied included epsin1, an endocytosis-related protein previously associated with membrane bending [25], his-GFP, a histidine-tagged green fluorescent protein engineered to bind to the membranes being studied, and others. For gel phase lipid domains (bending modulus $\kappa \sim 200 k_B T$), the domain was remodeled into a long, stable tubule. For liquid-disordered lipid domains ($\kappa \sim 20 k_B T$), more similar to those found in cells, highly curved and fluctuating fingerlike structures were formed.

These results were surprising because they defied explanation by any previously proposed

membrane bending mechanism. The means by which collections of proteins bend membranes has been thoroughly studied [3, 23], and proteins like those studied by Stachowiak *et al.* were thought to bend membranes solely by a hydrophobic insertion mechanism (see section 1.3). However, considerations of this effect alone would require such proteins to almost ubiquitously cover the membrane. The authors demonstrated that this is highly unlikely by developing a novel FRET assay to estimate the packing fraction (i.e., % area coverage) of proteins on the membrane. This showed that, even in experiments where almost all vesicle domains formed highly curved tubules, proteins typically covered up to only 50% of the surface (see Figure 2.3). The authors proposed that the driving force for curvature generation originated from crowding effects among the adhered proteins. Since the second paper studied proteins and membrane compositions highly relevant to biological systems, these results suggest that this steric effect could be an important driving force of curvature for cellular processes.

2.2 Thermodynamic modeling

To explain how curvature was stabilized in this system we proposed that curved membranes effectively increase the area of the protein layer, making such configurations entropically favorable for the composite system. This can be supported with simple theoretical arguments. For example, consider equation 1.1, the Helfrich free energy model, with respect to a single-component membrane tubule of radius R (i.e., $C_1 = 1/R$, $C_2 = 0$, $c_0 = 0 \text{ nm}^{-1}$) in combination with an adhered protein layer,

$$\begin{aligned} F &= F_{\text{mem}} + F_{\text{prot}} \\ &= \frac{\kappa}{2} \left[\frac{1}{R_1} + \frac{1}{R_2} - c_0 \right]^2 A + \gamma A + F_{\text{prot}} \end{aligned} \quad (2.1)$$

$$= \kappa \frac{1}{2R^2} A + \gamma A + F_{\text{prot}} \quad (2.2)$$

where γ is the surface tension and A is the membrane area. The area of the adhered protein layer can be written as $\bar{A} = A \left(1 + \frac{l}{R}\right)$, where l is the plane above the membrane upon which the proteins sterically interact (see figure 2.2). Minimizing the free energy of this composite system with respect to R gives an expression for the tubule radius at equilibrium, R_0 ,

$$\begin{aligned} 0 &= \frac{\partial F}{\partial R} = \left(\frac{\partial}{\partial R} \left(\kappa \frac{1}{2R^2} A \right) \right)_A + \left(\frac{\partial}{\partial R} (\gamma A) \right)_A + \left(\frac{\partial F_{\text{prot}}}{\partial \bar{A}} \right)_A \left(\frac{\partial \bar{A}}{\partial R} \right)_A \\ &= -\frac{2\kappa}{2R_0^3} A + (-p) \left(-\frac{Al}{R_0^2} \right) \\ R_0 &= \frac{\kappa}{pl} \end{aligned} \quad (2.3)$$

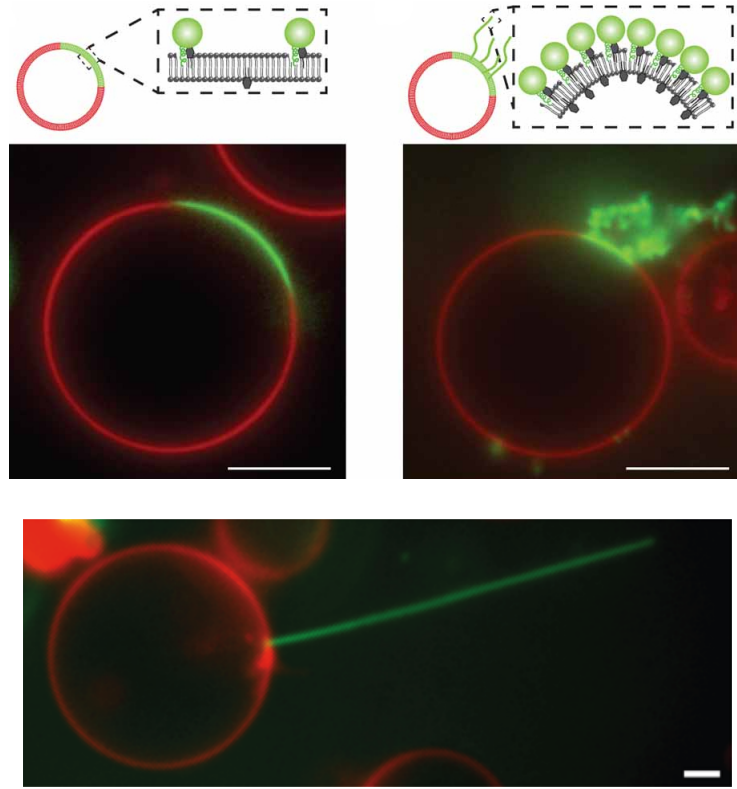


Figure 2.1: Experimental results of Stachowiak *et al.* In these experiments various proteins, such as epsin1, were tested for their ability to morphologically transform nearly-flat membrane domains. Each protein tested had a high affinity for attachment to this lipid domain and thus adhered to the GUV (giant unilamellar vesicle) in high concentration. Generally, this layer of proteins remodeled the domain into a long tubule if the domain was in the gel phase or into highly-curved shapes if the domain was fluid phase. Curved membranes are thermodynamically stabilized in this system because they provide more space in the adhered protein layer and are thus entropically favorable (schematics and first 2 images adapted from [76]; last image adapted from [75]; scale bars are $10 \mu\text{m}$ for the middle images and $2 \mu\text{m}$ for the bottom image).

where $p = -\left(\frac{\partial F_{\text{prot}}}{\partial A}\right)$ is the 2-dimensional pressure across the adhered protein layer. Stability relationships show that this pressure monotonically increases with the packing fraction of adhered proteins [77]. (Note: throughout the thesis we consider the packing fraction of proteins, η , instead of the density. The resulting statements are thus slightly more general since they do not consider protein size or number density in order to effectively consider only one parameter.)

We began to study the implications of equation 2.3 by considering only volume-excluding steric interactions among proteins on the membrane surface. This simplification corresponds

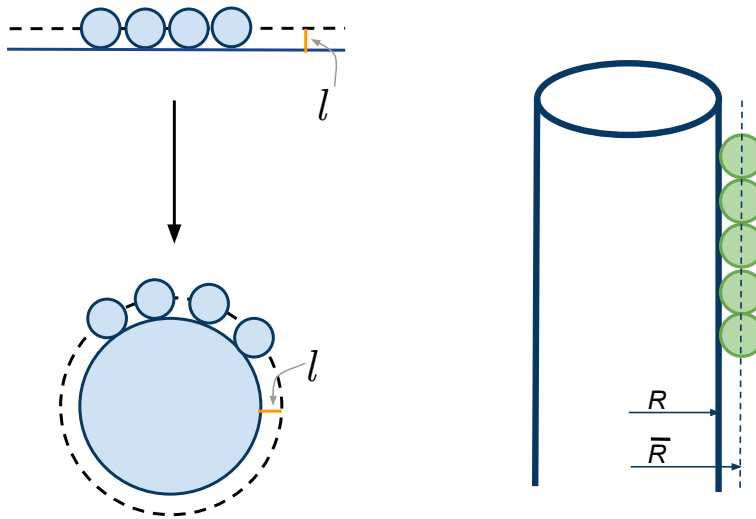


Figure 2.2: How entropic forces within the protein layer can drive curvature. (left) In a simple depiction of this mechanism, consider a collection of proteins adhered to the surface of a membrane. The proteins sterically interact with each other along the dotted line through their centers, a distance l above the membrane. When the membrane is flat, this protein layer has the same area as the underlying membrane. When the membrane is curved, this area effectively increases, producing an entropic favorability that becomes more significant at higher densities of adhered proteins. (right) For a cylinder, the area of the protein layer as a function of tubule radius is $\bar{A} = 2\pi\bar{R}L = 2\pi(R + l)L = A(1 + \frac{l}{R})$.

well with the characteristics of the proteins studied by Stachowiak *et al.*, which are expected to have no other significant interactions (GFP does dimerize, but only in an antiparallel configuration). For spherical proteins adhered to a surface, this assumption physically corresponds to the hard disk model of fluids from classical statistical mechanics [78]. An equation of state for the pressure of this model, the Carnahan-Starling equation, is highly accurate for this model's liquid state. Though the hard disk model does freeze at $\eta = 0.723$, we have no evidence that our system of proteins adhered to fluctuating membranes freezes in either simulation or experiment.

Song, Mason, & Stratt give a form for the d -dimensional Carnahan-Starling equation of state [79], which for $d = 2$ is

$$\frac{\beta p}{\rho} = 1 + b\rho g(\sigma^+) \tag{2.4}$$

where

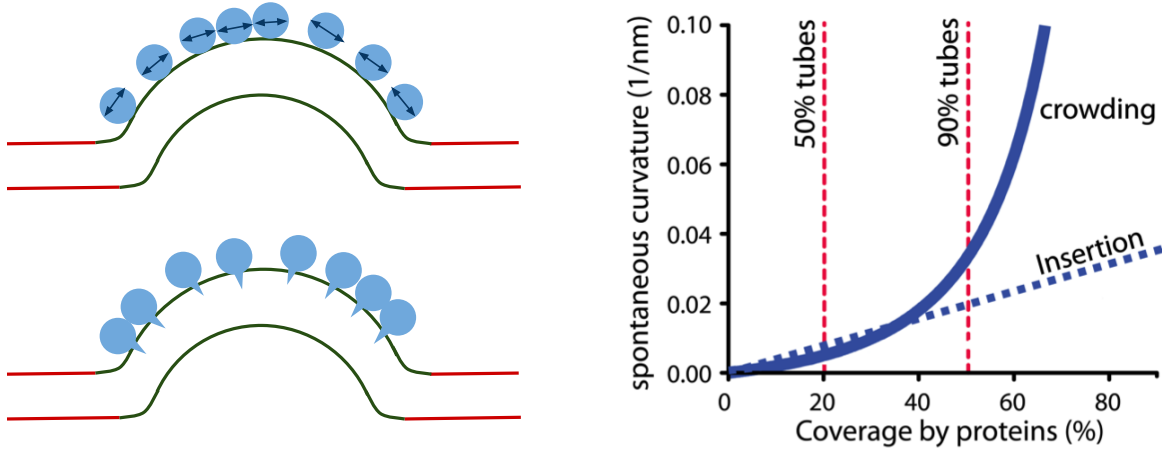


Figure 2.3: Curvature generation mechanisms at play in Stachowiak *et al.* [75, 76]. The plot on the right separately considers the curvature predicted by the protein steric interactions (left, top) described by equation 2.3 and the curvature predicted by the hydrophobic insertion method (left, bottom) as attained from continuum mechanical strain calculations [26]. This shows that, while both likely play a role in the observed curvature generation, at high membrane coverage the effect discovered by Stachowiak *et al.* becomes most significant. The red dotted lines in the plot correspond to experimental measurements of adhered protein packing fractions for systems like those seen in Figure 2.2. These denote the packing fractions measured when 50% or 90% of vesicles, respectively, form tubules.

$$b = \frac{\sigma^2 \pi}{2}$$

$$g(\sigma^+) = \frac{1 - \alpha \eta}{(1 - \eta)^2}$$

$$\alpha = 2 - 2 \left(\frac{4}{3} - \frac{\sqrt{3}}{\pi} \right)$$

$\rho = N/\bar{A}$ is the number density, $\beta = 1/k_B T$, and σ is the disk (or, protein) diameter. Throughout this thesis, any reference to results using the Carnhan-Starling equation refer to computations of equation 2.4 as a function of packing fraction.

Though cells feature systems that are considerably more complex, the bending mechanism presented here could be of general importance in biological processes. The results of the

2012 Stachowiak *et al.* report consider several unmodified cellular proteins adhered to lipid bilayers rich in PIP₂ (Phosphatidylinositol 4,5-bisphosphate), a lipid concentrated in membrane regions of high activity. Furthermore, these results suggest that proteins with neither curved structures nor large hydrophobic insertions can still appreciably bend membranes, widening the scope of curvature inducers in cells. Though some biologists have misunderstood this effect to become extinguished under molecular scaffolds like clathrin [80], this interpretation should not be valid as long as there are molecular fluctuations that favor area expansion. In fact, scaffolds could instead be a way of concentrating proteins such that this effect is enhanced.

2.3 Simulations of shape transformations by adhered proteins

Though the theoretical statements above elegantly support the experimental results, many aspects of these systems cannot be examined analytically. These include shape transformation pathways and the possible coupling of morphology and phase behavior within the protein layer. To explore such research questions we applied and extended a coarse-grained membrane model developed within our research group [66]. These developments are discussed in detail in Chapter 3.

Early tests of this model were conducted by starting simulations with some packing fraction η of proteins adhered to a flat domain of “membrane 2” particles, which are depicted as red spheres in figures throughout this manuscript. (Membrane 2 particles feature a repulsive potential between membrane 1 particles, which are depicted as white spheres, and also specifically adhere to the coarse-grained protein model.) Simulations were integrated in time using overdamped Langevin (i.e., Brownian) dynamics in a zero-tension ensemble (see section 3.8.1). In all cases tested, the domain readily adopts curvature proportional to the density of proteins adhered. Curvature can be partially driven by line tension due to small system sizes (see Figure 2.4 and Section 3.5.2). Budding and vesicle formation processes are observable beyond some density for systems of considerable size (see Figure 2.5). Though simulations like these could provide insight into vesicle sculpting processes, our model does not resolve individual lipids and thus cannot characterize the molecular rearrangements that are likely to be important for vesicle detachment transitions in experimental systems.

We also performed exploratory tests in which a fixed amount of proteins was adhered at various densities evenly to the surface of a small vesicle (see Figure 2.6). Simulations were then run to observe the equilibrium morphologies into which these systems relaxed. Interestingly, spherical vesicles with very high densities of proteins were not observed to transform to higher curvatures, as predicted using theoretical arguments presented above. However, when vesicles were begun in such configurations (in, e.g., a spherocylindrical shape), high curvature was stable and these vesicles did not expand into spheres. This result provides some evidence that shape transformations could involve free energy barrier crossing events

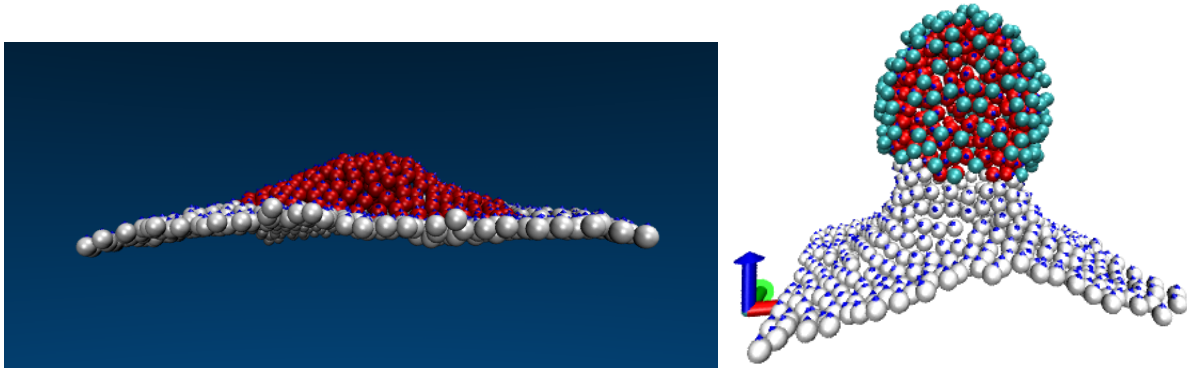


Figure 2.4: Physically realistic values of line tension can drive curvature in small systems. (left) This microstate from a membrane domain simulation with no proteins adhered exemplifies how appreciable curvature in the domain can become probable due to reductions in line tension free energy. (right) With high densities of proteins adhered, higher curvatures than those predicted by arguments discussed in section 2.2 can be achieved because the cinching seen here reduces the domain boundary. Above, $\eta = 0.32$ when the membrane is flat and changes with curvature throughout the trajectory.

in our model.

For all tests described above, as well as many others, we always observed membranes adopting spherical curvature (i.e., curvature that is typically symmetric about a point on the surface). These results are in contrast with the apparent observations from Stachowiak *et al.*, which seemed to show membranes adopting tubular membrane shapes. We discuss this discrepancy in the following section.

2.4 Spherical vs. spherocylindrical curvature

Stachowiak *et al.*'s results appear to show tubules as the dominant morphology generated in their systems. This preference is most clear in the earlier publication [75] where the membrane protrusion has a distinct and stable directionality (see Figure 2.1). In the second work, though morphologies are more complex, cryo-electron microscopy was used to observe tubules below the diffraction limit of fluorescence microscopy. Despite these observations, in simulation the spontaneous formation of tubular or spherocylindrical shapes remained elusive.

To begin to understand the conditions under which tubules are more stable than spheres we computed the total free energy of these shapes using our model,

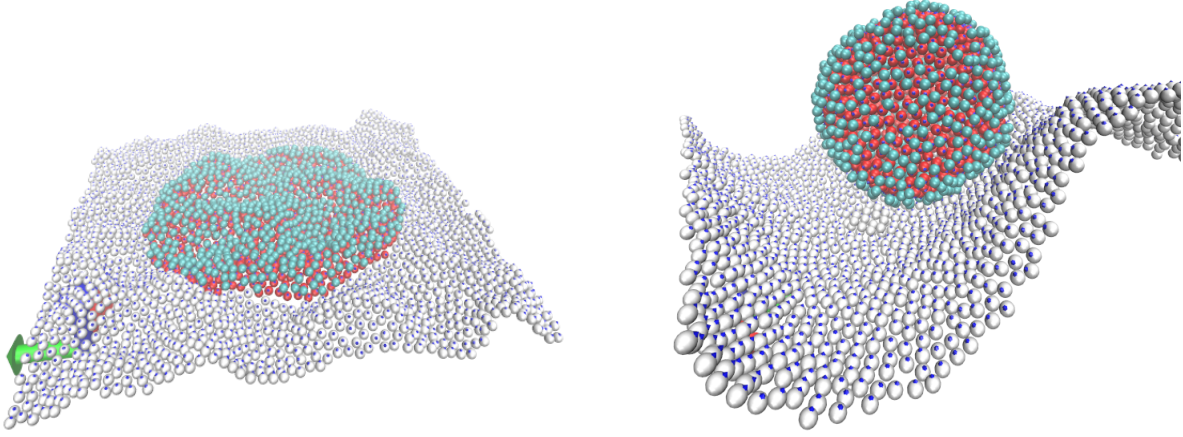


Figure 2.5: At considerably high densities of adhered proteins (here, $\eta = 0.42$ when the membrane is flat and changes with curvature throughout the trajectory) vesicle formation can be readily observed by the mechanism discussed here. This is aided somewhat by the line tension driving force discussed in section 3.5.2. These screenshots also how display fluctuation modes of a characteristic length scale amplify due to substantial membrane tension during the vesicle formation trajectory.

$$\begin{aligned}
 F &= F_{\text{mem}}(A, R) + F_{\text{prot}}(\bar{A}, \eta) \\
 &= \int dA \left[\frac{\kappa}{2} \left(\frac{1}{R_1} + \frac{1}{R_2} - c_0 \right)^2 \right] - \int d\bar{A} p
 \end{aligned} \tag{2.5}$$

For consistent shapes like spherocylinders or spheres, the curvature radius R is constant over the membrane surface and the integrals above become simple expressions,

$$\begin{aligned}
 \int dA &= A_{\text{sphere}} = 4\pi R^2 \\
 \int dA &= A_{\text{spherocyl}} = 2\pi RL + 4\pi R^2
 \end{aligned}$$

Similarly for the protein layer area, if we assume that the pressure is constant across the protein layer surface,

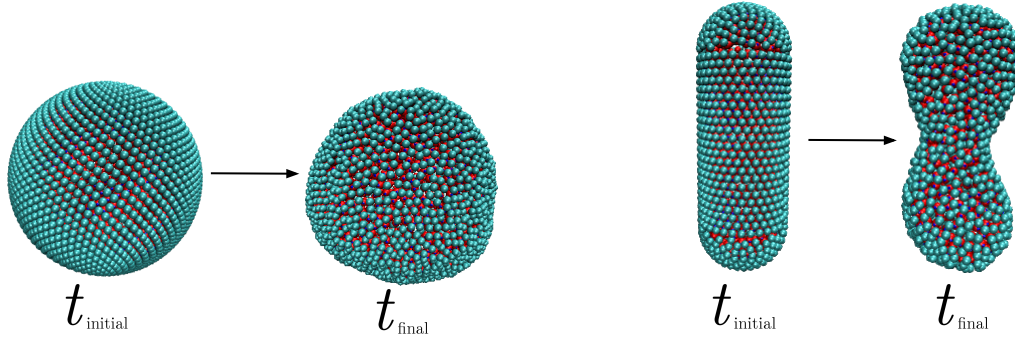


Figure 2.6: Observed final morphologies depend on starting configurations during the simulation period. (left) A vesicle with adhered proteins, started in a spherical configuration. $\left(\frac{N_{\text{prot}}}{A_{\text{mem}}} = 0.93 \text{ prots}/\sigma^2\right)$. Assuming that this geometry is still approximately spherical, the radius is $\sim 32.5 \text{ nm}$ and the protein layer packing fraction is $\eta \approx 0.636$. (right) A vesicle with adhered proteins, started in a spherocylindrical configuration $\left(\frac{N_{\text{prot}}}{A_{\text{mem}}} = 0.80 \text{ prots}/\sigma^2\right)$. Though these systems feature similar numbers of proteins per membrane area, they do not reach similar configurations or curvatures during the simulation period. The spherical configuration in particular displays a curvature lower than predicted given the high density of proteins adhered. This may indicate that a sphere-to-spherocylinder transition requires a rearrangement of particles that is improbable on the timescale observed.

$$\begin{aligned}
 \int d\bar{A} &= \bar{A}_{\text{sphere}} = 4\pi(R+l)^2 \\
 &= 4\pi(R^2 + 2Rl + l^2) \\
 &= A_{\text{sphere}} \left(1 + \frac{2l}{R} + \frac{l^2}{R^2}\right)
 \end{aligned}$$

$$\begin{aligned}
 \int d\bar{A} &= \bar{A}_{\text{spherocyl}} = \bar{A}_{\text{tube}} + \bar{A}_{\text{sphere}} \\
 &= 2\pi(R+l)L + 4\pi(R+l)^2 \\
 &= A_{\text{tube}} \left(1 + \frac{l}{R}\right) + A_{\text{sphere}} \left(1 + \frac{2l}{R} + \frac{l^2}{R^2}\right) \\
 &= (A + 4\pi Rl) \left(1 + \frac{l}{R}\right)
 \end{aligned}$$

We can determine which geometry has lowest shape by determining a form for p in

equation 2.5. However, we have 2 simultaneous equations for the pressure as a function of curvature radius, which we must solve self consistently. The first comes from minimizing equation 2.1 with respect to R_0 and solving for p .

$$p_{\text{spherocyl}}(R) = \frac{\kappa A}{AlR - 4\pi lR^3}$$

$$p_{\text{sphere}}(R) = \frac{4\kappa}{\sigma(R+l)}$$

The second arises because the pressure of the protein layer is dependent on its area \bar{A} , which is determined by geometry. We attain this by applying the Carnahan-Starling equation once again to get $p_{\text{CS}}(\eta)$, where η is a function of the radius,

$$p_{\text{spherocyl}}(R) = p_{\text{CS}} \left(\eta(R) = \frac{N_{\text{pro}} A_{\text{pro}}}{A(1 + \frac{\sigma}{R} + \frac{\sigma^2}{R^2})} \right)$$

$$p_{\text{sphere}}(R) = p_{\text{CS}} \left(\eta(R) = \frac{N_{\text{pro}} A_{\text{pro}}}{(A + 4\pi Rl)(1 + \frac{l}{R})} \right)$$

where A_{pro} is the projected area of a single protein and we have noted that the packing fraction $\eta(R) = \frac{N_{\text{pro}} A_{\text{pro}}}{A(R)}$.

Using this simple model, we determined which of the 2 geometries has the lowest free energy and then plotted the curvature radius of this geometry as a function of η (Figure 2.7). Though this does not accurately predict observations in our simulation – spherocylinders are seemingly predicted where only spherical shapes are observed – some useful trends are evident. Most importantly, it shows that tubules become more stable as the system size increases. This finding is reasonable because, for a spherocylinder with a given curvature radius R , as A_{mem} increases there is a higher ratio of cylindrical to spherical curvature in such vesicles. Cylindrical morphologies are favorable since they have half of the mean curvature of spherical morphologies (i.e., one of the principle curvatures in equation 1.1 is equal to zero). This supports the observed discrepancy that tubules are harder to observe in simulations, which are much smaller than experiments.

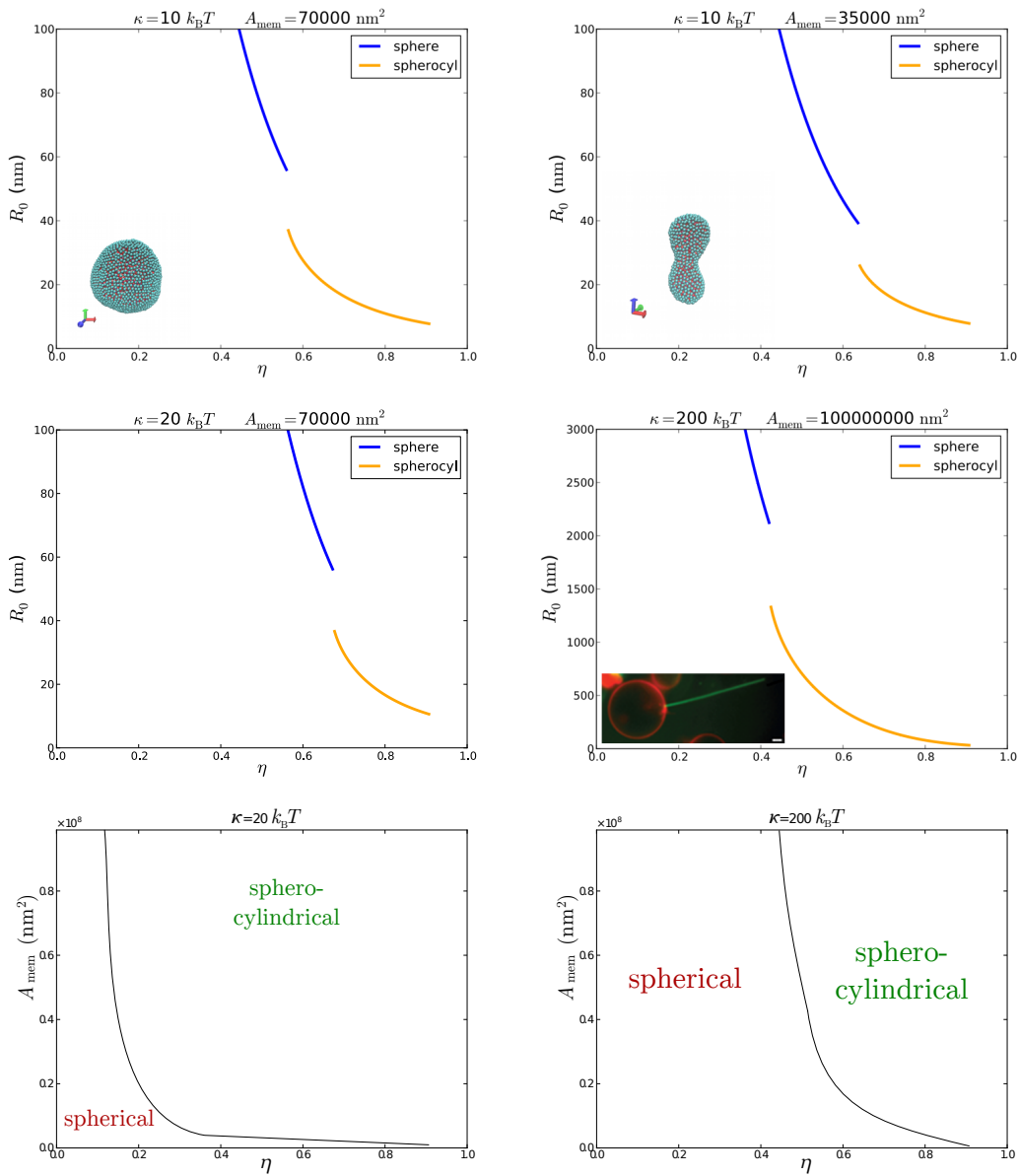


Figure 2.7: Simple modeling suggests that spherocylindrical vesicles become more stable than spheres as η and A_{mem} increase and as κ decreases. The top 4 plots were made by computing the total free energy for both spheres and tubules, then plotting the curvature radius of the shape with the lowest free energy. Inset images in 3 of these upper plots show simulations or experiments of system conditions corresponding to the plot parameters, however these do not necessarily exhibit accurate agreement. Upper two images are from Figure 2.6, center right image is from experiments in [75] (η unknown). In the bottom 2 plots, we use the methods above to predict morphological phase diagrams for $\kappa = 20k_B T$ and $200k_B T$ (typical fluid phase and gel phase rigidities) as a function of A_{mem} and η .

Chapter 3

Brownian dynamics simulations of fluctuating membranes at large lengthscales

3.1 Motivation

Numerical simulation has become an indispensable tool for examining the material properties of membranes and other soft materials. Such techniques are commonly used when theoretical models are challenging or impossible to analyze theoretically in ways that address research questions of interest. Though there has been some success in the direct hydrodynamical simulation of the approximated Helfrich free energy and other physical models [70], computational studies of membrane biophysics typically employ some form of molecular simulation such as Metropolis Monte Carlo or molecular dynamics [61].

There are a great variety of coarse-grained models available for molecular simulation of membranes [81]. At the highest levels of detail the membrane is resolved atomistically as a collection of lipid molecules self-assembled into a bilayer and surrounded by water and ions. However, the great computational cost of such models prohibit their use for many applications. This challenge has influenced the development of other models that abstract chemical detail at the cost of some physical properties. For example, coarse-grained lipid models in which the carbon chains of lipids are represented as 1 tail typically show only a liquid-solid phase transition, while more complex phase behavior is generally thought to require 2-tailed coarse grained models. In general, common tests for coarse-grained models verify that they obey the correct q -space dependence of height fluctuations modes, their mechanical properties are tunable, and they readily self-assemble due to modeled hydrophobic effects.

To access the time- and length-scales necessary to study protein layer effects on membrane bending mechanics we use a highly coarse-grained, solvent-free model recently developed in our group [66]. The work presented here required considerable extension of this model as

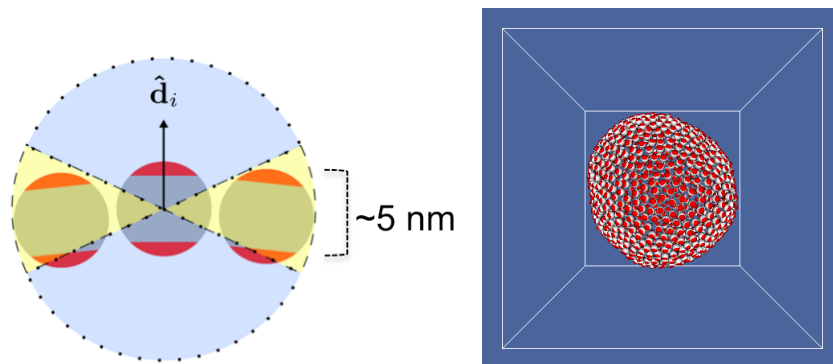


Figure 3.1: The membrane patch model of Pasqua *et al.* [66]. This meshless, solvent-free membrane model consists of a single layer of particles defined by their position and orientation. (left) Schematic showing a membrane particle 5 nm in diameter. Yellow shading corresponds to the equatorial neighbor region, blue shading corresponds to the polar neighbor region. (right) A vesicle configuration.

well as a non-trivial derivation of force terms for use with Brownian dynamics integrators. This section describes these additions, and source code can be provided upon request.

Note, the respective membrane-membrane and protein-membrane potentials described below contain parameters that have both the same name and meaning (e.g., r_a , z_b , etc). For notational simplicity, when referring to these parameters I only specify which potential these parameters belong to when this is ambiguous given the surrounding text. Otherwise, additional specifiers are used (e.g., $r_{a,\text{pro}}$, $z_{b,\text{mem}}$, etc).

3.2 The membrane patch model

The solvent-free, meshless “membrane patch” model developed by Pasqua *et al.* was designed to reproduce curvature fluctuation statistics using as few degrees of freedom as possible. The model is thus suitable for studying large-scale remodeling processes similar to those seen throughout cell biology and was inspired as an improvement upon a previous membrane model by Drouffe *et al.* [82]. Each particle is a membrane spanning sphere representing a 5 nm \times 5 nm patch of bilayer and is characterized by an orientational and translation degree of freedom. The basic form of the potential mimics the hydrophobic properties of bilayers. Though the underlying N -body potential energy equation is heuristic and cannot be derived from first principles, the large-scale bending mechanics of membranes emerges from these interactions (as demonstrated in section 3.7.1). The emergence of well-defined large scale material properties from heuristic microscopic interactions is a hallmark of many successful membrane models.

To allow for fluidity among the constituent particles of the membrane the model employs

an N -body potential rather than a pairwise potential. This potential has the following form,

$$\mathcal{U} = \mathcal{U}_{\text{HC}} + \epsilon \sum_{i=1}^N A_{\text{eq}}(n_{\text{eq}}^{(i)}) - A_{\text{pol}}(n_{\text{pol}}^{(i)}) \quad (3.1)$$

where \mathcal{U} is the total potential energy of the system, \mathcal{U}_{HC} (“hard-core”) enforces the steric constraint that no two particles overlap, N is the number of particles in the system, the terms to the right of the summation sign (further described below) mimic the hydrophobic penalty, and ϵ is a parameter that scales the size of this penalty.

Together, the functions A_{eq} and A_{pol} mimic the thermodynamic driving force influencing the hydrocarbon tails of lipids to point away from the aqueous solvent and the charged head groups of lipids to point toward the solvent (i.e., the hydrophobic effect). Given an orientation vector that points toward the particle’s “North pole”, The A_{eq} term counts the number of equatorial neighboring particles and contributes an energetic penalty if there are too few. Similarly, the A_{pol} term counts polar neighbors to energetically penalize any particles preventing head groups from (implicit) solvent exposure (see Figure 3.1). In equations, this leads to:

$$A_{\text{eq}}(n_{\text{eq}}) = \begin{cases} 1 - \frac{n_{\text{eq}}}{\bar{n}_{\text{eq}}} & , 0 \leq n_{\text{eq}} \leq \bar{n}_{\text{eq}} \\ 0 & , n \geq \bar{n}_{\text{eq}} \end{cases}$$

$$A_{\text{pol}}(n_{\text{pol}}) = \begin{cases} 1 - \frac{n_{\text{pol}}}{\bar{n}_{\text{pol}}} & , 0 \leq n_{\text{pol}} \leq \bar{n}_{\text{pol}} \\ 0 & , n \geq \bar{n}_{\text{pol}} \end{cases}$$

The input parameters \bar{n}_{eq} and \bar{n}_{pol} correspond to threshold numbers of equatorial and polar neighboring particles, respectively. If a particle has fewer than \bar{n}_{eq} neighbors along its equatorial (i.e., hydrophobic) region, there is a positive energetic cost. This form penalizes implicit solvent exposure to the hydrophobic region. This penalty increases linearly between 0 and 1 as n_{eq} decreases further from \bar{n}_{eq} . Similarly, if a particle has greater than 0 polar neighbors, this is penalized linearly between 0 and 1 as this number grows from 0 to a maximum of \bar{n}_{pol} .

Neighbor counting is achieved for each particle using the additional G and H functions, which are dependent on interparticle distance and orientation respectively,

$$n_{\text{eq}}^{(i)} = \sum_{j \neq i} G_{\text{eq}}(r_{ij}^2) H_{\text{eq}}(z_{ij}^2)$$

$$n_{\text{pol}}^{(i)} = \sum_{j \neq i} G_{\text{pol}}(r_{ij}^2) H_{\text{pol}}(z_{ij}^2) \quad (3.2)$$

where r_{ij} is the magnitude of the separation vector $\mathbf{r}_{ij} = \mathbf{r}_j - \mathbf{r}_i$ and $z_{ij} = \mathbf{r}_{ij} \cdot \hat{\mathbf{e}}_i / r_{ij}$ is the normalized projection of particle i 's orientation vector $\hat{\mathbf{e}}_i$ onto the separation vector \mathbf{r}_{ij} . Below, the subscript indices i and j for these variables and others may be dropped for notational simplicity.

Whether a particle j that is nearby to a particle i is classified as a “polar” or “equatorial” neighbor is determined by the forms of G and H . The function G decays from 1 to 0 linearly in r_{ij}^2 between r_a^2 and r_b^2 , where r_a and r_b are input parameters. The H function is similarly designed, however it depends on the normalized projection of particle i 's orientation vector onto the separation vector,

$$G_{\text{eq}}(r^2) = G_{\text{pol}}(r^2) = \begin{cases} 1 & \text{if } r^2 \leq r_a^2 \\ 0 & \text{if } r^2 \geq r_b^2 \\ \frac{r_b^2 - r^2}{r_b^2 - r_a^2} & \text{otherwise} \end{cases}$$

$$H_{\text{eq}}(z^2) = 1 - H_{\text{pol}}(z^2) = \begin{cases} 1 & \text{if } z^2 \leq z_a^2 \\ 0 & \text{if } z^2 \geq z_b^2 \\ \frac{z_b^2 - z^2}{z_b^2 - z_a^2} & \text{otherwise} \end{cases}$$

Though the form and logic of these equations may not be immediately apparent in equations, a clearer understanding may be achieved in illustrations (fig. 3.1) and plots (fig. 3.2).

3.3 Adapting the membrane patch potential for dynamical integrators

The potential published by Pasqua *et al.* is not amenable to dynamical integrators (i.e., those required for molecular dynamics or Langevin dynamics simulations) because it is not smoothly varying. Its forms for A , G , and H are instead piecewise discontinuous in their first derivatives. Numerical errors accrue since these integrators require forces, the first spatial derivative of the potential, to be computed and these forces are discontinuous with interparticle distance. (These integrators are typically based on expansions that are approximately accurate only when the underlying force functions are slowly varying.)

Since the specific form of the original potential was chosen only for simplicity, we choose here similar but smoothly-varying functions cubic in r and z to replace them,

$$G_{\text{eq}}(r^2) = G_{\text{pol}}(r^2) = \begin{cases} 1 & \text{if } r \leq r_a \\ 0 & \text{if } r \geq r_b \\ -\frac{2}{(r_a - r_b)^3} (r - r_b)^2 \left(r - \frac{3r_a - r_b}{2}\right) & \text{otherwise} \end{cases} \quad (3.3)$$

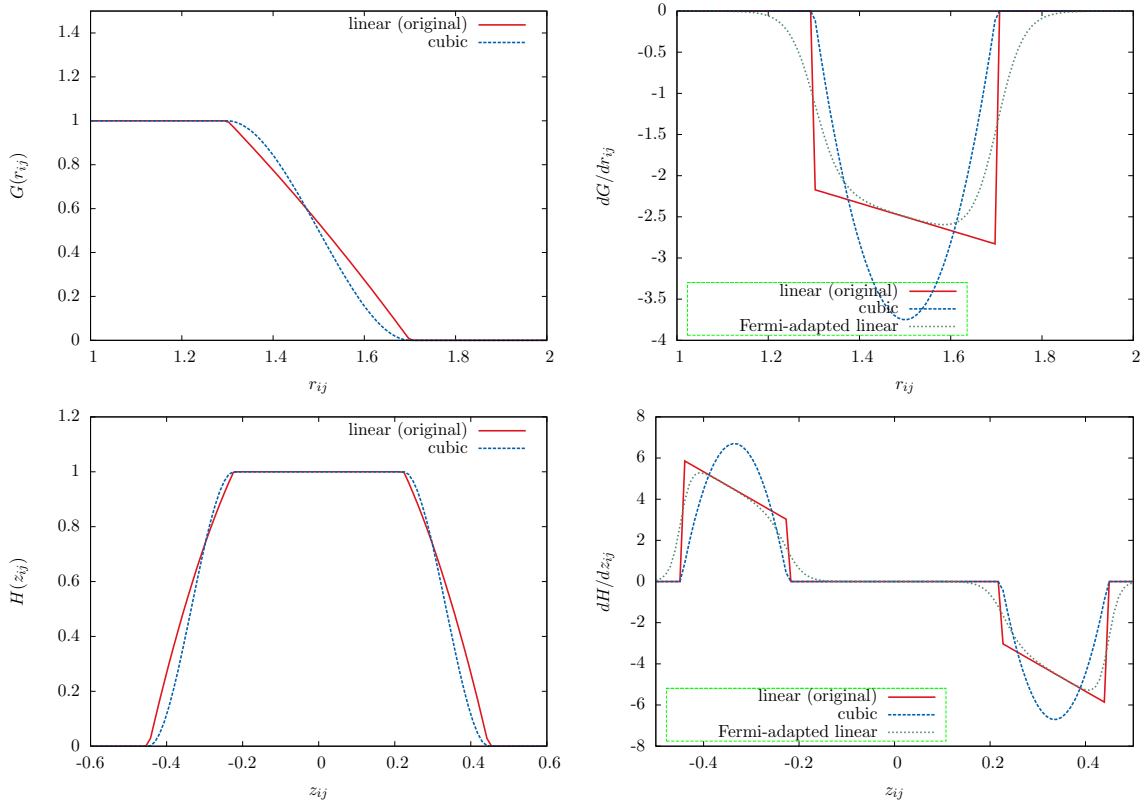


Figure 3.2: The G and H functions nested in the membrane patch potential. The original functions that comprise the model are piecewise and linear. Force equations derived from them are thus discontinuous and unsuitable for molecular/Brownian dynamics. The cubic equations that we replaced the original forms with are plotted here for comparison, along with a Fermi-function adaptation of the original functional forms (right plots).

$$H_{\text{eq}}(z) = 1 - H_{\text{pol}}(z) = \begin{cases} 1 & \text{if } -z_a \leq z \leq z_a \\ 0 & \text{if } -z_b \geq z \geq z_b \\ -\frac{2}{(z_a - z_b)^3} (|z| - z_b)^2 \left(|z| - \frac{3z_a - z_b}{2}\right) & \text{otherwise} \end{cases} \quad (3.4)$$

These functions and their first derivatives are plotted in figure 3.2. Usage of these cubic forms makes the derivatives for G and H piecewise continuous. Further similarity to the original potential can be achieved using Fermi functions ($f(x) = 1/(e^{\beta(x-x_0)} + 1)$, where β and x_0 are parameters) within the original piecewise construction (see, again, figure 3.2),

however this form appears to confer no significant advantage to the model (data not shown) and might be less computationally efficient.

A_{eq} and A_{pol} must also have piecewise continuous derivatives for numerical stability. We adopt the following cubic forms for them, similar to those above:

$$A_{\text{eq}}(n_{\text{eq}}) = \begin{cases} \frac{2}{\bar{n}_{\text{eq}}^3} (n_{\text{eq}} - \bar{n}_{\text{eq}})^2 (n_{\text{eq}} + \frac{\bar{n}_{\text{eq}}}{2}) & , 0 \leq n_{\text{eq}} \leq \bar{n}_{\text{eq}} \\ 0 & , n \geq \bar{n}_{\text{eq}} \end{cases}$$

$$A_{\text{pol}}(n_{\text{pol}}) = \begin{cases} \frac{2}{\bar{n}_{\text{pol}}^3} (n_{\text{pol}} - \bar{n}_{\text{pol}})^2 (n_{\text{pol}} + \frac{\bar{n}_{\text{pol}}}{2}) & , 0 \leq n_{\text{pol}} \leq \bar{n}_{\text{pol}} \\ 0 & , n \geq \bar{n}_{\text{pol}} \end{cases}$$

In the original model, the hard core steric potential \mathcal{U}_{HC} may be implemented simply by disallowing particle overlap during Metropolis Monte Carlo position updates. For dynamical integrators, this may be replaced by the Weeks-Chandler-Anderson (WCA) potential [83]

$$\mathcal{U}_{\text{WCA}} = \begin{cases} 4\epsilon \left[\left(\frac{\sigma}{r}\right)^{12} - \left(\frac{\sigma}{r}\right)^6 \right] + \epsilon & 0 \leq r \leq 2^{\frac{1}{6}}\sigma \\ 0 & \text{otherwise} \end{cases}$$

This potential is a truncated and shifted Lennard-Jones potential [61] that essentially retains only steric repulsive interactions.

3.4 Deriving N -body force equations

To derive force equations suitable for dynamical computational integrators, we take the first spatial derivative of the N -body potential given by equation 3.1 using the substituted equations discussed above. Since this derivation is non-trivial, we describe this in some detail here. Below the notation $\nabla_{\mathbf{r}_{ij}} = \left(\frac{\partial}{\partial x} \hat{\mathbf{x}} + \frac{\partial}{\partial y} \hat{\mathbf{y}} + \frac{\partial}{\partial z} \hat{\mathbf{z}} \right)$ is the first spatial gradient.

Translational force. The total translational force on particle i due to particle j has

the following form,

$$\begin{aligned}
-\mathbf{f}_{ij} &= \nabla_{\mathbf{r}_{ij}} \mathcal{U} \\
&= \nabla_{\mathbf{r}_{ij}} \mathcal{U}_{\text{WCA}} + \epsilon \left[\nabla_{\mathbf{r}_{ij}} A_{\text{eq}} - \nabla_{\mathbf{r}_{ij}} A_{\text{pol}} \right] \\
&= \nabla_{\mathbf{r}_{ij}} \mathcal{U}_{\text{WCA}} + \epsilon \left[\left(\frac{\partial A_{\text{eq}}^{(i)}}{\partial n_{\text{eq}}^{(i)}} \right) (\nabla_{\mathbf{r}_{ij}} n_{\text{eq}}) - \left(\frac{\partial A_{\text{pol}}^{(i)}}{\partial n_{\text{pol}}^{(i)}} \right) (\nabla_{\mathbf{r}_{ij}} n_{\text{pol}}) \right] \\
&= \nabla_{\mathbf{r}_{ij}} \mathcal{U}_{\text{WCA}} + \epsilon \left[\left(\frac{\partial A_{\text{eq}}^{(i)}}{\partial n_{\text{eq}}^{(i)}} \right) \left(\sum_{i \neq j} \nabla_{\mathbf{r}_{ij}} (G_{\text{eq}} H_{\text{eq}}) \right) \right. \\
&\quad \left. - \left(\frac{\partial A_{\text{pol}}^{(i)}}{\partial n_{\text{pol}}^{(i)}} \right) \left(\sum_{i \neq j} \nabla_{\mathbf{r}_{ij}} (G_{\text{pol}} H_{\text{pol}}) \right) \right] \\
-\mathbf{f}_{ij} &= \nabla_{\mathbf{r}_{ij}} \mathcal{U}_{\text{WCA}} + \epsilon \left[\left(\frac{\partial A_{\text{eq}}^{(i)}}{\partial n_{\text{eq}}^{(i)}} \right) (G_{\text{eq}}^{(i,j)} (\nabla_{\mathbf{r}_{ij}} H_{\text{eq}}^{(i,j)}) + H_{\text{eq}}^{(i,j)} (\nabla_{\mathbf{r}_{ij}} G_{\text{eq}}^{(i,j)})) \right. \\
&\quad \left. - \left(\frac{\partial A_{\text{pol}}^{(i)}}{\partial n_{\text{pol}}^{(i)}} \right) (G_{\text{pol}}^{(i,j)} (\nabla_{\mathbf{r}_{ij}} H_{\text{pol}}^{(i,j)}) + H_{\text{pol}}^{(i,j)} (\nabla_{\mathbf{r}_{ij}} G_{\text{pol}}^{(i,j)})) \right] \tag{3.5}
\end{aligned}$$

As we see shortly, the $\left(\frac{\partial A}{\partial n}\right)$ terms above are dependent on n . This means that, before any pairwise forces can be calculated, a loop over all particle pairs must be completed in order to sum up equatorial and polar neighbors for all particles via the G and H equations (more on this implementation in section 3.4.1).

Here, we derive forms for each term in the equation above. As before, we suppress notation for simplicity when such information is implicit in the discussion.

$$\nabla_{\mathbf{r}_{ij}} \mathcal{U}_{\text{WCA}} = \frac{\partial \mathcal{U}_{\text{WCA}}}{\partial \mathbf{r}} = \left(\frac{\partial \mathcal{U}_{\text{WCA}}}{\partial r} \right) \left(\frac{\partial \mathbf{r}}{\partial \mathbf{r}} \right)$$

$$\begin{aligned}
\frac{\partial \mathcal{U}_{\text{WCA}}}{\partial r} &= \left(4\epsilon \left[12 \left(\frac{\sigma}{r} \right)^{11} \left(-\frac{\sigma}{r^2} \right) - 6 \left(\frac{\sigma}{r} \right)^5 \left(-\frac{\sigma}{r^2} \right) \right] \right) \\
&= \frac{24\epsilon}{r} \left[2 \left(\frac{\sigma}{r} \right)^{12} - \left(\frac{\sigma}{r} \right)^6 \right]
\end{aligned}$$

$$\begin{aligned}\frac{\partial r}{\partial \mathbf{r}} &= \frac{1}{2} \frac{2r_x}{\sqrt{r_x^2 + r_y^2 + r_z^2}} \hat{x} + \frac{1}{2} \frac{2r_y}{\sqrt{r_x^2 + r_y^2 + r_z^2}} \hat{y} + \frac{1}{2} \frac{2r_z}{\sqrt{r_x^2 + r_y^2 + r_z^2}} \hat{z} \\ &= \frac{\mathbf{r}}{r}\end{aligned}\quad (3.6)$$

$$\begin{aligned}\nabla_{\mathbf{r}_{ij}} \mathcal{U}_{\text{WCA}} &= \left(\frac{24\epsilon}{r} \left[2 \left(\frac{\sigma}{r} \right)^{12} - \left(\frac{\sigma}{r} \right)^6 \right] \right) \left(\frac{\mathbf{r}}{r} \right) \\ &= \frac{24\epsilon}{r^2} \left[2 \left(\frac{\sigma}{r} \right)^{12} - \left(\frac{\sigma}{r} \right)^6 \right] (\mathbf{r})\end{aligned}\quad (3.7)$$

where

$$\begin{aligned}\mathbf{r} &= \mathbf{r}_j - \mathbf{r}_i \\ &\equiv (r_x, r_y, r_z)\end{aligned}\quad (3.8)$$

and

$$r = \sqrt{r_x^2 + r_y^2 + r_z^2}\quad (3.9)$$

$$\begin{aligned}\frac{\partial A_{\text{eq}}}{\partial n_{\text{eq}}} &= \frac{2}{\bar{n}_{\text{eq}}^3} \left((n_{\text{eq}} - \bar{n}_{\text{eq}})^2 + \left(n_{\text{eq}} + \frac{\bar{n}_{\text{eq}}}{2} \right) \cdot 2(n_{\text{eq}} - \bar{n}_{\text{eq}}) \right) \\ &= \frac{2}{\bar{n}_{\text{eq}}^3} (n_{\text{eq}} - \bar{n}_{\text{eq}}) (n_{\text{eq}} - \bar{n}_{\text{eq}} + 2n_{\text{eq}} + \bar{n}_{\text{eq}}) \\ &= \frac{6}{\bar{n}_{\text{eq}}^3} n_{\text{eq}} (n_{\text{eq}} - \bar{n}_{\text{eq}})\end{aligned}\quad (3.10)$$

Similarly,

$$\frac{\partial A_{\text{pol}}}{\partial n_{\text{pol}}} = \frac{6}{\bar{n}_{\text{pol}}^3} n_{\text{pol}} (n_{\text{pol}} - \bar{n}_{\text{pol}})\quad (3.11)$$

$$\nabla_{\mathbf{r}_{ij}} G_{\text{eq}} = \frac{\partial G_{\text{eq}}}{\partial \mathbf{r}} = \left(\frac{\partial G_{\text{eq}}}{\partial r} \right) \left(\frac{\partial r}{\partial \mathbf{r}} \right)$$

$$\begin{aligned} \frac{\partial G_{\text{eq}}}{\partial r} &= -\frac{2}{(r_a - r_b)^3} \left((r - r_b)^2 + 2 \left(r - \frac{3r_a - r_b}{2} \right) (r - r_b) \right) \\ &= -\frac{2}{(r_a - r_b)^3} (r - r_b) (r - r_b + 2r - 3r_a - r_b) . \\ &= -\frac{2}{(r_a - r_b)^3} (r - r_b) (3r - 3r_a) \\ &= -\frac{6}{(r_a - r_b)^3} (r - r_b) (r - r_a) \end{aligned}$$

$$\nabla_{\mathbf{r}_{ij}} G_{\text{eq}} = \left(-\frac{6}{(r_a - r_b)^3} (r - r_b) (r - r_a) \right) \left(\frac{\mathbf{r}}{r} \right) \quad (3.12)$$

$$\nabla_{\mathbf{r}_{ij}} G_{\text{pol}} = \nabla_{\mathbf{r}_{ij}} G_{\text{eq}}$$

$$\nabla_{\mathbf{r}_{ij}} H_{\text{eq}} = \frac{\partial H_{\text{eq}}}{\partial \mathbf{r}} = \left(\frac{\partial H_{\text{eq}}}{\partial z} \right) \left(\frac{\partial z}{\partial \mathbf{r}} \right)$$

$$\begin{aligned} \frac{\partial H_{\text{eq}}}{\partial z} &= -\frac{2}{(z_a - z_b)^3} \left((z - z_b)^2 + 2 \left(z - \frac{3z_a - z_b}{2} \right) (z - z_b) \right) \\ &= -\frac{2}{(z_a - z_b)^3} (z - z_b) (z - z_b + 2z - 3z_a - z_b) . \\ &= -\frac{2}{(z_a - z_b)^3} (z - z_b) (3z - 3z_a) \\ &= -\frac{6}{(z_a - z_b)^3} (z - z_b) (z - z_a) \end{aligned}$$

$$\begin{aligned}\frac{\partial H_{\text{pol}}}{\partial z} &= \frac{\partial}{\partial z} (1 - H_{\text{eq}}) \\ &= -\frac{\partial H_{\text{eq}}}{\partial z}\end{aligned}$$

$$\begin{aligned}\frac{\partial z}{\partial \mathbf{r}} &= \frac{\partial}{\partial \mathbf{r}} \left(\frac{\mathbf{r} \cdot \hat{\mathbf{e}}}{r} \right) \\ &= \frac{1}{r} \cdot \hat{\mathbf{e}} + (\nabla_{\mathbf{r}_{ji}} r^{-1}) (\mathbf{r} \cdot \hat{\mathbf{e}}) \\ &= \frac{\hat{\mathbf{e}}}{|r|} + \left(-r^{-2} \left(\frac{\mathbf{r}}{r} \right) \right) (\mathbf{r} \cdot \hat{\mathbf{e}}) \\ &= \frac{\hat{\mathbf{e}}}{r} - \frac{z\mathbf{r}}{r^2}\end{aligned}$$

$$\nabla_{\mathbf{r}_{ji}} H_{\text{eq}} = \left(-\frac{6}{(z_a - z_b)^3} (z - z_b)(z - z_a) \right) \left(\frac{\hat{\mathbf{e}}}{r} - \frac{z\mathbf{r}}{r^2} \right) \quad (3.13)$$

$$\nabla_{\mathbf{r}_{ji}} H_{\text{pol}} = -\nabla_{\mathbf{r}_{ji}} H_{\text{eq}}$$

where

$$z_{ij} = \frac{\mathbf{r}_{ij} \cdot \hat{\mathbf{e}}_i}{r_{ij}} \quad (3.14)$$

Torque. Because each particle features an orientational degree of freedom, the potential described above confers a torque about the center of mass of each particle. This torque can be expressed as [84]

$$\boldsymbol{\tau}_i = \hat{\mathbf{e}}_i \times \nabla_{\hat{\mathbf{e}}_i} \mathcal{U}_i$$

where $\hat{\mathbf{e}}_i$ is the unit vector specifying the orientation of particle i and $\nabla_{\hat{\mathbf{e}}_i} = \left(\frac{\partial}{\partial \epsilon_x} \hat{\mathbf{e}}_{\mathbf{x}} + \frac{\partial}{\partial \epsilon_y} \hat{\mathbf{e}}_{\mathbf{y}} + \frac{\partial}{\partial \epsilon_z} \hat{\mathbf{e}}_{\mathbf{z}} \right)$. For the potential described above, we can write the following expressions for the terms constituting this torque equation,

$$\begin{aligned}
\nabla_{\hat{\mathbf{e}}_i} \mathcal{U}_i &= \sum_{i \neq j} \nabla_{\hat{\mathbf{e}}_i} \mathcal{U}_{\text{WCA}}^0 + \epsilon (\nabla_{\hat{\mathbf{e}}_i} A_{\text{eq}} - \nabla_{\hat{\mathbf{e}}_i} A_{\text{pol}}) \\
&= \epsilon \left[\left(\frac{\partial A_{\text{eq}}}{\partial n_{\text{eq}}} \right) \left(\frac{\partial n_{\text{eq}}}{\partial \hat{\mathbf{e}}_i} \right) - \left(\frac{\partial A_{\text{pol}}}{\partial n_{\text{pol}}} \right) \left(\frac{\partial n_{\text{pol}}}{\partial \hat{\mathbf{e}}_i} \right) \right]
\end{aligned} \tag{3.15}$$

The forms for $\frac{\partial A_{\text{eq}}}{\partial n_{\text{eq}}}$ and $\frac{\partial A_{\text{pol}}}{\partial n_{\text{pol}}}$ were derived previously.

$$\begin{aligned}
\frac{\partial n_{\text{eq}}}{\partial \hat{\mathbf{e}}_i} &= \frac{\partial}{\partial \hat{\mathbf{e}}_i} (G_{\text{eq}}(\mathbf{r}) H_{\text{eq}}(z)) \\
&= G_{\text{eq}} \left(\frac{\partial H_{\text{eq}}(z)}{\partial \hat{\mathbf{e}}_i} \right) + H_{\text{eq}} \frac{\partial G_{\text{eq}}(r)}{\partial \hat{\mathbf{e}}_i} \\
&= G_{\text{eq}} \left(\frac{\partial H_{\text{eq}}(z)}{\partial z} \right) \left(\frac{\partial z}{\partial \hat{\mathbf{e}}_i} \right)
\end{aligned}$$

The term $\frac{\partial H_{\text{eq}}(z)}{\partial z}$ was also derived previously. Finally,

$$\frac{\partial z}{\partial \hat{\mathbf{e}}_i} = \frac{\partial}{\partial \hat{\mathbf{e}}_i} \left(\frac{\mathbf{r} \cdot \hat{\mathbf{e}}_i}{r} \right) = \frac{\mathbf{r}}{r}$$

which is equivalent to equation 3.6. Since $G_{\text{pol}} = G_{\text{eq}}$ and $\frac{\partial H_{\text{pol}}(z)}{\partial z} = -\frac{\partial H_{\text{eq}}(z)}{\partial z}$, the resulting forms for both terms are thus

$$\begin{aligned}
\frac{\partial n_{\text{eq}}}{\partial \hat{\mathbf{e}}_i} &= G_{\text{eq}} \left(\frac{\partial H_{\text{eq}}(z)}{\partial z} \right) \left(\frac{\mathbf{r}}{r} \right) \\
\frac{\partial n_{\text{pol}}}{\partial \hat{\mathbf{e}}_i} &= -\frac{\partial n_{\text{eq}}}{\partial \hat{\mathbf{e}}_i}
\end{aligned} \tag{3.16}$$

3.4.1 Algorithmic implementation & computational efficiency

To summarize the calculations necessary for force computation of the membrane-membrane potential, the stepwise algorithm is described here.

(Part A) Count the neighbors (i.e., calculate n_{eq} and n_{pol} for each particle):

for each particle i

 for each neighbor j

1. Calculate the distance vector \mathbf{r}_{ij} (eq. 3.8).
2. Calculate the normalized projections z_i and z_j of each particle's orientation vector over this interparticle separation (eq. 3.14).
3. Calculate $G_{\text{eq},i} = G_{\text{eq},j} = G_{\text{pol},i} = G_{\text{pol},j}$ (eq. 3.3), $H_{\text{eq},i} = 1 - H_{\text{pol},i}$, and $H_{\text{eq},j} = 1 - H_{\text{pol},j}$ (eq. 3.4).
4. Increment the equatorial neighbor count, n_{eq} , and the polar neighbor count, n_{pol} (eq. 3.2).

 endfor

endfor

(Part B) Calculate the pairwise forces

for each particle i

 for each neighbor j

1. If saved, re-acquire the following quantities: \mathbf{r}_{ij} , z_i , z_j , $G_{\text{eq},i} = G_{\text{eq},j} = G_{\text{pol},i} = G_{\text{pol},j}$, $H_{\text{eq},i} = 1 - H_{\text{pol},i}$, $H_{\text{eq},j} = 1 - H_{\text{pol},j}$ (this minimizes redundant calculation). Otherwise, recalculate them.
2. Calculate $\nabla_{\mathbf{r}_{ij}} \mathcal{U}_{\text{WCA}}$ if $r_{ij} < \sigma^{\frac{1}{6}}$ (eq. 3.7).
3. Calculate $\nabla_{\mathbf{r}_{ij}} G_{\text{eq},i} = \nabla_{\mathbf{r}_{ij}} G_{\text{eq},j} = \nabla_{\mathbf{r}_{ij}} G_{\text{pol},i} = \nabla_{\mathbf{r}_{ij}} G_{\text{pol},j}$ (eq. 3.12).
4. Calculate $\nabla_{\mathbf{r}_{ij}} H_{\text{eq},i} = -\nabla_{\mathbf{r}_{ij}} H_{\text{pol},i}$ and $\nabla_{\mathbf{r}_{ij}} H_{\text{eq},j} = -\nabla_{\mathbf{r}_{ij}} H_{\text{pol},j}$ (eq. 3.13).
5. Calculate $\nabla_{\mathbf{r}_{ij}} n_{\text{eq}}$ and $\nabla_{\mathbf{r}_{ij}} n_{\text{pol}}$ for particles i and j , where:

$$\begin{aligned} \nabla_{\mathbf{r}_{ij}} n_{\text{eq},i} &= G_{\text{eq},i} \nabla_{\mathbf{r}_{ij}} H_{\text{eq},i} + H_{\text{eq},i} \nabla_{\mathbf{r}_{ij}} G_{\text{eq},i} \\ \nabla_{\mathbf{r}_{ji}} n_{\text{eq},j} &= G_{\text{eq},j} \nabla_{\mathbf{r}_{ji}} H_{\text{eq},j} + H_{\text{eq},j} \nabla_{\mathbf{r}_{ji}} G_{\text{eq},j} \\ \nabla_{\mathbf{r}_{ij}} n_{\text{pol},i} &= G_{\text{pol},i} \nabla_{\mathbf{r}_{ij}} H_{\text{pol},i} + H_{\text{pol},i} \nabla_{\mathbf{r}_{ij}} G_{\text{pol},i} \\ \nabla_{\mathbf{r}_{ji}} n_{\text{pol},j} &= G_{\text{pol},j} \nabla_{\mathbf{r}_{ji}} H_{\text{pol},j} + H_{\text{pol},j} \nabla_{\mathbf{r}_{ji}} G_{\text{pol},j} \end{aligned}$$

6. Calculate $\frac{\partial A_{\text{eq}}}{\partial n_{\text{eq}}}$ (eq. 3.10) and $\frac{\partial A_{\text{pol}}}{\partial n_{\text{pol}}}$ (eq. 3.11) for particles i and j .
7. Calculate the translational force from particle i to j , \mathbf{f}_{ij} , and vice versa (eq. 3.5).

8. Calculate $\frac{\partial n_{\text{eq}}}{\partial \mathbf{e}}$ and $\frac{\partial n_{\text{pol}}}{\partial \mathbf{e}}$ (eq. 3.16) for particles i and j .
 9. Calculate the rotational force from particles i to j , and vice versa (eq. 3.15).
- endfor
endfor

Though the model described above abstracts many degrees of freedom, the lengthscales and timescales accessible using this model are nevertheless limited by available computational resources. We have not tested this performance rigorously, and these limits do not deter studies of many properties of membranes such as those analyzed in Chapter 4. However, for some studies of processes that involve large scale shape transformations, we anticipate that computational limits on system sizes may become an issue.

For example, Figure 3.3 shows that a typical large simulation studied during this research was $\sim 10^{-3}$ of the size of the corresponding experimental system. When a layer of adhered proteins was added to the domain seen in this figure, this took 3 to 4 weeks to produce configurations like those seen in Figure 2.5. Slow relaxation of curvature radii also prevented one method of spontaneous curvature computation and inspired the analysis in Section 3.7.2. Since we have predicted in Section 2.4 that system size is an important determinant of membrane morphology, extensions to the simulation source code that optimize computation or incorporate GPU acceleration could lead to increasingly relevant simulation studies.

3.5 Incorporating different lipid types

Though each membrane particle represents ~ 100 lipid molecules (a discrete $\sim 25 \text{ nm}^2$ patch of membrane), it is both physically meaningful and investigatively useful to incorporate two different lipid types in the model. Our main motivation was the better approximate the experimental conditions of Stachowiak *et al.* [75, 76], in which adhered proteins were confined to a domain of one lipid type that was surrounded by a larger membrane composed of a different lipid type. The morphological transformation observed in these studies depended on the rigidity of this domain, which differed from its surroundings, and may have been influenced by line tension at the domain boundary. We describe here the development and analysis of this “mem1-mem2” interaction potential.

3.5.1 The model

To mimic the tendency of unlike lipids to disassociate, we first compute the original potential described by Pasqua *et al.* (3.1) without modification to maintain hydrophobic properties. Additionally, we introduce a heuristic pairwise repulsion between, e.g., particle types A and

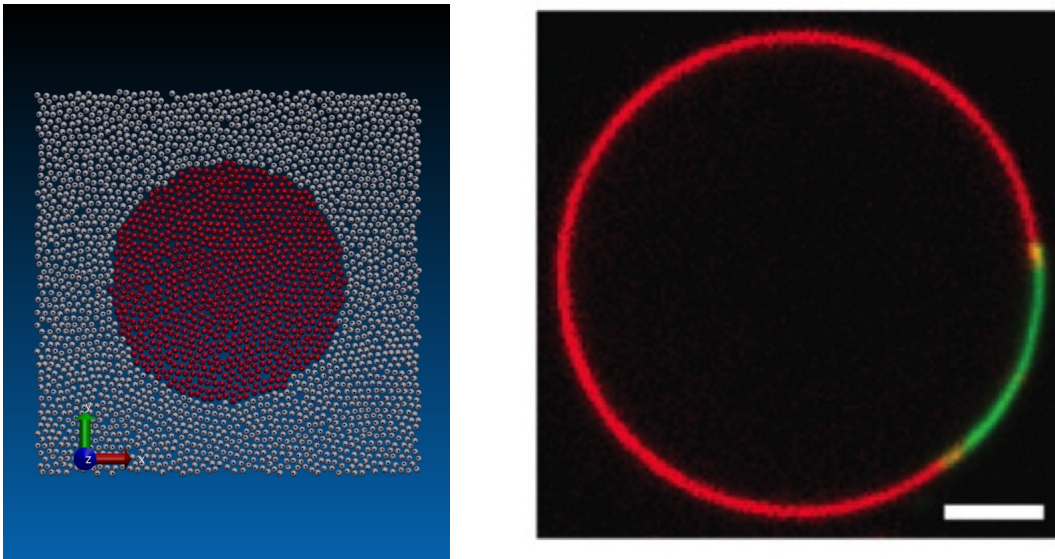


Figure 3.3: (left) A simulation of a membrane domain of particle type 2 surrounded by membrane particles of type 1. The “mem1-mem2” interaction potential is described by equation 3.17. The domain area is $A \approx 0.032\mu\text{m}^2$ and is typical of a large-sized simulation studied here. (right) For comparison, an experimental image of a giant unilamellar vesicle used in the experiment by our collaborators [75]. The domain area here is $A \approx 100\mu\text{m}^2$.

B (which are depicted as white particles and red particles, respectively, in figure 3.3). Since the $G(r_{ij})$ function (equations 3.3) is already computed, we make use of this monotonically decreasing function while using a different ϵ parameter to control the scale of the pairwise repulsion,

$$\mathcal{U}_{\text{lin}} = \begin{cases} \epsilon_{\text{lin}} \sum_{i<j} G(r_{ij}) & \text{if } i \text{ and } j \text{ are of different types} \\ 0 & \text{otherwise} \end{cases} \quad (3.17)$$

The gradient may be computed straightforwardly to get terms needed to compute forces and stress tensors. From this pairwise repulsion emerges a thermodynamic line tension that may be computed by analyzing 1-dimensional interfacial fluctuations along the domain boundary (see Subsection 3.5.2).

It should be noted that, since these terms are repulsive, sufficiently high values of $\epsilon_{\text{lin}}/k_{\text{B}}T$ may act to separate domains of particles A and B in space. This separation is conceptually similar to the formation of a vapor bubble at a hydrophobic interface. To maintain the tendency for A and B lipid types to demix while eliminating this issue, the repulsion term between unlike particles could be replaced with an attraction between like particles, thus leaving only attractive terms.

3.5.2 Domain boundary fluctuations and line tension measurements

As mentioned earlier, from the pairwise repulsion term emerges a line tension (λ). This property is thermodynamically defined as the free energetic cost per unit length of this domain boundary (e.g., $\lambda = (\partial F / \partial L)_{N,V,T}$, for a membrane domain in the $NV\lambda T$ ensemble). The line tension can be measured from interfacial fluctuations using methods analogous to those used to measure the bending rigidity and surface tension (see Section 3.7.1 for somewhat more discussion on these ideas). By defining the location (or, “height”) of this domain boundary in reference to its average circular shape (a Monge gauge approximation [10]; see Figure 3.4), the total line tension free energy of a domain boundary of length L may be written

$$F_{\text{line}} = \frac{\lambda}{2} \int_0^L dx \sqrt{1 + h_x^2} \quad (3.18)$$

expanding to second order, we can write equation 3.18 as

$$F_{\text{line}} = \frac{\lambda}{2} \int_0^L dx h_x^2.$$

Using the definitions $h_q = \frac{1}{L} \int h(x) e^{-iqx}$ and $h(x) = \sum_q h_q e^{iqx}$ for a forward and reverse Fourier transforms, this free energy becomes

$$F_{\text{line}} = \frac{\lambda}{2} L \left[\sum_q q^2 h_q^2 \right].$$

The free energy of each mode q is

$$\begin{aligned} F_{\text{line},q} &= \frac{\lambda}{2} L q^2 h_q^2 \\ \frac{1}{2} k_B T &= \frac{\lambda}{2} L q^2 \langle |h_q|^2 \rangle \end{aligned}$$

where the last line is due to the equipartition theorem [77]. Rearranging,

$$\langle |h_q|^2 \rangle = \frac{k_B T}{\lambda L q^2}.$$

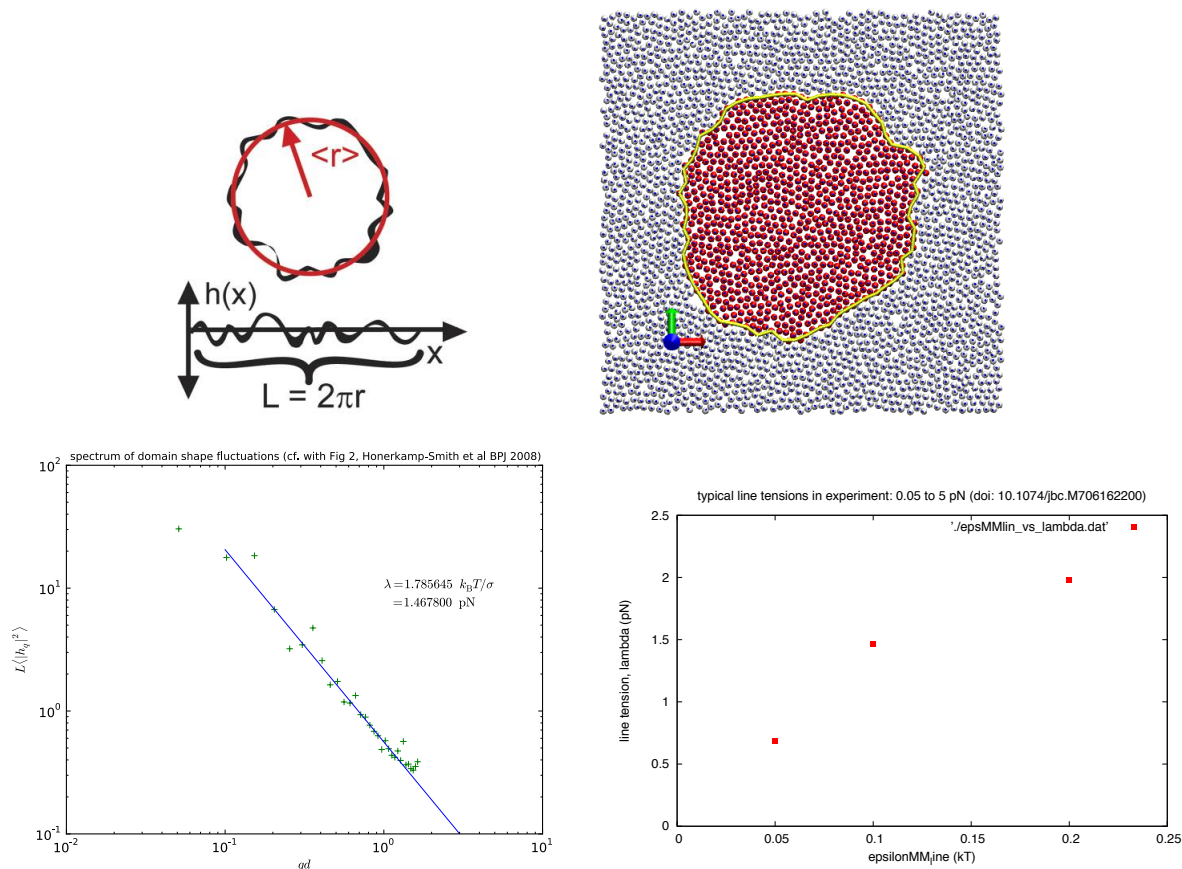


Figure 3.4: (top left) This schematic shows how domain boundary fluctuations are mapped to a single dimension for Fourier analysis. Adapted from [35]. (top right) An screenshot from a typical trajectory from which interfacial fluctuation data are gathered. The yellow line gives the interpolated domain boundary. (It should be noted that this calculation could be performed slightly more straightforwardly for a linear, rather than circular, domain interface.) (bottom left) An example of interfacial fluctuation measurements that are used to calculate λ . Confer with Figure 3.12. (bottom right) The y -values of this plot give line tension in units of piconewtons. This corresponds well with experimentally measured line tensions for lipid domains, which tend to be on the order of 10^{-1} pN to 10^0 pN [34, 35].

This equation, which is analogous to equation 3.21, is what may typically be fit to experimental or simulation data of interfacial fluctuations to calculate λ . These calculations for our membrane model (see Figure 3.4) showed that $\epsilon_{\text{lin}} = 0.1 k_B T$ in equation 3.17 yields a line tension of approximately $\lambda = 1.5$ pN. This value corresponds well with typical line tensions measured from experimental data [34, 35]. However, a main difference between our simulations and experiments is that the system sizes tested computationally are much

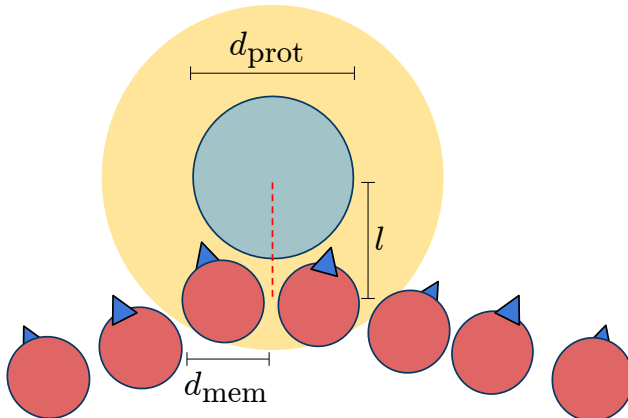


Figure 3.5: The protein-membrane potential was designed for this study to diffuse fluidly on the membrane surface and features a neighbor counting scheme similar to the one embedded in the membrane-membrane potential of Pasqua *et al.* [66]. The protein-protein potential includes only volume excluding interactions. The diameter of each particle representing a membrane patch (and, thus, also the membrane thickness) is $d_{\text{mem}} \equiv \sigma$, the diameter of protein particles are $d_{\text{mem}} = 2\sigma$. The protein layer height $l = (d_{\text{mem}} + d_{\text{mem}})/2 = 1.5\sigma$ was used for the analytical curve in Figure 4.2 and was verified numerically.

smaller. Because a much larger fraction of the system exists at the domain boundary, line tensions of such values, despite their physical meaningfulness, can play a major role in membrane bending observed (as discussed in Section 2.3).

3.6 The protein model

The protein-membrane potential was designed for consistency with the meshless membrane model presented earlier this chapter. This N -body potential is minimized when the number of membrane molecules with their polar faces toward the protein, $n_{\text{pol,pro}}$, is equal or greater to some threshold value $\bar{n}_{\text{pol,pro}}$. This counting is performed between proteins and membrane type 2 particles only (typically depicted as red in screenshots throughout this thesis); only steric (WCA) interactions are retained between proteins and membrane type 1 particles.

3.6.1 N -body potential

The contribution of the protein-membrane potential to the total system energy over all N_{prot} protein and N_{mem} membrane particles may be written

$$\begin{aligned}
\mathcal{U}_{\text{PM}} &= \epsilon \sum_i^{N_{\text{pro}}} A_{\text{pol}} \\
&= \epsilon \sum_i^{N_{\text{pro}}} \left(1 - \frac{n_{\text{pol,pro}}}{\bar{n}_{\text{pol,pro}}} \right) \\
&= \epsilon \sum_i^{N_{\text{pro}}} \left(1 - \frac{1}{\bar{n}_{\text{pol,pro}}} \sum_j^{N_{\text{mem}}} G_{ij}(r_{ij}) \cdot H_{\text{pol,mem}}(z_{\text{mem}}) \right)
\end{aligned}$$

Note that the equation above depends on z_{mem} , which is determined by the membrane particle orientation. This dependency helps to maintain that the protein is driven to be on the membrane surface only.

Letting $H_{\text{pol}} = 1 - H_{\text{eq}} = 1 - H$,

$$\mathcal{U}_{\text{PM}} = \epsilon \sum_i^{N_{\text{pro}}} \left(1 - \frac{1}{\bar{n}_{\text{pol,pro}}} \sum_j^{N_{\text{mem}}} G_{ij} \cdot (1 - H_{\text{mem}}) \right)$$

Taking the gradient to calculate the force between protein particle i and membrane particle j ,

$$\begin{aligned}
-\mathbf{f}_{ij} &= \nabla_{\mathbf{r}_{ij}} \mathcal{U}_{\text{PM}} = \epsilon \nabla_{\mathbf{r}_{ij}} \left(1 - \frac{1}{\bar{n}_{\text{pol,pro}}} \sum_j^{N_{\text{mem}}} G_{ij} (1 - H_{\text{mem}}) \right) \\
&= -\frac{\epsilon}{\bar{n}_{\text{pol,pro}}} \nabla_{\mathbf{r}_{ij}} (G_{ij} (1 - H_{\text{mem}})) \\
&= -\frac{\epsilon}{\bar{n}_{\text{pol,pro}}} \left((1 - H_{\text{mem}}) \nabla_{\mathbf{r}_{ij}} G_{ij} - (G_{ij} \nabla_{\mathbf{r}_{ij}} H_{\text{mem}}) \right) \\
&= -\frac{\epsilon}{\bar{n}_{\text{pol,pro}}} \left((1 - H_{\text{mem}}) \left(\frac{\partial G_{ij}}{\partial \mathbf{r}} \right) - \left(G_{ij} \left(\frac{\partial H_{\text{mem}}}{\partial z_{\text{mem}}} \right) \left(\frac{\partial z_{\text{mem}}}{\partial \mathbf{r}} \right) \right) \right)
\end{aligned}$$

The form of these forces is subtly different for the membrane particle and the protein particle, respectively. To see this, let

$$\begin{aligned}\mathbf{r} &= \mathbf{r}_{ij} = \mathbf{r}_{\text{pro}} - \mathbf{r}_{\text{mem}} \\ &= -\mathbf{r}_{ji}\end{aligned}$$

$$z_{\text{mem}} = \frac{\mathbf{r}_{ji} \cdot \hat{\mathbf{e}}_{\text{mem}}}{|r|}$$

$$\begin{aligned}\frac{\partial z_{\text{mem}}}{\partial \mathbf{r}_{\text{mem}}} &= \frac{\hat{\mathbf{e}}_{\text{mem}}}{|r|} - \frac{-\mathbf{r} \cdot \hat{\mathbf{e}}_{\text{mem}}}{|r|^2} \left(\frac{\mathbf{r}}{|r|} \right) \\ &= \frac{\hat{\mathbf{e}}_{\text{mem}}}{|r|} + \frac{\mathbf{r} \hat{z}_{\text{mem}}}{|r|^2}\end{aligned}$$

$$\begin{aligned}\frac{\partial z_{\text{mem}}}{\partial \mathbf{r}_{\text{pro}}} &= \frac{-\hat{\mathbf{e}}_{\text{mem}}}{|r|} - \frac{-\mathbf{r} \cdot \hat{\mathbf{e}}_{\text{mem}}}{|r|^2} \left(\frac{-\mathbf{r}}{|r|} \right) \\ &= -\frac{\hat{\mathbf{e}}_{\text{mem}}}{|r|} - \frac{\mathbf{r} \cdot \hat{z}_{\text{mem}}}{|r|^2}\end{aligned}$$

The above concerns the translational gradient of the potential. For the orientational gradient,

$$\begin{aligned}\nabla_{\hat{\mathbf{e}}} \mathcal{U}_{\text{PM}} &= -G \left(\frac{\partial H}{\partial z_{\text{mem}}} \right) \left(\frac{\partial z_{\text{mem}}}{\partial \hat{\mathbf{e}}} \right) + (1-H) \left(\frac{\partial G}{\partial \mathbf{r}} \right) \left(\frac{\partial \mathbf{r}}{\partial \hat{\mathbf{e}}} \right) \\ &= -G \left(\frac{\partial H}{\partial z_{\text{mem}}} \right) \left(\frac{\partial z_{\text{mem}}}{\partial \hat{\mathbf{e}}} \right)\end{aligned}$$

where

$$\frac{\partial z_{\text{mem}}}{\partial \hat{\mathbf{e}}_{\text{mem}}} = \frac{\mathbf{r}_{ji}}{|r|} = -\frac{\mathbf{r}_{ij}}{|r|}$$

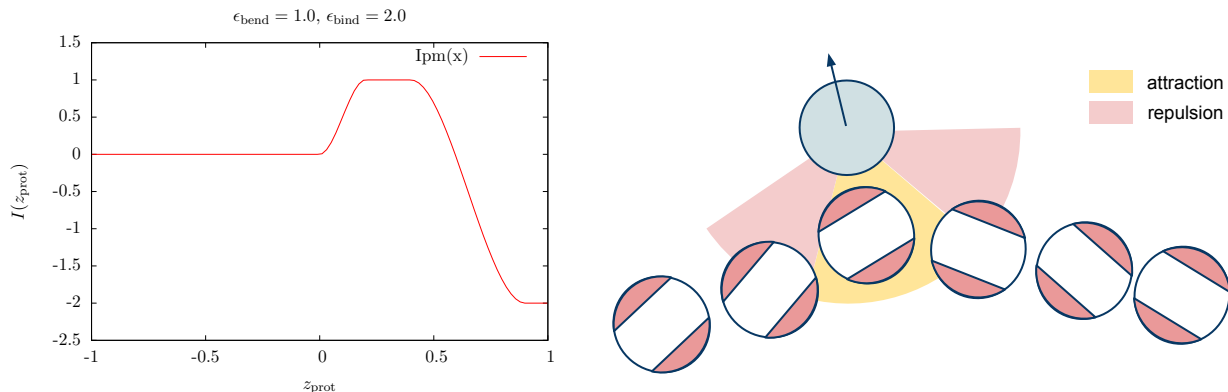


Figure 3.6: Adapting the protein-membrane potential to mimic hydrophobic insertion.

$$\frac{\partial z_{\text{mem}}}{\partial \hat{\mathbf{e}}_{\text{pro}}} = 0$$

where the final equation equals zero because the orientation of protein particles is unaffected by any part of the simulation. In other words, protein particles effectively have no orientation, however we work this out here for completeness and to symbolize that protein orientations are tracked in the simulation program.

3.6.2 Mimicking hydrophobic insertion

Though we have not tested this effect thoroughly in simulation, there has been much research that suggests the hydrophobic insertion mechanism of proteins and other inclusions (see section 1.3) is a significant driving force for membrane curvature [3]. This effect originates within the bilayer, resulting from crowding among lipids. Hydrophobic insertion has been studied both in continuum mechanics methods [26], which allow the stress caused by the insertion to be relaxed throughout the material by bending, and using atomistic simulation [85]. Our work indicates that steric effects within adhered protein layers may be more significant [75, 76], yet hydrophobic insertions may still play a functionally important cooperative role in curvature induction. This role could be studied by extending the model development described above. Though our membrane model does not resolve individual lipids, hydrophobic insertion could still be mimicked by incorporating an additional function I of the following form,

$$I(z_{\text{prot}}) = \begin{cases} 0 & z_{\text{prot}} < 0 \\ \epsilon_{\text{bend}} \left(1 - \frac{2}{a^3} (z_{\text{prot}} - a)^2 (z_{\text{prot}} + \frac{a}{2})\right) & 0 < z_{\text{prot}} < a \\ \epsilon_{\text{bend}} & a < z_{\text{prot}} < b \\ \epsilon_{\text{bind}} - \frac{2(\epsilon_{\text{bend}} - \epsilon_{\text{bind}})}{(b-c)^3} (z_{\text{prot}} - c)^2 (z_{\text{prot}} - \frac{3b-c}{2}) & b < z_{\text{prot}} < c \\ \epsilon_{\text{bind}} & c < z_{\text{prot}} < 1 \end{cases}$$

with a derivative

$$I'(z_{\text{prot}}) = \begin{cases} 0 & z_{\text{prot}} < 0 \\ \frac{-6\epsilon_{\text{bend}}}{a^3} z_{\text{prot}} (z_{\text{prot}} - a) & 0 < z_{\text{prot}} < a \\ 0 & a < z_{\text{prot}} < b \\ \frac{-6(\epsilon_{\text{bend}} - \epsilon_{\text{bind}})}{(b-c)^3} (z_{\text{prot}} - c)(z_{\text{prot}} - b) & b < z_{\text{prot}} < c \\ 0 & c < z_{\text{prot}} < 1 \end{cases}$$

where a, b, c are cutoff parameters switching between the pieces and $\epsilon_{\text{bend}}, \epsilon_{\text{bind}}$ are energy scales for the attractive and repulsive interactions (the heights of the higher and lower plateaus, respectively). Here, the separation vector \vec{r}_{ij} points from the membrane particle toward the protein, thus favorable binding happens when $z_{ij} = 1$ (the director and \vec{r}_{ij} point in the same direction). The protein-membrane potential could then be constructed as

$$\mathcal{U}_{\text{PM}}(r_{ij}, z_{\text{prot}}) = [G_{ij}(r_{ij})] [H_{\text{pol}}(z_{\text{mem}})] [I(z_{\text{prot}})]$$

though this potential is tunable in cutoff parameters and energy scales, it is pairwise instead of N -body. Other forms that retain the N -body character and neighbor counting scheme could be formulated, at perhaps greater complexity.

3.6.3 Parameter choices: pathologies and practical considerations

Our coarse-grained membrane-protein system has numerous independent, tunable parameters. The majority of these have no intrinsic physical meaning. Furthermore, there are many “good” choices for these parameters, leading to significant regions of parameter space that cannot be optimized and should (but are not guaranteed to) give quantitatively equivalent results for most physical properties of interest. However, some parameter values may be pathological (i.e., lead to unphysical and unwanted effects) for subtle reasons.

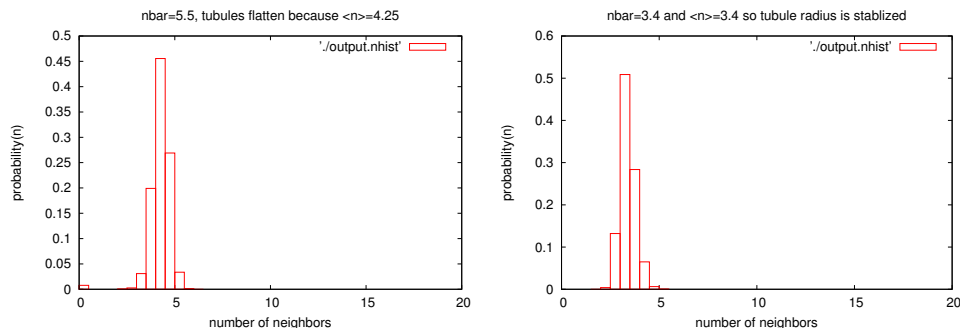


Figure 3.7: These histograms show distributions of n values for the protein-membrane potential for a tubule configuration. (left) Though typical values of n are ~ 4.5 , the value for $\bar{n} = 5.5$. Thus, this tubule is driven to increase its radius to increase n for particles in the protein layer. (right) Though there is no qualitative difference in this histogram, it shows that n for protein particles is easily above \bar{n} . Thus, this does not lead to unphysical effects on system curvature.

For example, the parameter \bar{n}_{prot} (the minimum number of polar membrane neighbors that a protein requires to minimize the protein-membrane potential) must not be set too low or else the protein may hover above the membrane surface. However, if it is set too high, this potential creates a driving force for the surface to wrap around a membrane particle in order to increase n_{prot} . This driving force may not be strong enough to produce this observation in simulation, however, and this unwanted effect might go unnoticed. However, if \bar{n}_{prot} is typically unreachable by proteins on a surface (see Figure 3.7) this parameter choice will bias against curvature via the mechanism we have sought to study. This bias occurs because production of curvature away from the protein requires n_{prot} to decrease. The parameter \bar{n}_{prot} should thus be carefully chosen such that it can still be reached by a typical protein even if the surface is substantially curved.

Other model parameters also have pathological regimes for subtle reasons. To test what parameters are suitable for our model we ran sets of simulations that scan across seemingly “good” regions of parameter space. Figure 3.8 shows an example of such a test, displaying 3 visible trends among these data. Analytic arguments (see Section 2.2) predicted that this system will relax to a radius somewhat greater than its starting radius of $R = 7.5\sigma$. However, results from the lower 2 lines are unphysical because \bar{n} is so low that proteins are permitted to partially penetrate the membrane while maintaining $n > \bar{n}$, increasing the membrane layer’s density and favoring increases in L_z instead of those in L_x and L_y that are required for the tubule radius to increase. The middle 4 lines are also unphysical because the membrane and protein layers both have crystallized and nested into each other (see Figure 3.9). This ordering occurs because the parameters of these simulations hold the proteins very close to the membrane particles, templating the protein layer and frustrating fluid movement across

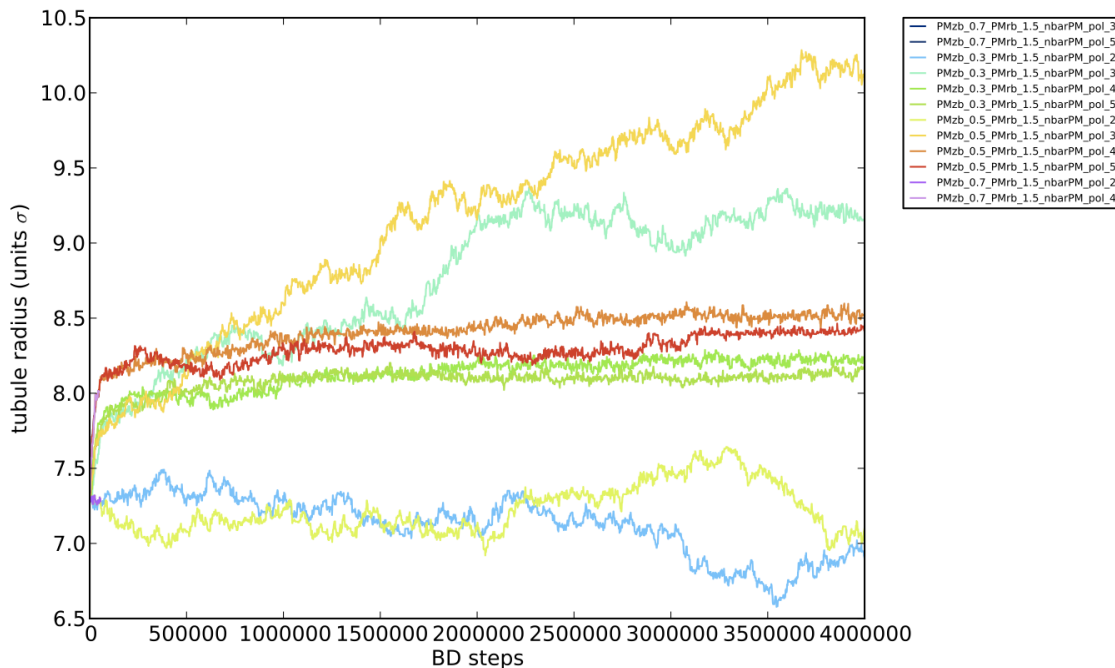


Figure 3.8: Different choices of parameters for the protein-membrane potential lead to different behavior. In these simulations, a box-spanning membrane tubule of radius $R = 7.5\sigma$ is allowed to relax to lower curvatures. Clusters of similar looking trajectory data might indicate problems with parameter choices.

the surface.

Finally, aside from avoiding the pathologies discussed above, the other consideration when choosing parameters is computational efficiency. Choosing r_a and r_b to be small, but not so small such that the aforementioned problems are encountered, reduces the amount of computation done during pairwise loops within the simulation algorithm (since fewer pairs will lie within these cutoffs). This aids in selection among parameter space that would otherwise feature much effective degeneracy.

In general, parameter selections for the research presented here were chosen because (i) both the protein layer and membrane layer particles appear to have fluid motion in visualized trajectories, (ii) proteins did not unphysically crystallize (as in Figure 3.9), (iii) proteins do not penetrate the membrane surface, (iv) in the data from Figures 3.8 and 3.10, tubule radii trajectories were among the most slowly-relaxing (i.e., trajectories with fast-increasing R suggest that the parameters choices resulted in $n < \bar{n}$, thus unphysically biasing against curvature), (v) and the lengthscale cutoff parameters r_a and r_b were small.

Model parameters typically needed to be modified according the properties of the system being simulated. Experience, as well as data seen in Figures 3.8 and 3.10, has shown that

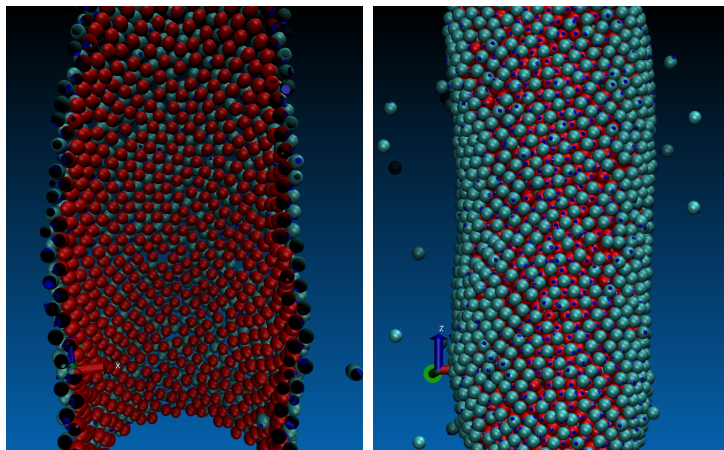


Figure 3.9: Unphysical crystallization occurs when lengthscale parameters of the protein-membrane potential are too small, driving protein particles to sit between membrane particles like eggs in an egg carton (as seen in the cross section image, left). Though pure systems of hard disks and hard spheres are widely known to crystallize beyond some critical packing fraction [86], the ordering in the protein layer seen above is an artifact which results using these parameters because the membrane is resolved as a discrete set of bilayer-spanning spheres. Though we anticipated that the protein layer would crystallize at high packing fractions using the “good” parameters discussed below, analogously to the pure hard disk system, this was not observed.

when $\sigma_{\text{prot}} = 2\sigma_{\text{mem}}$ good choices of parameters for the protein-membrane potential are $\{z_a = 0.2, z_b = 1.5, r_a = 1.2, r_b = 3.0, \bar{n} = 3\}$ and $\{z_a = 0.2, z_b = 1.5, r_a = 1.2, r_b = 3.5, \bar{n} = 4.5\}$, and the former set was used for data in Section 4 that is in preparation for publication. When $\sigma_{\text{prot}} = 1\sigma_{\text{mem}}$, good choices of parameters for the protein-membrane potential are $\{z_a = 0.2, z_b = 0.4, r_a = 1.2, r_b = 2.25, \bar{n} = 3.25\}$.

3.7 Computational analysis of model properties

3.7.1 Bending rigidity computation

The bending rigidity, which is specified as κ in the Helfrich free energy (eq. 1.1), is a fundamental material property of membranes. This property is typically measured in molecular simulation by fitting this free energy expression to height fluctuation statistics of a nearly flat membrane above the xy -plane (a parameterization is known in differential geometry as the Monge gauge [10]). To second order, this expression may be written

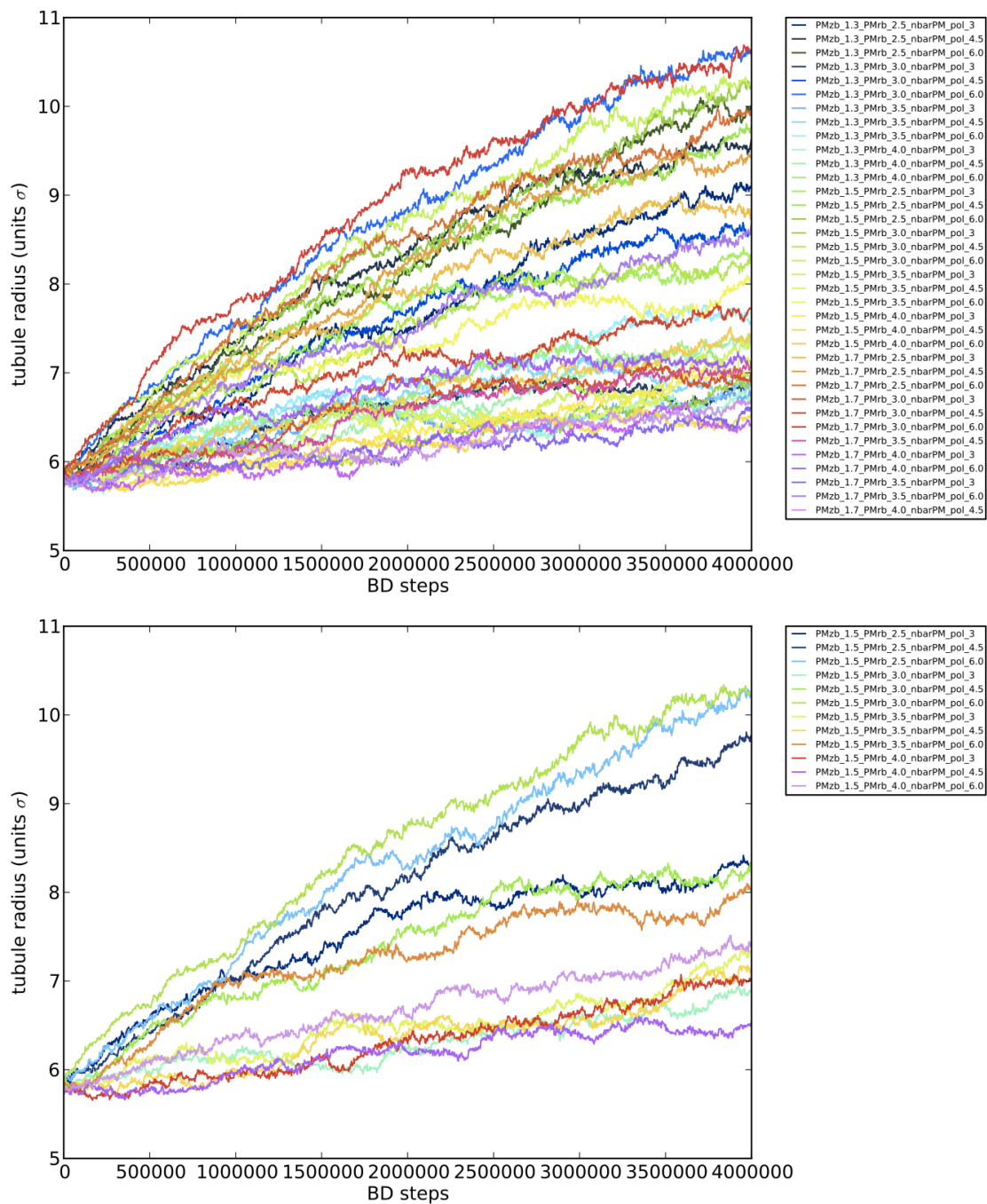


Figure 3.10: Parameter trace results for $\sigma_{\text{prot}} = 2\sigma_{\text{mem}}$. Good choices of parameters for the protein-membrane potential are $\{z_b = 1.5, r_b = 3.0, \bar{n} = 3\}$ or $\{z_b = 1.5, r_b = 3.5, \bar{n} = 4.5\}$.

$$F = \int dx \int dy \left\{ \frac{\kappa}{2} [\nabla^2 h(x, y)]^2 + \frac{\gamma}{2} [\nabla h(x, y)]^2 \right\} \quad (3.19)$$

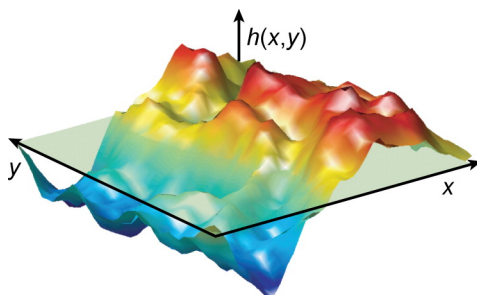
In Fourier space, equation 3.19 may be written

$$F = \frac{1}{2A_p} \sum_{\mathbf{q}} (\kappa \mathbf{q}^4 + \gamma \mathbf{q}^2) |\hat{h}_{\mathbf{q}}|^2 \quad (3.20)$$

where A_p is the projected area of the membrane onto the xy -plane and we have defined for forward and reverse Fourier transforms to be $\hat{h}_{\mathbf{q}} = \int_{A_p} d\mathbf{r} h(\mathbf{r}) e^{-i\mathbf{q}\cdot\mathbf{r}}$ and $h(\mathbf{r}) = \frac{1}{A_p} \sum_{\mathbf{q}} \hat{h}_{\mathbf{q}} e^{i\mathbf{q}\cdot\mathbf{r}}$, respectively, and where \mathbf{r} is a coordinate in the xy -plane. By applying the equipartition theorem [77], equation 3.20 tells us that the mean squared height fluctuations of each mode may be written as

$$\langle |\hat{h}_{\mathbf{q}}|^2 \rangle = \frac{k_B T A_p}{\kappa q^4 + \gamma q^2} \quad (3.21)$$

This equation may be used to calculate κ and γ by fitting data gathered from nearly-flat, fluctuating membrane simulations. To do this, uncorrelated samples of this surface are fit to an evenly-spaced grid in xy -plane, transformed via Fast Fourier transform (using, e.g., FFTW), and then plotted on a log-log scale as a function of q . For a successful membrane model, these data will fit the righthand side of equation 3.21 and κ may be extracted from the y -intercept of a linear fit (see Figure 3.12). This relationship breaks down in the high q (low-wavelength) regime because the fundamental approximation of this model – that the membrane is a continuum sheet – is no longer valid.




 Brown FLH. 2008.
Annu. Rev. Phys. Chem. 59:685–712.

Figure 3.11: A nearly membrane surface fluctuating above the xy -plane, characterized by the height function $h(x, y)$. This parameterization is sometimes known as the Monge gauge. (Adapted from Brown [87].)

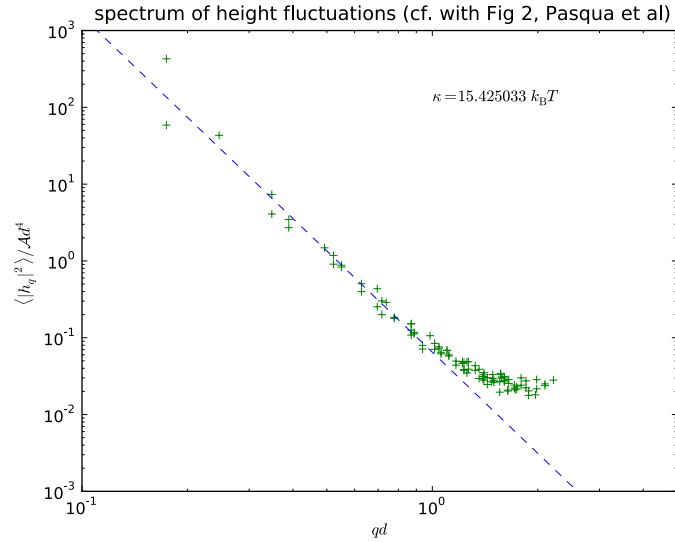


Figure 3.12: Fourier transformed height fluctuation statistics on a log-log scale. These data can be fit to equation 3.21 to extract the bending modulus (κ) and the surface tension (γ).

The bending rigidity may also be measured from molecular simulation using a virial equation of state [88]. This calculation is not available to some membrane models, such as the commonly-used triangulated mesh model [89, 90], because force equations cannot be derived from such potentials. However, for our meshless model this method provides a straightforward and generally faster way to calculate κ than the Fourier method described above.

The tensile force expression we use to extract κ from the virial expression was originally derived to calculate this quantity experimentally from membrane tubules [91]. In such experiments, a pipette or optical trap is used to pull a membrane tubule from a giant unilamellar vesicle. The relationship between R , κ , and the tensile force measured by this apparatus can be derived from the free energy (eq. 1.1) of a tubule as

$$\begin{aligned}
 f_z &= \left(\frac{\partial F}{\partial L_z} \right)_A = \left(\frac{\partial}{\partial L_z} \left[\frac{\kappa A}{2R^2} \right] \right)_A \\
 &= \left(\frac{\partial}{\partial R} \left[\frac{\kappa A}{2R^2} \right] \right)_A \left(\frac{\partial R}{\partial L_z} \right)_A = \left(-\frac{\kappa A}{R^3} \right) \left(-\frac{A}{2\pi L_z^2} \right) \\
 &= \frac{2\pi\kappa}{R}
 \end{aligned} \tag{3.22}$$

In simulations, this tensile force can be calculated from z -direction stress via $f_z = \sigma_{zz} L_x L_y$, where σ_{zz} is available from the virial equation [92],

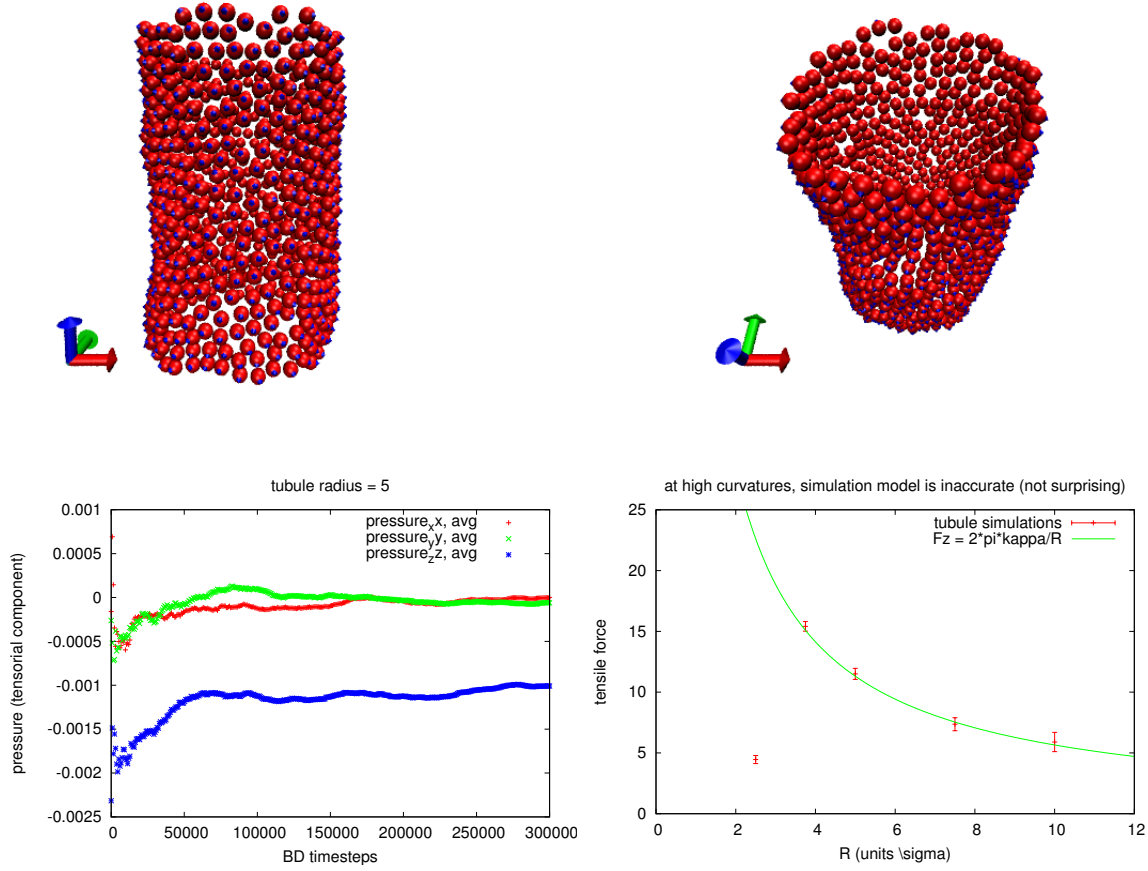


Figure 3.13: (top) Snapshots of a membrane tubule simulation used to calculate κ . Here, $\langle R \rangle = 7.5\sigma$, $L_z = 25\sigma$, and $N_{\text{mem}} = 803$. (bottom left) This shows running averages of σ_{zz} computed using equation 3.23. Stress in the x and y direction converges to 0, however, z -direction stress converges to a nonzero value. Confer with Figure 3 from [88]. (bottom right) tensile force calculations, here for a bare membrane, accurately correspond to κ over a variations of tubules radius. These data at $R = 2.5\sigma$ do not map to equation 3.22 because the tubule has ruptured. The tubule configuration cannot be sustained because the radius is approaching the natural coarse-graining length scale of the model.

$$\sigma_{zz} = \rho k_B T + \frac{1}{V} \left\langle \sum_{(i,j)} \mathbf{f}_z^{(i,j)} r_z^{(i,j)} \right\rangle \quad (3.23)$$

It is worth noting that this form is typically presented as valid for pairwise potentials [92]. Our membrane-membrane and membrane-protein potentials are fundamentally N -body, and

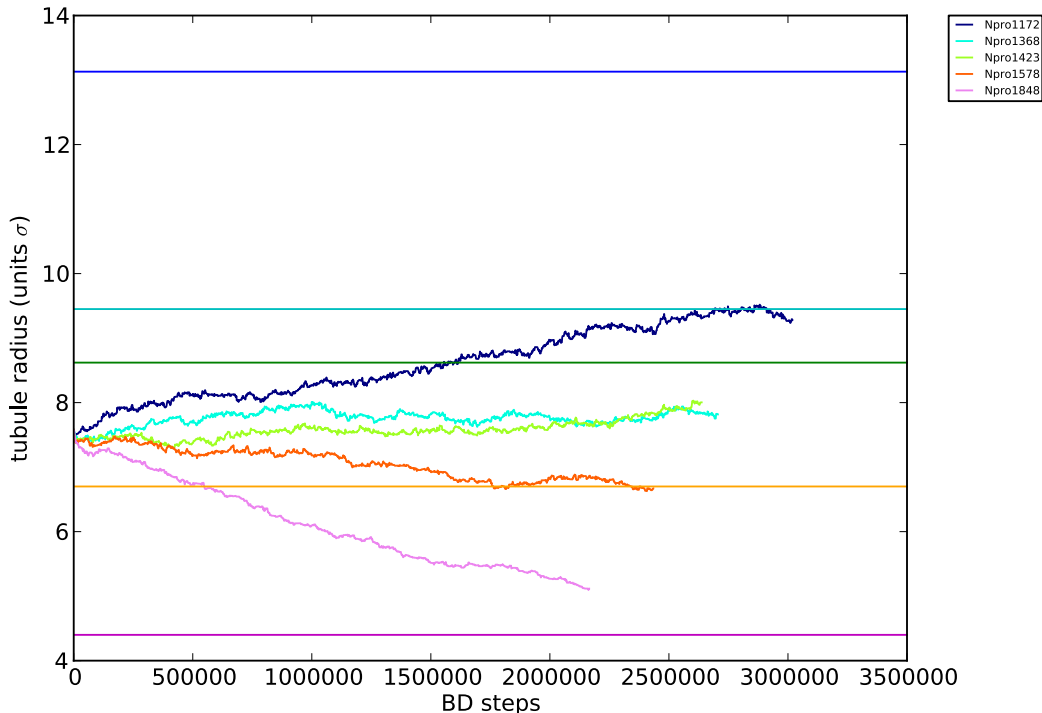


Figure 3.14: Tubule relaxation trajectories. These tests were intended to measure R_0 for various protein densities by letting the tubule radii relax, however this happened very slowly for reasons described in this section. The key of this plot gives N_{prot} for each simulation, and the corresponding colored straight lines are the R_0 values each of these simulations were predicted to relax to given the equation $R_0 = \kappa/pl$ (see section 2.2).

it is not immediately clear if equation 3.23 is valid and the previous force calculations (see section 3.4) can be straightforwardly applied. Though we do not show this here, it can be verified somewhat laboriously that 3.23 is usable for our model without modification.

3.7.2 Relaxation time of cylindrical morphologies

In our earliest work for this project, we supported the experimental observations of Stachowiak and coworkers by showing that the equilibrium radius $R_0 = \kappa/pl$ (see Section 2.2, [76]). To test this prediction, some of our first simulations studied box-spanning tubule configurations, letting the L_z dimension of the box (and thus the tubule radius) relax. Such tests effectively simulate a tensile force $f_z = 0$ ensemble, using box-scaling Monte Carlo moves described in section 3.8.1.

However, these proved to be extremely slow, computationally intensive simulations (see Figure 3.14). To understand why we observed slow relaxation in this coarse-grained degree

of freedom we looked at its relaxation properties using the overdamped Langevin equation, allowing us to understand its scaling with time (t). Note, in the analysis below we are looking at the simplest case, where $N_{\text{pro}} = 0$.

From equation 1.1, we have for a tubule with $c_0 = 0$,

$$F = A \left(\frac{\kappa}{2} \frac{1}{R^2} \kappa \right) + \gamma A$$

$$- \left(\frac{\partial F}{\partial R} \right)_A = \frac{A\kappa}{R^3}$$

thus we may write our overdamped Langevin equation

$$0 = \ddot{R}(t) = -\gamma \dot{R}(t) + \left(\frac{\partial F}{\partial R} \right)_A + \xi(t)$$

$$\gamma \dot{R}(t) = \frac{A\kappa}{R^3(t)} + \xi(t). \quad (3.24)$$

This equation is nonlinear due to the Gaussian noise term, $\xi(t)$. However, we can analyze the average t -scaling of this equation straightforwardly since doing this causes this noise term to vanish. The resulting differential equation once averaged is of the following form and may be solved analytically to give the t -scaling,

$$\dot{f}(t) = \frac{1}{f^3(t)}$$

$$f^3(t) \dot{f}(t) = 1$$

$$\frac{1}{4} \frac{d}{dt} f^4(t) = 1$$

$$\frac{d}{dt} f^4(t) = 4$$

$$f^4(t) = 4t + c$$

$$f(t) = (4t + c)^{1/4}$$

Since $R = R_0$ at $t = 0$, we have

$$\langle R(t) \rangle \sim (4t + (R_0)^4)^{1/4}$$

We used Euler integration to numerically simulate equation 3.24 and compare with our analytic scaling result for $\langle R(t) \rangle$. By setting a convenient choice of units (energy scale

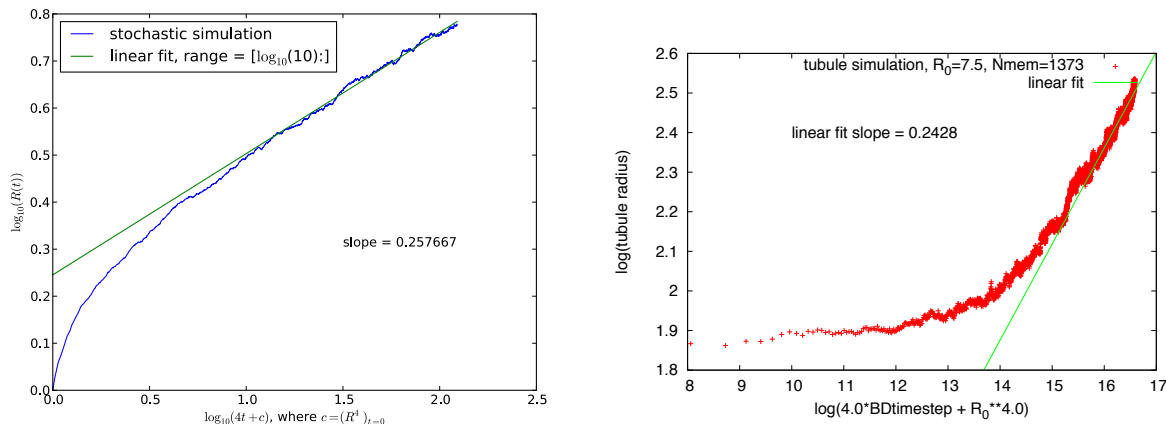


Figure 3.15: Both the numerically integrated Langevin representation and the molecular simulation approximately scale as $R \propto (t + c_0)^{\frac{1}{4}}$, where $c_0 = (R_0)^4$, for long timescale tubule radius relaxation dynamics. Early timescale dynamics are qualitatively different, however this is expected since the molecular simulation relaxes via particle position fluctuations and the other is approximated as and exact cylinder. (left) Euler-integrated numerical solution to our Langevin representation of R_0 relaxation dynamics. (right) Molecular simulation of R_0 relaxation dynamics.

$\epsilon = k_B T$, length scale $l = \sqrt{A}$, time scale $\tau = \gamma \frac{A}{k_B T}$ and reduced parameters ($\kappa^* = \frac{\kappa}{k_B T}$, $\gamma^* = 1$, $R^* = \frac{R}{\sqrt{A}}$) the previous equation (with the * implied) reduces to

$$\dot{R}(t) = \frac{\kappa}{R^3(t)} + \xi(t)$$

These results are plotted with molecular simulation data in Figure 3.15. Both show $R \sim (t + c_0)^{\frac{1}{4}}$, where $c_0 = (R_0)^4$, at long timescales.

3.8 Other features of the custom simulation program

3.8.1 Constant tension ensemble

Biological membranes, as well as those used in simplified experiments, are typically considered to exhibit zero or vanishing surface tension (γ). Thermodynamically, this property means that such membranes should feature significant fluctuations in area with substantial probability.

Since real biological membranes are not a continuum, however, practical implementation of a physically meaningful γ in computer simulations is non-trivial. In fact, this parameter is

perhaps best thought of as a chemical potential, since area fluctuations in a molecular material typically require fluctuations in molecule number. (Alternatively, such area fluctuations could come about due to fluctuations in area-per-lipid while keeping molecule number fixed. However such area-stretching comes at high energetic cost for typical membrane and even small increases can lead to rupture [48].)

A common way to implement a constant tension ensemble in molecular simulation is to allow for fluctuations in the projected area of the membrane, A_p , which is typically the xy -plane [93, 62]. In practice, after many particle position updates (via Monte Carlo or molecular dynamics algorithms) a value λ is chosen on some random interval. This variate is used to scale the box dimensions as $(\lambda L_x, \lambda L_y, \frac{1}{\lambda^2} L_z) = (L'_x, L'_y, L'_z)$. Particle positions are rescaled accordingly as well. After computing the new potential energy of the system, $\mathcal{U}(\mathbf{r}'^N; \lambda')$, the probability that a Monte Carlo move is accepted is

$$P_{\text{acc}}(\lambda \rightarrow \lambda') = \frac{\exp\{-\beta [\mathcal{U}(\mathbf{r}'^N; \lambda') - \gamma A(\lambda')]\}}{\exp\{-\beta [\mathcal{U}(\mathbf{r}^N; \lambda) - \gamma A(\lambda)]\}}$$

For all research presented in this thesis, simulations requiring a constant tension ensemble were done using $\gamma = 0 k_B T / \sigma^2$. In this case, the above expression simply reduces to

$$P_{\text{acc}}(\lambda \rightarrow \lambda') = \exp\{-\beta \Delta \mathcal{U}\}$$

where $\Delta \mathcal{U} = \mathcal{U}(\mathbf{r}'^N; \lambda') - \mathcal{U}(\mathbf{r}^N; \lambda)$.

3.9 Additional extensions

Here we describe additional aspects of the simulation program that have been developed and could be applied in future studies, including investigations of several systems presented in Chapter 1.

3.9.1 BAR proteins

Our earliest efforts aimed to study the shape transforming effects of collections of BAR (Bin-Amphiphysin-Rvs) family proteins [24]. These proteins are often associated with endocytosis, vesicle trafficking throughout the cell, and cell motility processes at the actin-membrane interface. The crystal structure of one protein in this family, *Drosophila* amphiphysin [94], suggested that these proteins typically generate curvature by binding to the membrane along the inner face of a crescent shape (see Figure 3.9.1). Since then many more members have of this family have been experimentally discovered, and intensive simulations analyzed detailed molecular representations of how these proteins couple to the underlying membrane [85, 95, 96, 97].

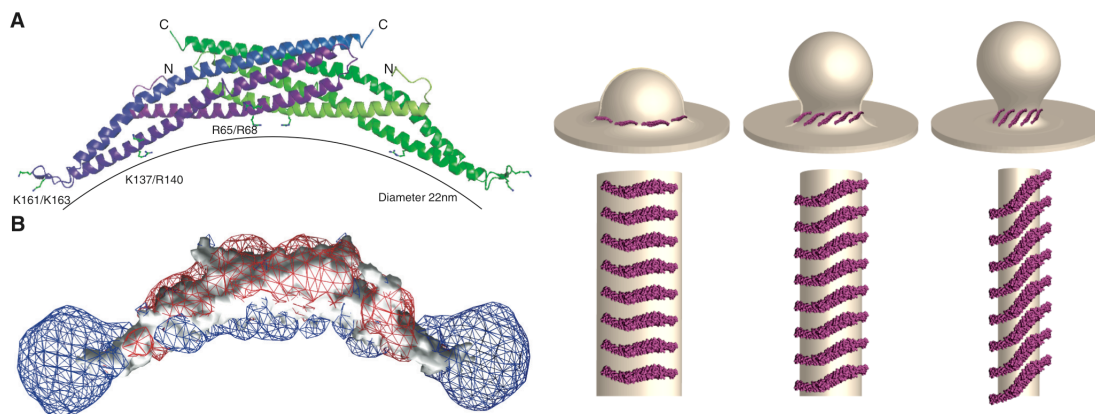


Figure 3.16: BAR family proteins and curvature generation (left) The protein structure of the the BAR domain of *Drosophila* amphiphysin [99]. The electrostatic equipotential surface in the lower image shows a high concentration of positive charge along the inner face, which is through to aid in binding and bending membranes rich in negative multivalent Phosphatidylinositol 4,5-bisphosphate (PIP₂) lipids. (right) This schematic shows how assembly features of FBAR proteins could allow these clusters to adapt to different curvatures and to possibly aid in vesicle neck constriction during endocytosis [100].

We sought to study the effects of large clusters of BAR proteins on the membrane surface in order to bring insight into how these assemblies might generate robust, diverse, and tunable membrane shapes. To achieve such large lengthscales I constructed a BAR protein model with orientational degrees of freedom consistent with the meshless membrane described throughout this chapter (see Figure 3.9.1). Bond length and bond angle constraints were handled by the SHAKE algorithm [98] and the protein-membrane potential was similar to the one described earlier in this chapter. After development of this model, however, we turned our attention to modeling the experimental of Stachowiak and coworkers [75, 76] and never returned to these tests.

3.9.2 Actin-membrane interactions

Another feature that was implemented in the simulation program but not studied was actin-membrane interactions. Actin filaments are important for motility, structural support, and other reasons in cells (as discussed in Section 1.5).

Actin filaments at large lengthscales are typically modeled using the “wormlike chain” (WLC) model for semiflexible polymers. In simulation, this model may be represented by a series of particles connected by segments (or “bonds”). Each unit segment vector \mathbf{t}_i corresponds to a tangent to the underlying curve of the semiflexible polymer being represented. This model may be defined as [11]

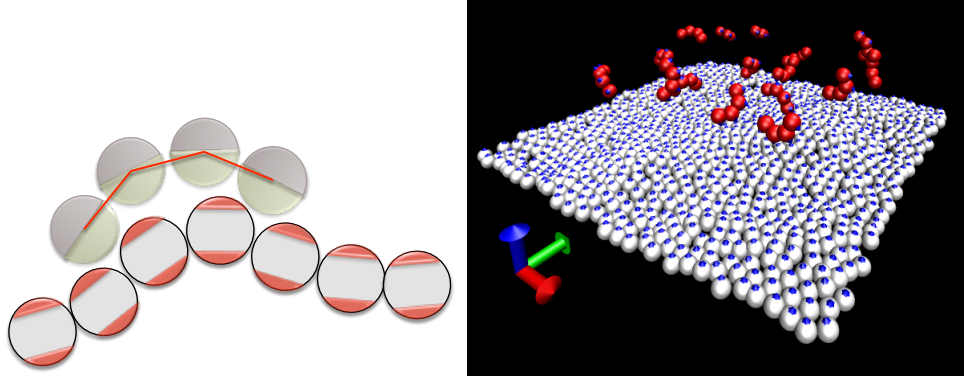


Figure 3.17: Implementing BAR family proteins in simulation using the membrane patch model of Pasqua *et al.* [66]. (left) This schematic shows how a simple model of a BAR family protein was implemented in the simulation program. The SHAKE algorithm was used to maintain distance constraints between neighboring particles and non-neighboring particles, modeling bonds and bond angles respectively. Variations in “curviness” could model various members of the BAR protein family, and the orientational protein-membrane potential was implemented as in section 3.6.2. (right) A snapshot of coarse-grained BAR molecules above a membrane surface.

$$U_{\text{WLC}} = \int_0^L \frac{l_p}{2} \left[\frac{\partial \mathbf{t}}{\partial s} \right]^2 ds$$

which, using a finite difference approximation, may be written

$$\begin{aligned} U_{\text{WLC}} &= \sum_{i=2}^{N_{\text{segments}}} \frac{l_p}{2} \left[\frac{\Delta \mathbf{t}}{\Delta s} \right]^2 \Delta s = \sum_{i=2}^{N_{\text{segments}}} \frac{l_p}{2s} |\mathbf{t}_i - \mathbf{t}_{i-1}|^2 \\ &= \sum_{i=2}^{N_{\text{segments}}} \frac{l_p}{2s} (\mathbf{t}_i^2 - 2\mathbf{t}_i \mathbf{t}_{i-1} + \mathbf{t}_{i-1}^2) \\ &= \sum_{i=2}^{N_{\text{segments}}} \frac{l_p}{2s} (1 - 2\cos\theta_{(i,i-1)} + 1) \\ &= \sum_{i=2}^{N_{\text{segments}}} \frac{l_p}{s} (1 - \cos\theta_{(i,i-1)}) \end{aligned}$$

where θ is the deviation of the angle between tangent vectors \mathbf{t}_i and \mathbf{t}_{i-1} , s is the segment length, and l_p is the persistence length (i.e., the stiffness of the polymer). By applying the law of cosines ($\theta = \arccos(\mathbf{u} \cdot \mathbf{v} / \|\mathbf{u}\| \|\mathbf{v}\|)$), corresponding force terms may be written

$$\begin{aligned}
\mathbf{F}_{ij} &= -\nabla_{\mathbf{r}_{ij}} \mathcal{U} = -\frac{\partial \mathcal{U}}{\partial \cos(\theta)} \cdot \frac{\partial \cos(\theta)}{\partial \mathbf{r}_{ij}} \\
&= -\left[-\frac{l_p}{s}\right] \cdot \left[\frac{1}{\|\mathbf{r}_{ij}\| \|\mathbf{r}_{jk}\|} \left(\mathbf{r}_{jk} - \frac{\mathbf{r}_{ij} \cdot \mathbf{r}_{jk}}{\|\mathbf{r}_{ij}\|^2} \mathbf{r}_{ij}\right)\right] \\
&= \left[\frac{l_p}{s}\right] \cdot \left[\frac{1}{\|\mathbf{r}_{ij}\| \|\mathbf{r}_{jk}\|} \left(\mathbf{r}_{jk} - \frac{\mathbf{r}_{ij} \cdot \mathbf{r}_{jk}}{\|\mathbf{r}_{ij}\|^2} \mathbf{r}_{ij}\right)\right]
\end{aligned}$$

This potential was implemented in the molecular simulation program, with filament particle diameters of 7 nm. However, as with the BAR proteins, this was put aside in order to study the results of Stachowiak and coworkers.

Chapter 4

Adhered proteins renormalize the material properties of membranes

Though a basic physical description of membranes has been well-established, there remains great interest in studying complex membranes relevant to biological systems. Here we analyze an extension to this basic description to include a common biological motif – a layer of proteins adhered to the membrane surface – and find that this system is equivalent to the basic description but with renormalized expressions for the bending rigidity, spontaneous curvature, and surface tension. All three expressions are functions of the packing fraction of adhered proteins, and at high packing fractions the system can become unstable. We examine these predictions in greater detail numerically using molecular simulation. Previously published experiments support our result for the renormalized bending rigidity and also observe our predicted curvature instability regime at high protein density. Our findings and others suggest that additional biological features may be physically understood in the context of such fundamental models, helping to characterize elementary features of processes like endocytosis and cell motility.

4.1 Introduction

Biological membranes are complex materials that must remodel, self-organize, and mechanically change in order to partake in myriad cellular processes. High-level observation by increasingly powerful optical techniques continue to reveal new roles that membranes play in motility [101], endocytosis [102], and other functions. Meanwhile, molecular-scale data regarding several proteins essential to these functions have identified structural characteristics that aid in organization and bending [3]. It nevertheless remains challenging to characterize how complex systems containing many interacting proteins mechanically couple to the underlying membrane at the mesoscale.

One common motif among many of biological processes is the clustering of proteins from the cytosol to the membrane surface in considerable density. Such systems have been

recently shown using reconstituted experimental systems to form highly curved tubule-like morphologies in a generic manner [75, 76]. As described in Chapter 2, we supported these results by showing theoretically that the area upon which adhered proteins sterically interact increases as curvature of the underlying membrane becomes larger in this system, producing an entropic driving force for curvature stabilization.

To more deeply characterize such systems, we extend here the basic physical description of membranes by generically modeling the effects of a layer of adhered proteins. This analysis results in a form equivalent to the original free energy equation with terms for effective parameters that are functions of the 2-dimensional pressure within this layer. To support these results, we use a hard disk fluid equation of state to express these parameters as functions of protein density and compare these predictions to numerical calculations attained using molecular simulation [61]. For at least one of these parameters, κ_{eff} , experimental data that support our result have been published previously [16].

Though these analytic and numerical results consider only steric (volume-excluding) interactions among proteins, we expect these expressions to apply to more generic protein-protein interactions as well. Furthermore, our results are aligned with other theoretical treatments of membrane systems that yield expressions for renormalized material parameters [19, 18, 17, 103, 104, 105, 106], many of which have also been supported experimentally [107, 108, 109]. Such developments suggest that novel extensions to the basic material descriptions of membranes will continue to provide a powerful way to understand the physics of increasingly complex and cell-like systems.

4.2 Analytical results

The standard free energy for a membrane of area A and a mean curvature H at each point on this surface may be written [13, 10],

$$F_{\text{mem}} = \int dA \left[\frac{\kappa}{2} (2H - c_0)^2 + \gamma \right]. \quad (4.1)$$

Curvature is geometrically defined as the inverse radius of a circle osculating the surface at a given point [10]. Our treatment of the protein layer (see Appendix A), which models adhered proteins as hard spheres interacting on a surface parallel to the membrane, yields effective expressions for the bending rigidity (κ), surface tension (γ), and spontaneous curvature (c_0) as a function of the 2-dimensional “pressure” of this protein layer,

$$\kappa_{\text{eff}} = \kappa - pl^2 \quad (4.2)$$

$$\gamma_{\text{eff}} = \gamma - p \quad (4.3)$$

$$c_{0,\text{eff}} = c_0 + \frac{pl}{\kappa} \quad (4.4)$$

where $p = -(\partial F_{\text{prot}}/A_{\text{prot}})_A$ is the pressure of the adhered protein layer and l is the distance between this layer and the underlying membrane. (The form for $c_0 = 1/R_{0,\text{eff}}$ is equivalent to our previously published result [76] but arrived at differently). This pressure is conceptually equivalent to that of a 2-dimensional fluid and increases monotonically with protein density.

As with bare membranes, the free energy of our composite system may be written in Fourier space as

$$F = \frac{1}{2A_p} \sum_{\mathbf{q}} \mathbf{q}^2 (\kappa_{\text{eff}} \mathbf{q}^2 + \gamma_{\text{eff}}) |\hat{h}_{\mathbf{q}}|^2 \quad (4.5)$$

This expression shows that this system will be unstable for any fluctuation mode \mathbf{q} such that $\kappa_{\text{eff}} \mathbf{q}^2 + \gamma_{\text{eff}} < 0$, or when $\mathbf{q} < \sqrt{(\gamma - p)/(\kappa - pl^2)}$. As we discuss later, this form predicts that long-wavelength fluctuations become unstable first as the density of adhered proteins increases, and eventually the system can be unstable at all modes. To test these and other predictions, we turned to molecular simulation of large scale coarse-grained membrane models.

4.3 Simulations of bending modulus and surface tension renormalization

We first intended to test these κ_{eff} and γ_{eff} predictions using the membrane patch model developed by Pasqua *et al.* and extended in Chapter 3. However, the calculations described below proved exceedingly difficult because at high densities the protein particles had a strong tendency to penetrate and rupture the membrane. Instead, group member Julian Weichsel incorporated a similar model for steric protein interactions into a widely used network model for fluctuating membranes [89, 90]. We include his results here for κ_{eff} and γ_{eff} calculations to more completely present support for the analytic predictions.

We estimated κ_{eff} and γ_{eff} by fitting height fluctuation statistics to the Fourier transform of equation 4.7 [10] (see Appendix B),

$$\langle |\hat{h}_q|^2 \rangle = \frac{k_B T \mathcal{A}}{\kappa q^4 + \gamma q^2}$$

where $\hat{h}_q = \int_A h(\mathbf{x}) \exp(i\mathbf{q} \cdot \mathbf{x}) d\mathbf{x}$ is the Fourier transform of the membrane height and \mathbf{q} is a 2-dimensional wavevector.

Using these simulations we observed the three instability regimes predicted by equation 4.5 above (see Figure 4.1). For low packing fractions of adhered proteins, all membrane fluctuation modes around the flat state are stable. At intermediate packing fractions, the large wavelength modes become unstable. Since the projected area is fixed and the area is

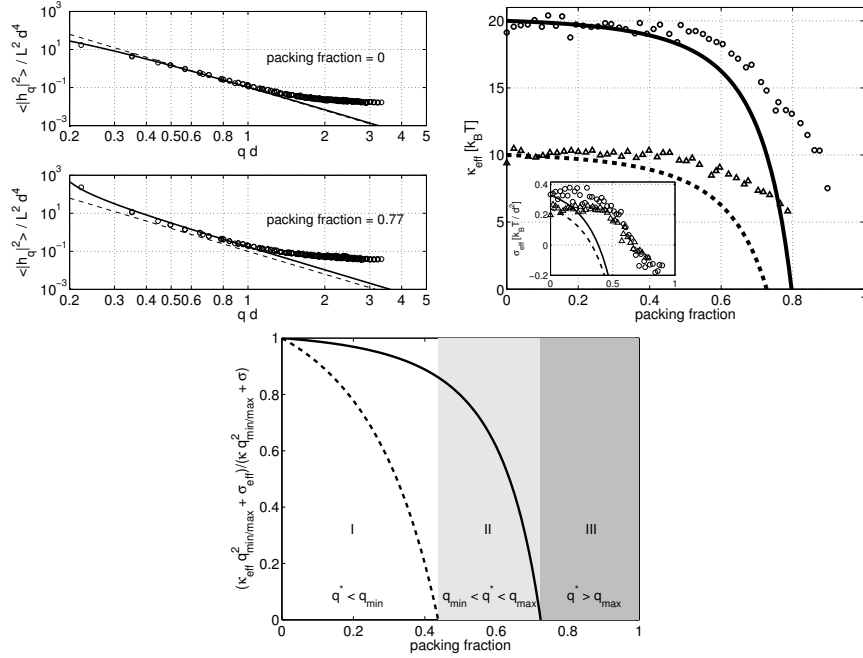


Figure 4.1: Renormalization of the bending modulus, κ_{eff} , and surface tension, γ_{eff} (data from simulations by Julian Weichsel). (top left) $\langle |h_q|^2 \rangle$ spectrum of the membrane height fluctuations around its flat state versus the corresponding mode q without adhered proteins (upper) and including adhered proteins (lower). The effective bending rigidity and surface tension are determined by fitting the small and long wavelength fluctuation regime respectively (solid line). The dashed line for comparison corresponds to a case without adhered proteins and vanishing surface tension. (top right) Renormalization of the bending rigidity and surface tension (inset) as functions of packing fraction of adhered proteins for $\kappa = 10 k_B T$ (triangles) and $20 k_B T$ (circles). Dashed and solid lines are the theoretical expectations. (bottom) Wavelength dependent instability regimes versus packing fraction of adhered proteins.

fluctuating but finite, these fluctuations are still constrained around the flat state and do not amplify indefinitely. However, as packing fraction increases more modes become unstable until the membrane fluctuations around the flat state become unstable at all wavelengths. At this point simulations typically display a small and highly curved membrane protrusion, as seen in Figure 4.4.

4.4 Simulations of spontaneous curvature renormalization

To measure the dependence of the effective spontaneous curvature, $c_{0,\text{eff}}$, on protein density, we used the “meshless” (i.e., non-triangulated) coarse grained membrane model [66]. This

model was recently developed in our group to study fluctuations and shape transformations of membranes at large scales while retaining properties such as hydrophobic effects, rupture tensions, fluidity, and self-assembly. Here, we combine this model with a consistent model for adhered proteins (described in Chapter 3) to straightforwardly calculate $c_{0,\text{eff}}$ from simulations of box-spanning membrane tubules of radius R held at a fixed length L_z (see Figure 4.4 & Appendix B). For a membrane with $c_0 = 0$ and $\gamma \approx 0$, the tensile force parallel to the axis of this tubule is

$$f_z = 2\pi\kappa \left(\frac{1}{R} - c_0 \right) = 2\pi\kappa \left(\frac{1}{R} - \frac{pl}{\kappa} \right). \quad (4.6)$$

The second equality above can be attained by inserting $c_{0,\text{eff}} = c_0 + pl/\kappa$ (eq. 4.4), which results from our treatment in Appendix A. This result may also be attained via $f_z = (\partial F_{\text{tot}}/\partial L_z)_A$, where $F_{\text{tot}} = F_{\text{mem}} + F_{\text{prot}}$ and $F_{\text{mem}} = \kappa A/2R^2$ is the Helfrich free energy of a membrane tubule.

Since our system consists of particles with a well-defined interaction potential, this force can be computed from the z -component of the virial stress tensor, σ_{zz} , along with simulation box dimensions L_x and L_y via $f_z = \sigma_{zz}L_xL_y$ [88]. Since R is fixed and κ may be calculated using equation 4.6 with no adhered proteins, these data together can be used to calculate $c_{0,\text{eff}}$ as a function of protein packing fraction, η . As shown in Figure 4.2, this calculation is in good agreement with the curve calculated using the Carnahan-Starling equation for hard disk fluids, with a somewhat more modest response. This result is consistent with our calculations for κ_{eff} and γ_{eff} .

4.5 Discussion

Here, we derived and showed numerically how clusters of adhered proteins on membranes can be physically understood in the context of the basic physics of soft materials. As mentioned before, our bending modulus renormalization result is supported experimentally by previously published research [16] (see Appendix C). In this work, Settles *et al.* used an optical trap to extend a membrane tube from a giant unilamellar vesicle and related the tensile force to protein concentration using an expression similar to equation 4.6. In fact, these authors interpret their data using famous result for κ_{eff} that is similar to our own [17]. However, their form posits a phenomenological linear coupling between composition and curvature instead of modeling the system based on more physical grounds.

In a similar spirit to our work here, another recent study [110] used coarse-grained molecular simulation to test established theoretical predictions about how generalized polymers anchored to membranes renormalize material parameters [103, 104]. Both the theoretical and computational studies showed that higher densities of these polymers increase $c_{0,\text{eff}}$. However, in contrast to our findings, anchored polymers were shown to effectively stiffen, rather

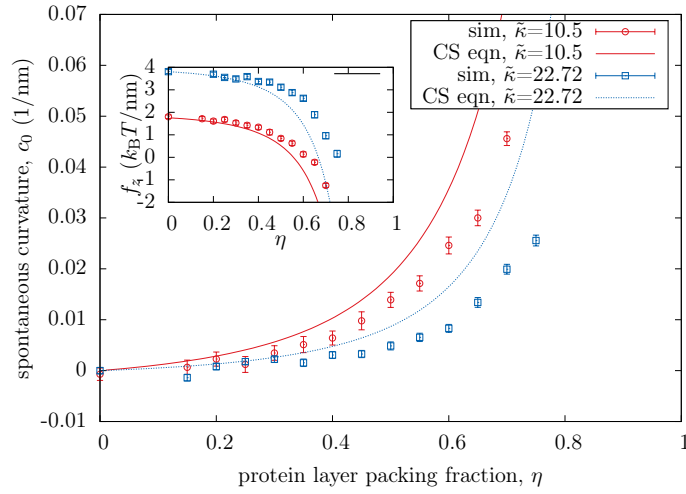


Figure 4.2: Renormalization of spontaneous curvature, $R_{0,\text{eff}}$. In the key, $\tilde{\kappa} = \kappa/k_B T$ is a reduced bending modulus, “sim” corresponds to molecular simulation data, and “CS eqn” plots equation 4.4 using the $2d$ Carnhan-Starling equation for pressure [79] and $l = (d_{\text{prot}} + d_{\text{mem}})/2 = 7.5\text{nm}$. (inset) raw data of tensile force computed as $f_z = \sigma_{zz}L_xL_y$ as a function of packing fraction of proteins. (main) Both the tensile force data and analytical curve are plotted via equation 4.6.

than soften, κ_{eff} . This disagreement suggests intriguing fundamental differences between these two simplified models – hard disks on a manifold and generalized anchored homopolymers – regarding how material properties emerge from steric interactions. Moreover, further study could bring insight to the effects of membrane-adhered proteins which may be partially disordered and are not well-approximated by either of these extremes.

Though we have modeled protein-protein interactions here using only volume-excluding steric considerations, biological macromolecules typically interact in a more complex manner. Such interactions can be experimentally measured for isotropic solutions of proteins using small angle scattering techniques [111], and these data could bring additional physical detail to further modeling studies. Collections of proteins may also cross-link or self assemble into heterogeneous and sometimes curved structures, such as clathrin coated pits [102]. Though our work and others’ suggest how fluctuations can entropically stabilize such structures, more complex models could elucidate how the more specialized proteins mechanically couple to the membrane to elicit specific biological processes.

4.6 Appendix A: Deriving κ_{eff} , γ_{eff} , and $c_{0,\text{eff}}$

Here, we derive expressions for the renormalized material parameters as functions of adhered protein density. (eqs. 4.2, 4.3, 4.4). The underlying membrane is described using the Helfrich

Hamiltonian (eq. 4.1) in the often-studied approximate form for a fluctuating surface above the xy -plane,

$$\begin{aligned} F_{\text{mem}} &= \int dx \int dy \left\{ \frac{\kappa}{2} [\nabla^2 h(x, y) - c_0]^2 + \frac{\gamma}{2} [\nabla h(x, y)]^2 \right\} \\ &= \int dx \int dy \left\{ \frac{\kappa}{2} H^2 - \kappa c_0 H + \frac{\gamma}{2} [\nabla h(x, y)]^2 \right\} \\ &\quad + \text{const.} \end{aligned} \tag{4.7}$$

where $H \approx \nabla^2 h(x, y)$ is the mean curvature in the Monge gauge [10] for a membrane with small but nonzero height fluctuations. Here and below, the symbol ‘ \approx ’ signifies either a Taylor expansion to second order in membrane curvature or a finite difference approximation.

To determine how the area of the protein layer depends on the curvature of the underlying membrane, consider this membrane surface to be parameterized by a square grid in the xy -plane with small spacing δ . The protein layer may be considered to be a parallel surface defined by a set of points $\{l\hat{n}_{(i,j)}\}$, where $\hat{n}_{(i,j)}$ is a unit normal vector to the membrane surface at the (i, j) th grid point and l is the height of the protein layer above the membrane. The area of the protein layer is the sum of the areas of each rectangular patch defined by these points.

Consider one surface patch that has corners at P_1 , P_2 , and P_3 . The area of this patch is equal to $|\mathbf{r}_{12} \times \mathbf{r}_{13}|$, where \mathbf{r}_{mn} is a vector pointing from P_m to P_n . The vector \mathbf{r}_{12} may be expressed as

$$\begin{aligned} \mathbf{r}_{12} &= P_1 - P_2 \\ &= \delta \hat{x} + \hat{z}[h(x + \delta, y) - h(x, y)] + l[\hat{n}(x + \delta, y) - \hat{n}(x, y)] \\ &\approx \delta \hat{x} + \hat{z}[\delta h_x] + l[\hat{n}(x + \delta, y) - \hat{n}(x, y)] \end{aligned} \tag{4.8}$$

The normal vector is defined as

$$\hat{n}(x, y) = \frac{\hat{z} - \nabla h(x, y)}{\sqrt{1 + |\nabla h(x, y)|^2}} \approx \hat{z} - \nabla h(x, y)$$

where

$$\begin{aligned} \nabla h(x + \delta, y) &= \hat{x}h_x(x + \delta, y) + \hat{y}h_y(x + \delta, y) \\ &\approx \nabla h(x, y) + \hat{x}\delta h_{xx}(x, y) + \hat{y}\delta h_{xy}(x, y). \end{aligned}$$

Thus the difference between normal vectors in equation 4.8 may be expressed as

$$\hat{n}(x + \delta, y) - \hat{n}(x, y) = -\hat{x}\delta h_{xx} - \hat{y}\delta h_{xy}$$

Using the following expressions

$$\begin{aligned}\frac{\mathbf{r}_{12}}{\delta} &\approx \hat{x}(1 - lh_{xx}) + \hat{y}(-lh_{xy}) + \hat{z}(h_x) \\ \frac{\mathbf{r}_{13}}{\delta} &\approx \hat{x}(-lh_{xy}) + \hat{y}(1 - lh_{yy}) + \hat{z}(h_y)\end{aligned}$$

The patch area can be expressed as

$$\begin{aligned}|\mathbf{r}_{12} \times \mathbf{r}_{13}| &= \delta^2 \sqrt{|\nabla h(x, y)|^2 + (1 - lH + l^2K)^2} \\ &\approx \delta^2 \left(1 + \frac{1}{2}|\nabla h(x, y)|^2 - lH + l^2K + \frac{1}{2}l^2H^2 \right)\end{aligned}$$

where $H = \nabla^2 h(x, y)$ is the mean curvature and $K = h_{xx}h_{yy} - h_{xy}^2$ is the Gaussian curvature (expressed using the notation $h_x = \partial h / \partial x$).

Summing over all patches (i, j) ,

$$\begin{aligned}A_{\text{prot}} &= \sum_{(i,j)} \delta^2 \left(1 + \frac{1}{2}|\nabla h(x_i, y_i)|^2 - lH_{(i,j)} + l^2K_{(i,j)} + \frac{1}{2}l^2H_{(i,j)}^2 \right) \\ &= A_{\text{mem}} + \int dx \int dy \left(\frac{1}{2}|\nabla h(x, y)|^2 - lH + l^2K + \frac{1}{2}l^2H^2 \right)\end{aligned}\quad (4.9)$$

For a surface of fixed topology, the Gauss-Bonnet theorem shows that $\int dx \int dy K$ will integrate to the same value for any configuration. Thus, we can write the free energy of the protein layer as a function of curvature as

$$\begin{aligned}F_{\text{prot}} &= \left(\frac{\partial F_{\text{prot}}}{\partial A} \right) \Delta A \\ &= (-p) (A_{\text{prot}} - A_{\text{mem}}) \\ &= \int dx \int dy \left(-\frac{pl^2}{2}H^2 + plH - \frac{p}{2}|\nabla h|^2 \right)\end{aligned}$$

The total free energy of the composite system is thus

$$\begin{aligned}F &= F_{\text{mem}} + F_{\text{prot}} \\ &= \int dx \int dy \left(\frac{\kappa}{2}H^2 - \kappa c_0 H + \frac{\gamma}{2}[\nabla h(x, y)]^2 \right) + \\ &\quad \int dx \int dy \left(-\frac{pl^2}{2}H^2 + plH - \frac{p}{2}|\nabla h(x, y)|^2 \right) \\ &= \int dx \int dy \left(\frac{\kappa - pl^2}{2}H^2 - (\kappa c_0 - pl)H - \frac{\gamma - p}{2}|\nabla h(x, y)|^2 \right)\end{aligned}$$

This result is of the same form as equation 4.7 but with renormalized parameters given by equations 4.2, 4.3, and 4.4).

4.7 Appendix B: Simulation Details

Meshless membrane model with proteins. To calculate $c_{0,\text{eff}}$, we used a meshless membrane model designed by Pasqua *et al.* [66]. This potential was modified to include slowly-varying functional forms so that force functions varied continuously with their dependent variables, as described in Chapter 3. This allowed us to simulate the model using Brownian Dynamics in the NVT ensemble [84] and to compute f_z using a virial expression (eq. 4.6). We verified that this modification reproduced all properties of the model in its original form.

We used the following values for the protein-membrane potential: $\bar{n} = 3$, $z_a = 0.2$, $z_b = 1.5$, $r_a = 1.2$, $z_b = 3$, $\epsilon = 25 k_B T$, $d_{\text{mem}} = 5$ nm, and $d_{\text{prot}} = 10$ nm. For the membrane-membrane potential we used the same parameters as those studied in the original paper and selected z_a in order to simulate the membrane rigidities $\kappa = 10.5 k_B T$ and $\kappa = 22.72 k_B T$. Protein-protein interactions were modeled as WCA spheres [83] to retain only repulsive, volume-excluding interactions.

4.8 Appendix C: Experimental measurement of κ_{eff} softening

After deriving our result above for renormalized material parameters, we found good experimental support for our κ_{eff} prediction in previous research. In particular, Settles *et al.* [16] used a membrane tether apparatus to measure the bending rigidity of tubules while varying the amount of Sar1 adhered to the surface (see Figure 4.5). Sar1 is a vesicle trafficking protein that has been shown previously to associate with curved membranes. This was also among the collection of proteins experimentally shown by Stachowiak *et al.* [76] to bend membranes via the protein-protein crowding mechanism (which was discussed in section 2 and inspired the work in this thesis).

Settles *et al.* used an optical trap to pull a tether from a giant unilamellar vesicle and measured κ_{eff} via the tensile force using an equation similar to equation 3.22. As they increased the concentration of Sar1 in solution they observed κ_{eff} to lower until the system reached a point of instability (i.e., the bending rigidity appear to become negative and the system lowered its free energy by becoming increasingly curved).

To understand this softening, these researchers applied a popular result of Leibler [17] to derive what they thought was an effective bending rigidity,

$$\begin{aligned} \frac{f_z R}{2\pi} &= \kappa_{\text{eff}}(R) \\ &= \kappa - \Lambda \phi R \end{aligned}$$

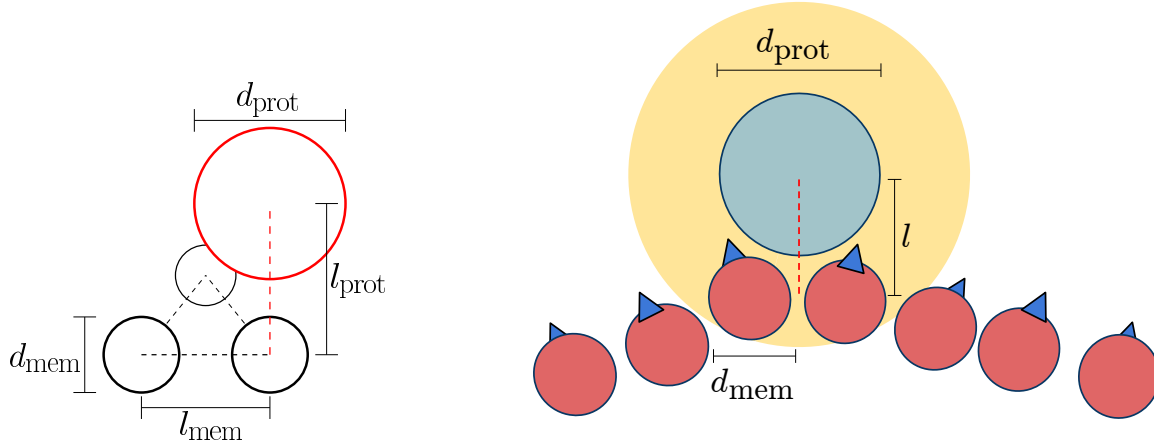


Figure 4.3: Coarse grained models. Here d are particle diameters and l is the height of the protein layer. (left) Triangulated mesh membrane model [89, 90], extended to include an adhered protein model. (right) The meshless membrane model we used was developed by Pasqua *et al.* [66] to study membrane height fluctuations and shape transformations at large lengthscales. This N -body potential allows fluid motion of particles within the surface, and the blue triangles represent each particle’s orientation vector. The protein-membrane potential was designed for this study to diffuse fluidly on the membrane surface. The protein-protein potential includes only volume excluding interactions. The diameter of each particle representing a membrane patch (and, thus, also the membrane thickness) is $d_{\text{mem}} = 5$ nm, the diameter of protein particles are $d_{\text{prot}} = 10$ nm. The protein layer height $l = (d_{\text{mem}} + d_{\text{prot}})/2 = 7.5$ nm was used for the analytical curve in Figure 4.2 and was verified numerically.

where ϕ is a molar concentration of membrane inclusions and Λ is a phenomenological parameter that linearly couples to ϕ in a form for the curvature free energy. However, κ_{eff} here is dependent on a term that linearly couples to R , which is more like a spontaneous curvature. Rearranging the above equation,

$$f_z = 2\pi\kappa \left(\frac{1}{R} - \frac{\Lambda\phi}{\kappa} \right)$$

This result is similar to our own equation 4.6 with pl^2 replaced by a phenomenological linear coupling. It was originally derived to understand curvature instabilities in red blood cells similar to those seen by Settles *et al.*. The molecules that induced this instability were suggested to generate curvature by some hydrophobic insertion mechanism like the one discussed in section 1.3. However, our own expression for the effective bending rigidity (4.2) is of a similar form and has more physical meaning. Furthermore, the characteristics of Sar1 suggest that a hydrophobic insertion mechanism is unlikely to be significant (as discussed by Stachowiak *et al.* [76]). The forms we derived for other material parameters also suggest

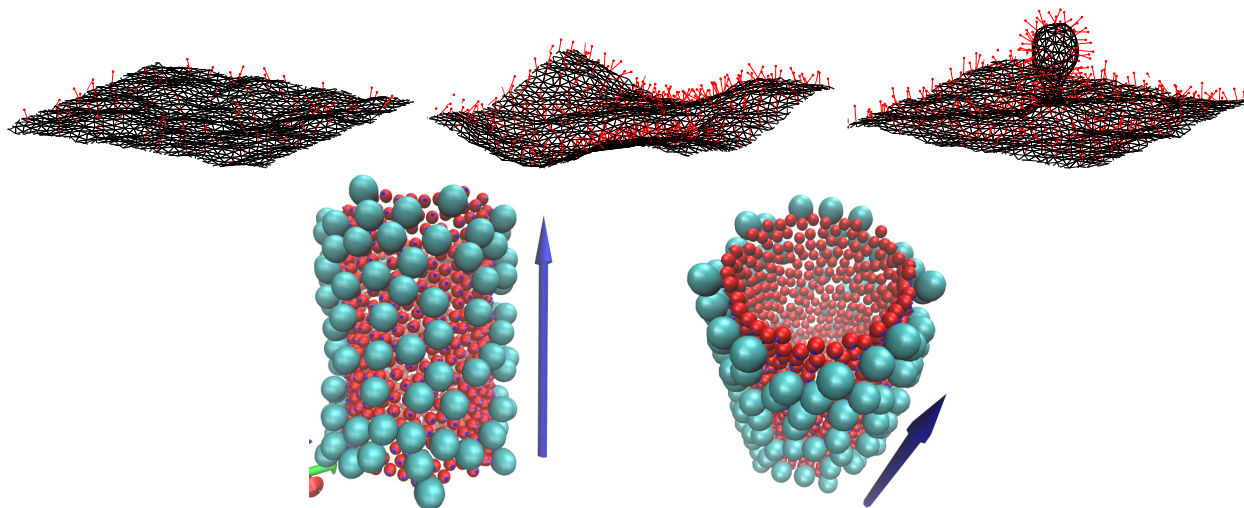


Figure 4.4: Molecular simulation snapshots. (top) These 3 screenshots correspond to the 3 regimes in Figure 4.1 – when no mode is unstable, when large wavelength modes are unstable, and when all modes are unstable and a membrane bud forms. (bottom) The tensile force was computed in the z -direction (blue arrow) using $f_{zz} = \sigma_{zz}L_xL_y$ and then related to c_0 using equation 4.6. Here, $\langle R \rangle = 37.5$ nm, $L_z = 125$ nm, $N_{\text{mem}} = 803$, and $N_{\text{prot}} = 146$.

that there are additional physical effects beyond κ_{eff} softening that characterized the system they studied, further conveying the rich physics that these systems display.

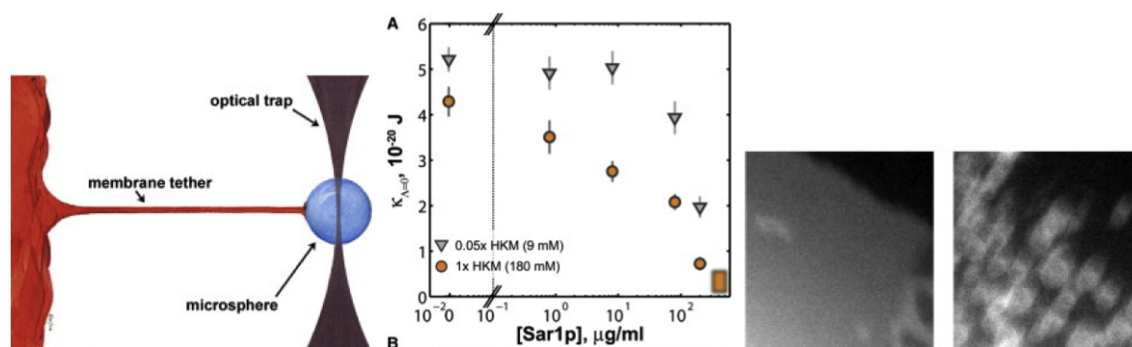


Figure 4.5: The results of Settles *et al.* [16] support our prediction that κ_{eff} softens as protein density increases. (left) This illustration shows the optical trap from which researchers extended membrane tethers and measured κ_{eff} from average values of tensile force. (middle) This plot shows that as protein density in solution (assumed to correlate with bound protein density) increases, κ_{eff} decreases until the system becomes unstable. (right) An image of the curvature instability seen when κ_{eff} would be predicted by the trend to become negative.

Chapter 5

Conclusions & Future Work

The work presented in this manuscript provides a basic physical understanding for a recently discovered mechanism for membrane curvature generation by adhered proteins. Furthermore, this research also exemplifies how two simple models that have been analyzed for decades – fluctuating membranes and hard sphere fluids – can produce surprising and meaningful physical results when studied as a composite system.

We have made many simplifying assumptions in order to elucidate the basic physics of our system, and further investigation of more specified systems could provide interesting findings. For example, incorporating biologically inspired protein-protein interactions such as attractions, repulsions, patchy potentials, or softness could yield surprising examples of self assembled structures. Remarkable self-organization is a hallmark of cellular life, and physical characterizations of such processes could aid in technological applications of nanoscale assembly.

We have also simplified our study by letting a single membrane particle, which represents a 25nm^2 patch of bilayer, be characterized by a single fixed lipid composition. Though our molecular simulation model is indeed highly coarse-grained, it is still amenable to incorporation of a fluctuating compositional degree of freedom for each particle. This feature might allow for more realistic simulations of how compositional fluctuations of important intra-membrane molecules, like PIP_2 , couple to both adhered protein concentrations and curvature stabilization.

With additions such as those discussed above and in Section 3.9, two promising application areas of our simulation tools would be the systems highlighted in Chapter 1 – aspects of clathrin-mediated endocytosis (CME) and filopodium formation. Both are appealing because they have been thoroughly studied in reconstituted systems and thus minimal sets of components have been largely identified [112, 57]. This information has already allowed for some theoretical studies of aspects of CME [113, 114, 115], yet there are many open questions about how coupled fluctuations of membranes and protein clusters lead to robust clathrin cage assembly. Reduced physical models have also been used to study the mechanical properties of filopodia by our research group [49, 116] and others [50], however little published work exists about the emergence of filopodia from coupled actin and membrane fluctuations. In

both of CME and filopodium formation, as well as many other processes, BAR proteins have been implicated as playing important roles in curvature generation and stabilization. These effects could be studied in our coarse-grained simulations using the model discussed earlier. Though all these possibilities lead to a very large design space for molecular simulation studies, data from biology could help direct these tests. Such considerations could then lead to large scale studies of cell-like organization processes at an optimal level of coarse-graining.

References

- [1] Yoko Shibata et al. “Mechanisms shaping the membranes of cellular organelles.” In: *Annual review of cell and developmental biology* 25 (Jan. 2009), pp. 329–54.
- [2] Bruno Antony. “Mechanisms of membrane curvature sensing.” en. In: *Annual Review of Biochemistry* 80 (June 2011), pp. 101–23.
- [3] Tobias Baumgart et al. “Thermodynamics and Mechanics of Membrane Curvature Generation and Sensing by Proteins and Lipids.” In: *Annual Review of Physical Chemistry* 62.1 (Apr. 2010).
- [4] Nikos S Hatzakis et al. “How curved membranes recruit amphipathic helices and protein anchoring motifs”. In: *Nature Chemical Biology* 5.11 (Sept. 2009), pp. 835–841.
- [5] K L Madsen et al. “BAR domains, amphipathic helices and membrane-anchored proteins use the same mechanism to sense membrane curvature.” In: *FEBS letters* 584.9 (May 2010), pp. 1848–55.
- [6] R M Hochmuth et al. “Extensional flow of erythrocyte membrane from cell body to elastic tether. II. Experiment.” In: *Biophysical Journal* 39.1 (July 1982), pp. 83–9.
- [7] A Tian and T Baumgart. “Sorting of lipids and proteins in membrane curvature gradients.” In: *Biophysical Journal* 96.7 (Apr. 2009), pp. 2676–88.
- [8] Aurélien Roux et al. “Role of curvature and phase transition in lipid sorting and fission of membrane tubules.” In: *The EMBO journal* 24.8 (Apr. 2005), pp. 1537–45.
- [9] Benoît Sorre et al. “Nature of curvature coupling of amphiphysin with membranes depends on its bound density.” In: *Proceedings of the National Academy of Sciences of the United States of America* 109.1 (Jan. 2012), pp. 173–8.
- [10] Samuel A. Safran. *Statistical Thermodynamics Of Surfaces, Interfaces, And Membranes (Frontiers in Physics)*. Westview Press, Jan. 2003.
- [11] Randall D. Kamien. “The geometry of soft materials: a primer”. In: *Reviews of Modern Physics* 74.4 (2002), pp. 953–971.
- [12] P B Canham. “The minimum energy of bending as a possible explanation of the biconcave shape of the human red blood cell.” In: *Journal of theoretical biology* 26.1 (Jan. 1970), pp. 61–81.

- [13] W Helfrich. “Elastic properties of lipid bilayers: theory and possible experiments.” In: *Zeitschrift für Naturforschung. Teil C: Biochemie, Biophysik, Biologie, Virologie* 28.11 (1973), pp. 693–703.
- [14] Derek Marsh. “Elastic curvature constants of lipid monolayers and bilayers”. In: *Chemistry and Physics of Lipids* 144.2 (Nov. 2006), pp. 146–159.
- [15] Jianjun Pan, Stephanie Tristram Nagle, and John F. Nagle. “Effect of cholesterol on structural and mechanical properties of membranes depends on lipid chain saturation”. In: *Physical Review E (Statistical, Nonlinear, and Soft Matter Physics)* 80.2 (2009).
- [16] Edward I. Settles et al. “The Vesicle Trafficking Protein Sar1 Lowers Lipid Membrane Rigidity”. In: *Biophysical Journal* 99.5 (Sept. 2010), pp. 1539–1545.
- [17] S. Leibler. “Curvature instability in membranes”. In: *Journal de Physique* 47.3 (1986), pp. 507–516.
- [18] L. Peliti and S. Leibler. “Effects of Thermal Fluctuations on Systems with Small Surface Tension”. In: *Physical Review Letters* 54.15 (Apr. 1985), pp. 1690–1693.
- [19] W. Helfrich. “Effect of thermal undulations on the rigidity of fluid membranes and interfaces”. In: *Journal de Physique* 46.7 (1985), pp. 1263–1268.
- [20] Udo Seifert. “Curvature-induced lateral phase segregation in two-component vesicles”. In: *Physical Review Letters* 70.9 (Mar. 1993), pp. 1335–1338.
- [21] Ilan Tsafrir et al. “Pearling Instabilities of Membrane Tubes with Anchored Polymers”. In: *Physical Review Letters* 86.6 (2001), pp. 1138–1141.
- [22] Ilan Tsafrir et al. “Coiling instability of multilamellar membrane tubes with anchored polymers”. In: *Physical Review E* 63.3 (2001).
- [23] Joshua Zimmerberg and Michael M Kozlov. “How proteins produce cellular membrane curvature.” In: *Nature Reviews Molecular Cell Biology* 7.1 (Jan. 2006), pp. 9–19.
- [24] Britta Qualmann, Dennis Koch, and Michael Manfred Kessels. “Let’s go bananas: revisiting the endocytic BAR code.” In: *The EMBO Journal* 30.17 (Aug. 2011), pp. 3501–15.
- [25] Marijn G J Ford et al. “Curvature of clathrin-coated pits driven by epsin.” In: *Nature* 419.6905 (Sept. 2002), pp. 361–6.
- [26] Felix Campelo, Harvey T. McMahon, and Michael M. Kozlov. “The Hydrophobic Insertion Mechanism of Membrane Curvature Generation by Proteins”. In: *Biophysical Journal* 95.5 (Sept. 2008), pp. 2325–2339.
- [27] Karel Drbal et al. “Single-molecule microscopy reveals heterogeneous dynamics of lipid raft components upon TCR engagement.” In: *International immunology* 19.5 (May 2007), pp. 675–84.

- [28] Tobias Zech et al. “Accumulation of raft lipids in T-cell plasma membrane domains engaged in TCR signalling.” In: *The EMBO Journal* 28.5 (Mar. 2009), pp. 466–76.
- [29] Kai Simons and Gerrit Van Meer. “Lipid sorting in epithelial cells”. In: *Biochemistry* 27.17 (Aug. 1988), pp. 6197–6202.
- [30] Kai Simons and Julio L Sampaio. “Membrane organization and lipid rafts.” en. In: *Cold Spring Harbor perspectives in biology* 3.10 (Oct. 2011), a004697.
- [31] Akihiro Kusumi, Ikuko Koyama-Honda, and Kenichi Suzuki. “Molecular dynamics and interactions for creation of stimulation-induced stabilized rafts from small unstable steady-state rafts.” In: *Traffic (Copenhagen, Denmark)* 5.4 (Apr. 2004), pp. 213–30.
- [32] Mario Brameshuber et al. “Imaging of mobile long-lived nanoplatforms in the live cell plasma membrane.” In: *The Journal of Biological Chemistry* 285.53 (Dec. 2010), pp. 41765–71.
- [33] Christian Klose et al. “Yeast lipids can phase-separate into micrometer-scale membrane domains.” In: *The Journal of Biological Chemistry* 285.39 (Sept. 2010), pp. 30224–32.
- [34] Ana J García-Sáez, Salvatore Chiantia, and Petra Schwille. “Effect of line tension on the lateral organization of lipid membranes.” In: *The Journal of Biological Chemistry* 282.46 (Nov. 2007), pp. 33537–44.
- [35] Aurelia R. Honerkamp-Smith et al. “Line Tensions, Correlation Lengths, and Critical Exponents in Lipid Membranes Near Critical Points”. In: *Biophysical Journal* 95.1 (July 2008), pp. 236–246.
- [36] Robert Brewster and Samuel A Safran. “Line active hybrid lipids determine domain size in phase separation of saturated and unsaturated lipids.” In: *Biophysical Journal* 98.6 (Mar. 2010), pp. L21–3.
- [37] Reinhard Lipowsky and Rumiana Dimova. “Domains in membranes and vesicles”. In: *Journal of Physics: Condensed Matter* 15.1 (Jan. 2003), S31–S45.
- [38] John F Hancock. “Lipid rafts: contentious only from simplistic standpoints.” In: *Nature Reviews Molecular Cell Biology* 7.6 (June 2006), pp. 456–62.
- [39] R Brewster, P A Pincus, and S A Safran. “Hybrid lipids as a biological surface-active component.” In: *Biophysical Journal* 97.4 (Aug. 2009), pp. 1087–94.
- [40] Katrin Weise et al. “Influence of the lipidation motif on the partitioning and association of N-Ras in model membrane subdomains.” In: *Journal of the American Chemical Society* 131.4 (Feb. 2009), pp. 1557–64.
- [41] Sarah L Veatch et al. “Critical fluctuations in domain-forming lipid mixtures.” In: *Proceedings of the National Academy of Sciences of the United States of America* 104.45 (Nov. 2007), pp. 17650–17655.

- [42] Clifford P. Brangwynne. “Soft active aggregates: mechanics, dynamics and self-assembly of liquid-like intracellular protein bodies”. In: *Soft Matter* 7.7 (2011), pp. 3052–3059.
- [43] Thierry Mora and William Bialek. “Are Biological Systems Poised at Criticality?” In: *Journal of Statistical Physics* 144.2 (June 2011), pp. 268–302.
- [44] A T Hammond et al. “Crosslinking a lipid raft component triggers liquid ordered-liquid disordered phase separation in model plasma membranes.” In: *Proceedings of the National Academy of Sciences of the United States of America* 102.18 (May 2005), pp. 6320–5.
- [45] Allen P Liu and Daniel A Fletcher. “Actin polymerization serves as a membrane domain switch in model lipid bilayers.” In: *Biophysical Journal* 91.11 (Dec. 2006), pp. 4064–70.
- [46] Daniel Lingwood et al. “Plasma membranes are poised for activation of raft phase coalescence at physiological temperature.” In: *Proceedings of the National Academy of Sciences of the United States of America* 105.29 (July 2008), pp. 10005–10.
- [47] Christine S Scheve et al. “Steric Pressure between Membrane-Bound Proteins Opposes Lipid Phase Separation.” In: *Journal of the American Chemical Society* (Jan. 2013).
- [48] David Boal. *Mechanics of the Cell*. Cambridge University Press, 2012, p. 622.
- [49] Allen P Liu et al. “Membrane-induced bundling of actin filaments.” In: *Nature Physics* 4 (Aug. 2008), pp. 789–793.
- [50] A Mogilner and B Rubinstein. “The physics of filopodial protrusion.” In: *Biophysical Journal* 89.2 (Aug. 2005), pp. 782–95.
- [51] Kwonmoo Lee et al. “Self-assembly of filopodia-like structures on supported lipid bilayers.” In: *Science (New York, N.Y.)* 329.5997 (Sept. 2010), pp. 1341–5.
- [52] Volker Schaller et al. “Polar patterns of driven filaments.” In: *Nature* 467.7311 (Sept. 2010), pp. 73–7.
- [53] Tariq Butt et al. “Myosin motors drive long range alignment of actin filaments.” In: *The Journal of Biological Chemistry* 285.7 (Feb. 2010), pp. 4964–74.
- [54] Yutaka Sumino et al. “Large-scale vortex lattice emerging from collectively moving microtubules.” In: *Nature* 483.7390 (Mar. 2012), pp. 448–52.
- [55] Harvey T McMahon and Emmanuel Boucrot. “Molecular mechanism and physiological functions of clathrin-mediated endocytosis.” In: *Nature Reviews Molecular Cell Biology* 12.8 (Aug. 2011), pp. 517–33.
- [56] Eva M Schmid and Harvey T McMahon. “Integrating molecular and network biology to decode endocytosis.” In: *Nature* 448.7156 (Aug. 2007), pp. 883–8.
- [57] Philip N Dannhauser and Ernst J Ungewickell. “Reconstitution of clathrin-coated bud and vesicle formation with minimal components.” In: *Nature Cell Biology* 14.6 (June 2012), pp. 634–9.

- [58] Wanda Kukulski et al. “Plasma membrane reshaping during endocytosis is revealed by time-resolved electron tomography.” In: *Cell* 150.3 (Aug. 2012), pp. 508–20.
- [59] David L Richmond et al. “Forming giant vesicles with controlled membrane composition, asymmetry, and contents.” In: *Proceedings of the National Academy of Sciences of the United States of America* 108.23 (June 2011), pp. 9431–6.
- [60] Anand Bala Subramaniam et al. “Glycans pattern the phase behaviour of lipid membranes.” In: *Nature Materials* 12.2 (Nov. 2012), pp. 128–33.
- [61] Daan Frenkel and Berend Smit. *Understanding Molecular Simulation: From Algorithms to Applications*. Second. Vol. 1. Academic Press, Nov. 2001.
- [62] M Venturoli et al. “Mesoscopic models of biological membranes”. In: *Physics Reports* 437.1-2 (Dec. 2006), pp. 1–54.
- [63] Siewert J. Marrink, Alex H. de Vries, and Alan E. Mark. “Coarse Grained Model for Semiquantitative Lipid Simulations”. In: *The Journal of Physical Chemistry B* 108.2 (Jan. 2004), pp. 750–760.
- [64] IR Cooke, Kurt Kremer, and Markus Deserno. “Tunable generic model for fluid bilayer membranes”. In: *Physical Review E* September 2004 (2005), pp. 2–5.
- [65] G. Gompper and D. M. Kroll. “Network models of fluid, hexatic and polymerized membranes”. eng. In: *Journal of physics. Condensed matter* 9.42 (1997), pp. 8795–8834.
- [66] Andrea Pasqua et al. “Large-scale simulations of fluctuating biological membranes”. In: *The Journal of Chemical Physics* 132.15 (2010).
- [67] Benedict J Reynwar et al. “Aggregation and vesiculation of membrane proteins by curvature-mediated interactions.” In: *Nature* 447.7143 (May 2007), pp. 461–4.
- [68] Siewert J Marrink and Alan E Mark. “The mechanism of vesicle fusion as revealed by molecular dynamics simulations.” en. In: *Journal of the American Chemical Society* 125.37 (Sept. 2003), pp. 11144–5.
- [69] Frédérick de Meyer and Berend Smit. “Effect of cholesterol on the structure of a phospholipid bilayer.” In: *Proceedings of the National Academy of Sciences of the United States of America* 106.10 (Mar. 2009), pp. 3654–8.
- [70] Frank L H Brown. “Continuum simulations of biomembrane dynamics and the importance of hydrodynamic effects.” In: *Quarterly reviews of biophysics* 44.4 (Nov. 2011), pp. 391–432.
- [71] Touko Apajalahti et al. “Concerted diffusion of lipids in raft-like membranes”. en. In: *Faraday Discussions* 144 (2010), p. 411.
- [72] Alba Diz-Muñoz, Daniel A Fletcher, and Orion D Weiner. “Use the force: membrane tension as an organizer of cell shape and motility.” In: *Trends in Cell Biology* 23.2 (Nov. 2012), pp. 47–53.

- [73] Margarita Staykova et al. “Mechanics of surface area regulation in cells examined with confined lipid membranes”. In: *Proceedings of the National Academy of Sciences* 108.22 (May 2011), pp. 9084–9088.
- [74] Bidisha Sinha et al. “Cells respond to mechanical stress by rapid disassembly of caveolae.” In: *Cell* 144.3 (Feb. 2011), pp. 402–13.
- [75] Jeanne C. Stachowiak, Carl C. Hayden, and Darryl Y. Sasaki. “Steric confinement of proteins on lipid membranes can drive curvature and tubulation”. In: *Proceedings of the National Academy of Sciences* 107.17 (Apr. 2010), pp. 7781–7786.
- [76] Jeanne C Stachowiak et al. “Membrane bending by protein-protein crowding.” In: *Nature Cell Biology* 14.9 (Sept. 2012), pp. 944–9.
- [77] David Chandler. *Introduction to Modern Statistical Mechanics*. 1st ed. Oxford University Press, USA, Sept. 1987.
- [78] Jean-Pierre Hansen and I.R. McDonald. *Theory of Simple Liquids*. Academic Press, 2006, p. 428.
- [79] Yuhua Song, E. A. Mason, and Richard M. Stratt. “Why does the Carnahan-Starling equation work so well?” In: *The Journal of Physical Chemistry* 93.19 (Sept. 1989), pp. 6916–6919.
- [80] Tom Kirchhausen. “Bending membranes.” In: *Nature cell biology* 14.9 (Sept. 2012), pp. 906–8.
- [81] Maddalena Venturoli et al. “Mesoscopic models of biological membranes”. In: *Physics Reports* 437.1 (2006), pp. 1–54.
- [82] JM Drouffe, AC Maggs, and S Leibler. “Computer simulations of self-assembled membranes”. In: *Science* 254.5036 (Nov. 1991), pp. 1353–1356.
- [83] John D. Weeks, David Chandler, and Hans C. Andersen. “Role of Repulsive Forces in Determining the Equilibrium Structure of Simple Liquids”. In: *The Journal of Chemical Physics* 54.12 (1971), pp. 5237–5247.
- [84] Michael P. Allen and Dominic J. Tildesley. *Computer Simulation of Liquids*. Oxford University Press, 1989, p. 385.
- [85] Philip D Blood, Richard D Swenson, and Gregory A Voth. “Factors Influencing Local Membrane Curvature Induction by N-BAR Domains as Revealed by Molecular Dynamics Simulations”. In: *Biophysical Journal* 95.August (2008), pp. 1866–1876.
- [86] B. J. Alder and T. E. Wainwright. “Phase Transition for a Hard Sphere System”. In: *The Journal of Chemical Physics* 27.5 (Aug. 1957), p. 1208.
- [87] Frank L H Brown. “Elastic modeling of biomembranes and lipid bilayers.” In: *Annual review of physical chemistry* 59 (Jan. 2008), pp. 685–712.
- [88] Vagelis A Harmandaris and Markus Deserno. “A novel method for measuring the bending rigidity of model lipid membranes by simulating tethers.” In: *The Journal of chemical physics* 125.20 (Nov. 2006), p. 204905.

- [89] J.-S Ho and A Baumgärtner. “Simulations of Fluid Self-Avoiding Membranes”. en. In: *Europhysics Letters (EPL)* 12.4 (June 1990), pp. 295–300.
- [90] G Gompper and D M Kroll. “Network models of fluid, hexatic and polymerized membranes”. en. In: *Journal of Physics: Condensed Matter* 9.42 (Oct. 1997), pp. 8795–8834.
- [91] L. Bo and R.E. Waugh. “Determination of bilayer membrane bending stiffness by tether formation from giant, thin-walled vesicles”. In: *Biophysical Journal* 55.3 (1989), pp. 509–517.
- [92] Rudolph J.E. Clausius. “On a mechanical theorem applicable to heat”. In: *Philosophical Magazine Series 4* 40.265 (1870), pp. 122–127.
- [93] Maddalena Venturoli and Berend Smit. “Simulating the self-assembly of model membranes”. en. In: *PhysChemComm* 2.10 (Jan. 1999), p. 45.
- [94] Brian J Peter et al. “BAR domains as sensors of membrane curvature: the amphiphysin BAR structure.” In: *Science (New York, N. Y.)* 303.5657 (Jan. 2004), pp. 495–9.
- [95] Gary S Ayton, Philip D Blood, and Gregory A Voth. “Membrane Remodeling from N-BAR Domain Interactions : Insights from Multi-Scale Simulation”. In: *Biophysical Journal* 92.10 (2007), pp. 3595–3602.
- [96] Carsten Mim et al. “Structural basis of membrane bending by the N-BAR protein endophilin.” In: *Cell* 149.1 (Mar. 2012), pp. 137–45.
- [97] Edward Lyman, Haosheng Cui, and Gregory a Voth. “Water under the BAR.” In: *Biophysical journal* 99.6 (Sept. 2010), pp. 1783–90.
- [98] J Ryckaert, G Ciccotti, and H Berendsen. “Numerical integration of the cartesian equations of motion of a system with constraints: molecular dynamics of n-alkanes”. In: *Journal of Computational Physics* 23.3 (Mar. 1977), pp. 327–341.
- [99] Joshua Zimmerberg and Stuart McLaughlin. “Membrane Curvature: How BAR Domains Bend Bilayers”. In: *Current Biology* 14.6 (Mar. 2004), R250–R252.
- [100] William Mike Henne et al. “FCHo Proteins Are Nucleators of Clathrin-Mediated Endocytosis.” In: *Science (New York, N. Y.)* 1281 (May 2010).
- [101] Enas Abu Shah and Kinneret Keren. “Mechanical forces and feedbacks in cell motility.” In: *Current opinion in cell biology* 25.5 (Oct. 2013), pp. 550–7.
- [102] Gary J Doherty and Harvey T McMahon. “Mechanisms of endocytosis.” In: *Annual Review of Biochemistry* 78 (Jan. 2009), pp. 857–902.
- [103] R. Lipowsky. “Bending of Membranes by Anchored Polymers”. In: *EPL (Europhysics Letters)* 30.4 (May 1995).
- [104] Christin Hiergeist and Reinhard Lipowsky. “Elastic Properties of Polymer-Decorated Membranes”. en. In: *Journal de Physique II* 6.10 (Oct. 1996), pp. 1465–1481.

- [105] Wokyung Sung and SeungKyun Lee. “The soft-mode instability of a membrane induced by strong polymer adsorption”. en. In: *Europhysics Letters (EPL)* 68.4 (Nov. 2004), pp. 596–602.
- [106] Grace Brannigan and FLH Brown. “A consistent model for thermal fluctuations and protein-induced deformations in lipid bilayers”. In: *Biophysical journal* 90.5 (2006), pp. 1501–1520.
- [107] E. Evans and W. Rawicz. “Elasticity of “Fuzzy” Biomembranes”. In: *Physical Review Letters* 79.12 (Sept. 1997), pp. 2379–2382.
- [108] P. Girard, J. Prost, and P. Bassereau. “Passive or Active Fluctuations in Membranes Containing Proteins”. In: *Physical Review Letters* 94.8 (2005).
- [109] M. Faris et al. “Membrane Tension Lowering Induced by Protein Activity”. In: *Physical Review Letters* 102.3 (Jan. 2009), pp. 1–4.
- [110] Hao Wu, Hayato Shiba, and Hiroshi Noguchi. “Mechanical properties and microdomain separation of fluid membranes with anchored polymers”. en. In: *Soft Matter* 9.41 (Oct. 2013), p. 9907.
- [111] Dmitri I Svergun and Michel H J Koch. “Small-angle scattering studies of biological macromolecules in solution”. In: *Reports on Progress in Physics* 66.10 (Oct. 2003), pp. 1735–1782.
- [112] GP Vigers, RA Crowther, and BM Pearse. “Three-dimensional structure of clathrin cages in ice.” In: *The EMBO journal* 5.3 (Mar. 1986), pp. 529–534.
- [113] R. Nossal. “Energetics of Clathrin Basket Assembly”. In: *Traffic* 2.2 (2001), pp. 138–147.
- [114] Wouter K. den Otter, Marten R. Renes, and W.J. Briels. “Asymmetry as the Key to Clathrin Cage Assembly”. In: *Biophysical Journal* 99.4 (Aug. 2010), pp. 1231–1238.
- [115] Shafiq Mehraeen et al. “Impact of defect creation and motion on the thermodynamics and large-scale reorganization of self-assembled clathrin lattices”. en. In: *Soft Matter* 7.19 (May 2011), p. 8789.
- [116] Sander Pronk, Phillip L. Geissler, and Daniel A. Fletcher. “Limits of Filopodium Stability”. In: *Physical Review Letters* 100.25 (2008).